

UNIVERSITY OF CALIFORNIA

Los Angeles

A Transient Model for Predicting Concentration Polarization
in Commercial Spiral Wound Membranes

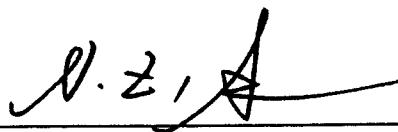
A dissertation submitted in partial satisfaction of the
requirements for the degree of Doctor of Philosophy
in Civil Engineering

by

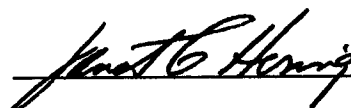
Kapal Madireddi

1996

The dissertation of Kapal Madireddi is approved.



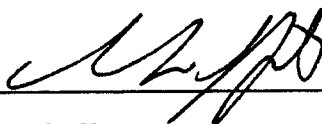
Ne Zhing Sun



Janet Hering



Menachem Elimelech



I. H. (Mel) Suffet



Michael K. Stenstrom, Committee Chair

University of California, Los Angeles

1996

Dedicated to my parents
Sowjanya and M. C. Rao,
and grandparents
Rajamani and Late M. Durga Rao

TABLE OF CONTENTS

Table of Contents	iv
List of Figures	vii
List of Tables	xii
List of Symbols	xiii
Acknowledgments	xviii
Vita	xx
Publications and Presentations	xx
Abstract of the Dissertation	xxii
1. Introduction	1
1.1 Problem Statement and Significance	1
1.2 Statement of Objectives	6
1.3 Dissertation Organization	8
2. Background Literature Review	11
2.1 Introduction to Membrane Separation Processes	11
2.1.1 Osmosis	11
2.1.2 Reverse Osmosis	16
2.1.3 Classification of Membrane Processes	17

2.1.4 Commercial Membrane Modules	24
2.1.5 Membrane Applications	28
2.2 Membrane Transport	28
2.2.1 Fundamental Equations	28
2.2.2 Models for Membrane Transport	32
2.3 Concentration Polarization (CP) and Fouling	35
2.3.1 Basic Definitions	35
2.3.2 Fundamental Models for CP	38
2.3.3 Models for Membrane Fouling	51
2.4 Minimizing CP and Fouling	55
2.5 Modeling CP in Commercial Membrane Systems	57
2.5.1 Momentum Transport and Velocity Profiles	58
2.5.2 Pressure Profiles	66
2.5.3 Mass Transport	67
2.5.4 Solution Techniques	68
2.5.5 Limitation of Existing Work	71
3. Model Development and Experimental Methods	75
3.1 Model Development	75
3.1.1 Mathematical Formulation	75
3.1.2 Determination of Experimental Parameters	81

3.1.3 Numerical Solution of Model Equations	88
3.2 Experimental Methods	95
4. Results and Discussion	100
4.1 Numerical Stability	100
4.2 Accuracy	103
4.3 Parametric Consistency	110
4.4 Model Predictions	121
4.4.1 Laminar Flow	121
4.4.2 Spiral Wound Membranes	134
4.5 Experimental Verification	140
5. Summary and Conclusions	148
Appendix I	151
Appendix II	199
References	216

LIST OF FIGURES

Fig 2.1 Schematic description of osmosis, osmotic equilibrium and reverse osmosis.

Fig 2.2 Illustration of different pressure driven processes and conventional filtration (CF) based on pore size distribution.

Fig 2.3 Schematic of a generalized membrane process.

Fig 2.4 Development of concentration polarization (CP) in membrane processes: (a) initial state; (b) transient state; and (c) steady state.

Fig 2.5 Schematic description of the gel polarization model.

Figure 2.6 Flow in membrane modules: (a) Laminar flow in channels with two porous walls, and (b) flow in porous pipes.

Figure 2.7 Effect of the eddy constant m on axial velocity in a spiral wound membrane.

Figure 2.8 Permeate flux decline during NF separation of wastewater effluent for a 12 week test period in Lake Arrowhead, CA with weekly chemical cleaning: normalized flux (GFD/psi) at ambient temperature and at 77 °F depicted over time.

Figure 3.1 Pure water permeability tests conducted on a spiral wound RO unit at various temperatures and constant feed flow of 3.0 gallons per minute (GPM). Permeation velocity in gallons per day per square foot of membrane area (GFD) versus operating pressure in psi; permeability coefficient A is defined by the slope of each line.

Figure 3.2 Pure water permeability tests for constant feed flow of 2.0 GPM. Permeation velocity in GFD versus operating pressure in psi; the permeability coefficient A is defined by the slope of the best-fit lines.

Figure 3.3 Permeability coefficient A (GFD/psi) versus ambient temperature in °C for constant feed flows of 2 and 3 GPM.

Figure 3.4 Osmotic pressure versus solute (NaCl) concentration at various temperatures (Data from Sourirajan [1970]).

Figure 3.5 Osmotic pressure constant K_{osm} (psi.L/mg) versus temperature based on data from Sourirajan [1970].

Figure 3.6 Graphical representation of the FD solution.

Figure 3.7 Schematic description of the pilot-scale RO unit.

Figure 4.1 Stability as a function of time increment ΔT -CP modulus calculated at the axial mid-point on the membrane surface after t_r .

Figure 4.2 Stability as a function of transverse increment ΔY -CP modulus calculated at the axial mid-point on the membrane surface after t_r .

Figure 4.3 CP modulus versus ratio of time and axial increments-CP modulus calculated at the axial mid-point on the membrane surface after t_r .

Figure 4.4 Steady state CP modulus versus number of axial divisions of the membrane unit (Operating conditions based on Table 3.1).

Figure 4.5 Comparison of the model with earlier steady state FEM solution by Bhattacharya [1990].

Figure 4.6 Effect of membrane permeability A on CP: plot shows the ratio of solute concentration on the membrane surface at the axial mid-point to feed solute concentration versus starting permeate recovery.

Figure 4.7 Effect of membrane permeability A on flux decline: plot shows steady state permeate flow versus initial permeate flow.

Figure 4.8 Effect of solute rejection coefficient R on CP: plot shows the ratio of solute concentration on the membrane surface at the axial mid-point to feed solute concentration versus initial permeate recovery.

Figure 4.9 Effect of solute rejection coefficient R on flux decline: plot shows steady state permeate flow versus initial permeate flow.

Figure 4.10 Effect of the osmotic pressure constant K_{osm} on CP: plot shows the ratio of solute concentration on the membrane surface at the axial mid-point to feed solute concentration versus starting permeate recovery.

Figure 4.11 Effect of the osmotic pressure constant K_{osm} on flux decline: plot shows steady state permeate flow versus initial permeate flow.

Figure 4.12 Effect of solute diffusivity D_s on CP; plot shows steady state CP modulus at the axial mid-point on the membrane surface versus D_s .

Figure 4.13 Effect of the solute diffusivity D_s on permeate flux decline: plot shows steady state permeate flow versus initial permeate flow.

Figure 4.14 Transient state model predictions: flux decline (in GPD) is plotted versus time in multiples of nominal residence time t_r .

Figure 4.15 Steady state CP modulus at the axial mid-point on the membrane surface versus initial permeate recovery for various feed solute concentrations.

Figure 4.16 Steady state versus initial permeate flow for various feed solute concentrations for laminar flow conditions.

Figure 4.17 Effect of laminar vs completely mixed flow regimes on CP build-up: CP modulus is plotted versus initial permeate recovery for different feed solute concentrations.

Figure 4.18 Steady-state versus initial permeate flow for laminar and completely mixed flow regimes: flux decline for two feed solute concentrations are depicted.

Figure 4.19 Effect of cross-flow Reynolds' number on CP through an increase in feed flow: steady state CP modulus ($X=0.5$, $Y=1$) plotted versus initial permeate flow.

Figure 4.20 Effect of cross-flow Reynolds' number based on feed flow rate on permeate flux decline.

Figure 4.21 Effect of recycle ratio on permeate flux decline.

Figure 4.22 Effect of ambient temperature on CP for laminar channel flow.

Figure 4.23 Effect of ambient temperature on permeate flux decline.

Figure 4.24 Effect of feed solute concentration on CP for spiral wound flow.

Figure 4.25 Effect of feed solute concentration on permeate flux decline for spiral wound flow.

Figure 4.26 Effect of various cross-flow regimes on permeate flux decline.

Figure 4.27 Effect of channel width and spacer eddy constant m on permeate flux decline.

Figure 4.28 Development of CP and flux decline over time: Model results for three flow regimes (laminar, turbulent and spacer induced mixing) are compared with experimental data from a pilot-scale RO unit.

Figure 4.29 Permeate flux decline for a feed concentration of 200 mg/L for various initial recoveries at zero recycle: Model results versus experimental data are depicted.

Figure 4.30 Permeate flux decline for a feed concentration of 1000 mg/L for various initial recoveries at zero recycle: Model results versus experimental data are depicted.

Figure 4.31 Model results versus experimental data for various initial recoveries at a recycle ratio of 1.

Figure 4.32 Model results versus experimental data for feed flow of 2880 GPD and zero recycle.

LIST OF TABLES

Table 2.1: Size-based classification of membrane processes.

Table 2.2: Selected Applications of membrane processes.

Table 3.1: Feed and operating conditions, and membrane characteristics of the spiral wound RO unit employed in this study for experimental verification and parametric analysis.

Table 4.1: Description of feed and operating conditions for comparison with the Bhattacharya Model (Accuracy analysis).

LIST OF SYMBOLS

a_s	Activity of solute
a_w	Activity of solvent (water)
A	Membrane Permeability
A_m	Membrane Area
B	Solute Permeability
c_0	Inlet (Feed) Solute Concentration
c_b	Bulk Solute Concentration
C_b	Dimensionless Bulk Solute Concentration
c_g	Gel Concentration
C_g	Dimensionless Gel Concentration
c_m	Membrane Surface Solute Concentration (c_w)
c_p	Permeate Side Solute Concentration
C_p	Dimensionless Permeate Solute Concentration
c_s	Solute Concentration
$(c_s)_{ln}$	Logarithmic Mean Average of Solute Concentration
C	Dimensionless Concentration
d_h	Hydraulic Diameter
d_s	Spacer Fiber Thickness
D	Dimensionless Solute Diffusivity

D_s	Solute Diffusivity
$\bar{\bar{D}}_s$	Diffusion Tensor
E	Internal Energy
\bar{F}	Force Vector
G	Gibbs Free Energy
H	Channel Half Thickness
i	Numerical Coordinate (Axial Direction)
j	Numerical Coordinate (Transverse Direction)
j_0	Pure Water Flux
\bar{j}_c	Mass Flux Vector
J_f	Fouled Flux
J_i	Unfouled Starting Flux
J_R	Reynolds Flux
J_s	Solute Flux
j_{ss}	Steady State Water Flux
J_v	Solvent (Water) Volume Flux (J_w, j_w)
k	Mass Transfer Coefficient
K_3	Membrane Transport Coefficient (Solution-Diffusion-Imperfection Model)
L	Length of the Module
L_p	Filtration Coefficient
m	Eddy Constant

M	Concentration Polarization Modulus
M_d	Mass of the Foulant per Unit Area of the Membrane
M_s	Mass of the Solute
n_s	Number of Spacers
n_i	Moles of i^{th} Component
N_F	Filtration Number
P	Operating Pressure
\bar{q}_H	Heat Flux Vector
Q_f	Feed Flow
Q_p	Permeate Flow
r	Radial Coordinate
rec	Permeate Recovery
r_m	Tube Radius
r_d	Rate of Deposition (Kimura-Nakao Model)
r_e	Rate of Removal (Kimura-Nakao Model)
R	Membrane Solute Rejection
R_{bl}	Boundary Layer Resistance
R_m	Membrane Resistance
R_s	Cake Resistance
Re	Reynolds Number
Re_y	Permeation Reynolds Number

R_g	Universal Gas Constant
S	Entropy
Sc	Schmidt Number
Sh	Sherwood Number
t	Time Coordinate
t_s	Spacer Thickness
T	Dimensionless Time
T_s	System Temperature
u	Axial Velocity
u_{avg}	Average Axial Velocity
U	Dimensionless Axial Velocity
v	Transverse Velocity
V	Dimensionless Transverse Velocity
V_p	Dimensionless Wall Permeation Velocity
V_s	System Volume
\bar{V}	Molar Volume
W	Width of the Membrane
x	Axial coordinate
x_s	Solute Molar Fraction
x_w	Solvent Molar Fraction
y	Transverse Coordinate

Y	Dimensionless Transverse Coordinate
z	Axial Coordinate

GREEK SYMBOLS

α	Specific Cake Resistance
β_T	Empirical Turbulence Burst Factor
Δ	Difference
ε	Spacer Porosity
ϕ	Molar Osmotic Coefficient
δ	Boundary Layer Thickness
δ_r	Thickness of the Reaction Layer (Kinetic Growth Model)
κ	Constant in Green-Belfort Model
λ	Dimensionless Coordinate
μ	Viscosity of the Solvent
ν	Kinematic Viscosity
Π	Osmotic Pressure
ρ	Density
σ	Reflection Coefficient
θ	Accumulated Time
τ_w	Wall Shear
ω	Solute Permeability

ACKNOWLEDGEMENTS

I wish to express my sincere gratitude to Professor Michael K. Stenstrom, for his support and encouragement during my graduate studies program at UCLA . Mike has been a mentor and friend, and in his capacity as my graduate advisor and thesis committee chair, helped me considerably on matters relating to my graduate studies. I also wish to express my gratitude to Dr. I. H. (Mel) Suffet, Professor of Environmental Health Sciences, who was my co-advisor at UCLA; I found his advice on matters relating to the Lake Arrowhead project and my thesis work quite insightful.

I wish to express my thanks to the other members of the doctoral committee Dr. Menachem (Meny) Elimelech, Dr. Janet Hering, and Dr. N. Z. Sun for their advice and assistance on problems I encountered during my stay at UCLA. Julius (Bud) Glater , Senior Research Engineer at UCLA, who is an expert on membrane technology with nearly forty years of experience, and who had worked with some of the pioneering members in this field, also helped me a great deal during my graduate work; I wish to express my thanks to him.

I am also indebted to Dr. Roger Babcock with whom I worked for over a year during the Lake Arrowhead project. Roger has been a mentor and friend to me; I found his advice on matters relating to my studies and professional career very useful. I also had the pleasure of sharing a house with him and Jill (Babcock) who is an excellent gourmet cook.

I wish to express my gratitude to all my friends and students I worked with during my stay at Lake Arrowhead and UCLA; they include among many Dr. Simlin Lau, Bruno Levine, Scott Burke, Eakalak Khan and Fang Q. Ye. Many thanks are due to Elizabeth Chacko, Linda Schweitzer, Nagaraj Vishwanath, Muddu Sudhakar, and Suresh Lingineni. John Langholff of UCLA Department of Civil assisted and taught me many technical and hands-on issues during the Lake Arrowhead project. I am also indebted to the personnel from the Lake Arrowhead Community Services District, and J. B. Neethling from HDR Engineering Inc. for his help during the project. Many thanks are also due to Debby Haines, Deonna Columbia, Janice Bedig, Joanne Amos and rest of the staff in the Department of Civil and Environmental Engineering at UCLA

Finally, I wish to express my gratitude and affection to my parents, brothers, sister, and family who gave unwavering support and love during my studies at UCLA.

The research described in this dissertation and the work related to the Lake Arrowhead Advanced Wastewater Reclamation Project was supported by a grant from the Ahmanson Foundation; additional support was provided by the Lake Arrowhead Community Services District and the Department of Civil and Environmental Engineering at UCLA.

VITA

April 4, 1969--Born, Madras, India

1990 B. Tech in Chemical Engineering

Indian Institute of Technology, Madras, India

1992 M. S. in Chemical Engineering

University of Southern California, Los Angeles

1996 M. S. in Civil Engineering

University of California, Los Angeles

1996 Ph.D in Civil Engineering

University of California, Los Angeles

PUBLICATIONS AND PRESENTATIONS

Wastewater Reclamation at Lake Arrowhead. J. B. Neethling, M. K. Stenstrom, K. Madireddi, and I. H. (Mel) Suffet. Presented at the 1993 American Water Works Association Conference Proceedings on Water Reuse, Houston, Texas.

Denitrification in a Fluidized Bed: A Lake Arrowhead Pilot Study. K. Madireddi, B. Levine, J. B. Neethling and M. K. Stenstrom. Presented at the 1994 Water Environment Federation Conference Proceedings, October 15-19, 1994, Chicago, Illinois.

Indirect Potable Reuse at Lake Arrowhead, California. K. Madireddi and J. Glater.

Presented at the 1995 Proceedings of the International Desalination Association World Congress on Desalination and Water Sciences, November 18-24, Abu Dhabi, UAE.

Pilot-Scale Wastewater Repurification for Indirect Potable Reuse. R. W. Babcock, K.

Madireddi, I. H. Suffet and M. K. Stenstrom. Presented at the 1995 Proceedings of the International Chemical Congress of Pacific Basin Societies, December 17-22, Honolulu, Hawaii.

Fluidized Bed Denitrification of Secondary Effluent during Wastewater Reclamation in Southern California. K. Madireddi, R. W. Babcock, and M. K. Stenstrom. Presented in the 1996 American Society of Civil Engineers (ASCE) Water and Environment Congress, June 22-28, Anaheim, CA,

ABSTRACT OF THE DISSERTATION

A Transient Model for Predicting Concentration Polarization in
Commercial Spiral Wound Membranes

by

Kapal Madireddi

Doctor of Philosophy in Civil Engineering

University of California, Los Angeles, 1996

Professor Michael K. Stenstrom, Chair

This dissertation investigates concentration polarization and resulting permeate flux decline in commercial spiral wound membranes. Concentration polarization refers to the accumulation of contaminants (solutes) near the membrane surface that offer additional resistance to separation. It is a serious problem that decreases permeate throughput and quality, increases operating costs and results in frequent membrane cleaning and replacement.

Previous studies on concentration polarization provided an understanding of the process at a fundamental level but were limited to simplified membrane systems such as

the one-dimensional batch cell or flow in porous pipes. This study focuses on predicting concentration polarization in commercial spiral wound membranes operating at high solvent recoveries.

A transient finite difference model is developed and presented to explain concentration polarization in spiral wound membranes that operate at moderate to high solvent recoveries. The solute mass transport equation is solved in axial and transverse directions along with appropriate fluid flow equations that describe flow in spiral wound membranes. In addition, a model for membrane transport based on osmotic theory is used to describe solvent (water) flow across the membrane surface.

The model was tested for numerical stability and accuracy, and compared with existing steady state models that predict concentration polarization for low solvent recoveries. The model was also verified with experimental data collected from a pilot-scale spiral wound reverse osmosis system. This included specific tests conducted to collect initial flux decline data during separation of NaCl solutions under various operating conditions. Finally, transient and steady state concentration polarization and permeate flux decline data are presented for a wide range of feed and operating conditions including different feed flow rates, recycle rates, temperatures and membrane permeabilities. This information is expected to be especially useful during design and operation of membrane facilities for both water and wastewater treatment, and desalination applications.

CHAPTER 1

INTRODUCTION

1.1 Problem Statement and Significance

Fresh water is a precious commodity that is rapidly diminishing due to population expansion and increased industrial activity. In a recent study, it was concluded that a substantial portion of surface water and groundwater supplies were contaminated by hazardous wastes alone [Fetter, 1993]. In addition, changes in global weather patterns may cause extended sporadic droughts in arid and semi-arid regions of the world, creating additional water shortage problems. As a result, public awareness about conserving existing resources has increased considerably [Crozes, 1993]; this concern has also translated into more comprehensive legislation and stricter regulations for protecting existing sources.

There is an ongoing search to augment existing fresh water sources from drought-tolerant resources; water reclamation is the most important example of this search, and is more feasible today than ever before. This is because of the technological and scientific advances that have taken place in the area of water and wastewater treatment. Several new technologies are available today for treating and reusing contaminated effluent discharges from municipal and industrial sources [Water Reuse, 1989]; examples include

granular activated carbon (GAC) adsorption and filtration, ion exchange, and membrane separation. The technologies have dramatically increased the quality of treatment, making the concept of water reuse more appealing to the public.

Of the above technologies, membrane separation processes such as reverse osmosis (RO) and ultrafiltration (UF) have gained considerable importance because they offer superior treatment at relatively modest capital and operating costs [Liu, 1987; Weisner, 1994]. The processes remove a wide range of contaminants present in untreated water, municipal and industrial wastewater discharges such as suspended and dissolved solids, organic matter, heavy metals, bacteria and viruses [Belfort, 1984]. Historically, RO was first developed as an alternative to thermal desalination processes such as multi-stage flash evaporation to reduce energy costs; however, the industry grew quickly and several new membranes based on synthetic polymers were developed for increasing the scope of applications. This has resulted in membranes being accepted as a popular form of treatment in various industries ranging from domestic applications such as water treatment, wastewater treatment and reclamation, and also specialized industrial applications such as paper and pulp treatment, and protein purification in biochemical engineering .

Specifically, the main advantages of membrane separation are: (1) the process is inherently simple and easy to implement; (2) the same governing principles hold even when applications differ (for example, water treatment, gas separation, and desalination);

(3) there is no phase change (e.g. evaporation) involved which decreases the overall energy requirements; and (4) the operation is in the ambient temperature range (20-40°C). Ambient temperature thus allows for temperature-sensitive applications which are especially important in the pharmaceutical and biotechnology industries (Soltanieh, 1981). In addition, the process generally does not require use of corrosive chemicals which are difficult to handle (as is the case in conventional treatment processes such as lime, and ferric chloride precipitation). As membrane processes continue to develop and receive greater acceptance, it is expected that their implementation will reduce the size and complexity of existing treatment facilities [Jacangelo, 1989].

In spite of the above advantages, the progress of membrane implementation at the full-scale level has been restricted because of two principal problems commonly encountered during operation: concentration polarization (CP) and fouling. CP refers to an increase in concentration of contaminants (solutes) near the membrane surface that offer additional resistance to separation. It is a reversible phenomena that occurs within a few hours of operation depending on the size of the membrane system. It is a result of the fundamental nature of membrane separation; the solute is transported to the surface of the membrane by advection and is rejected by the membrane barrier, and forced to accumulate near the surface.

Membrane fouling refers to the long term decline in the permeate flux from prolonged operation. Fouling is a complex phenomena with a number of influencing

factors such as membrane pore plugging, chemical degradation and bacterial growth [Potts, 1981]. Depending on the size of the system, fouling manifests over a long time period ranging from a few hundred hours to several thousand hours of operation. It is acknowledged that CP generally increases fouling, because it increases the concentration of contaminants such as bacteria, organic and inorganic material near the membrane surface which in turn aggravates the factors that cause fouling.

Both CP and fouling also negatively affect the useful life-span of membranes; though the manufacturers suggest a typical life-span of three to five years for most membranes, CP and fouling can cause a 50-75 % reduction in the life-span. On-site measures that are normally taken in order to decrease CP and fouling include: increasing solute mass transfer by dilution, stirring or promoting turbulence, use of tangential or cross flow type feed, operating at lower water (solvent) permeation rates, and use of anti-scalants and anti-foulants.

It is also necessary to develop theoretical models that describe these phenomena in order to improve design and implementation of membrane systems. A few models are available that address both CP and fouling at empirical and theoretical levels [Matthiason, 1980; Fane, 1986; Bowen, 1995]. Theoretical concepts are used to explain CP as it essentially involves solving the flow and solute mass transport equations with appropriate boundary conditions while empirical studies are more often used to describe fouling which depends on more complex physical and chemical factors.

Theoretical CP studies are centered around obtaining solutions for mass transport and flow balance (Navier-Stokes) equations; since the equations that describe membrane separation are quite complex, exact solutions exist only for simple systems such as the one-dimensional batch cell. Furthermore, approximate solutions are only available for systems where several simplifying assumptions are made; these include constant fluid and solute properties, simplified fluid flow profiles and steady-state analysis. The last assumption is a major limitation to the predictive capability of a model. In most membrane systems, CP reaches steady state within a few hours of operation but permeate flux continues to decline over time because of fouling and membrane degradation.

In order to address this problem correctly, a predictive transient model for CP is necessary that will allow for dynamic phenomena to be included at a latter stage. The initial transient data generated from such a model could be used to understand the conditions that develop and exist near the membrane surface. Such information could be used in improving the physical aspects of the model, and correct mechanistic assumptions that are made in developing the model.

Another limitation of existing work is that commercial systems are rarely taken into account; several CP studies are limited to either dead-end filtration systems (one-dimensional batch cells) or flat-cell units with very low permeate recoveries (permeate flow per unit feed flow). In real systems, there are several complicating factors such as

feed stream characteristics, membrane type (UF, RO etc.), module type (hollow-fiber, spiral wound etc.), and ambient conditions. The flow profiles in commercial modules are usually distorted and complex because of mixing and turbulence from feed spacers. These effects are very important especially in full-scale systems that operate at moderate to high recoveries (permeate flow per unit feed flow), and should be included to improve overall design.

It should be noted that a complete understanding of membrane separation of a multi-component system such as municipal or industrial wastewater effluents will be difficult because of complex interactions in the feed; however, a comprehensive model could be developed for a simplified organic or inorganic system with one or two solutes that could be used during full-scale design and implementation.

1.2 Statement of Objectives

The main objective of this work is to perform a systematic and comprehensive theoretical and experimental study of CP, and predict permeate flux behavior from initial transient conditions to the final steady state in a commercial spiral wound RO unit. A transient CP model is developed and tested mathematically and verified experimentally towards fulfilling this objective. Specifically, it involves the following tasks:

1. The model is developed by solving the solute mass transport equation employing a finite difference (FD) method. Three different fluid flow profiles are used that represent laminar, turbulent and spacer induced mixing. Thin-film theory is used to describe the membrane surface boundary conditions, and the osmotic pressure model will be used to describe the membrane permeation behavior.
2. The model is then tested for numerical stability and accuracy by varying key numerical parameters such as the numerical time step (Δt), numerical grid properties (Δx and Δy), and comparing steady state predictions with other available models. The model is also tested for its physical validity by performing a parametric analysis; this involves varying the physical parameters such as membrane permeability, solute diffusivity and osmotic pressure coefficient.
3. Once the model is validated in terms of stability and accuracy, it is verified with experiments; a pilot-scale spiral wound RO system is used to generate experimental information including transient and steady state permeate flux data over a range of operating conditions such as feed flow rates, feed solute concentrations, and recycle flow rates. Sodium chloride-water system is used so that the osmotic model assumption can be easily verified.
4. The model is then be used in generating CP and permeate flux decline behavior for several feed and membrane characteristics, ambient temperatures and

recommendations are made for extending the model for other solute-solvent systems such as organic and colloidal solutions.

The CP model as presented in this work does not deal with the problem of membrane fouling; however, the concepts on fouling are reviewed to enable future research on extending the model to incorporate long term flux decline. The model is a transient model that involves performing calculations as a function of time; however as CP steady state is reached, progressively larger time steps could be taken to include fouling phenomena that manifest over long time periods without losing significant computation time.

1.3 Dissertation Organization

In order to develop and address the problem of CP systematically, this dissertation has been organized in the following sequence. A detailed literature review on membrane processes including basic definitions and concepts is reported in chapter II. This is followed by a classification of membrane processes based on physical and chemical parameters such as pore size, membrane type and module type, and a brief outline of membrane applications. Existing information on membrane transport including various transport models such as the solution-diffusion model and irreversible thermodynamics model is presented followed by a detailed review of CP and fouling. All important

models of CP and fouling are discussed in terms of their scope and applicability, advantages and limitations.

This is followed by a review of existing research on CP for commercial membrane systems. All the necessary equations of mass, momentum and continuity are given in vector form and later expanded in different coordinate systems for different membrane modules such as hollow-fiber and spiral-wound units. The limitations of these models are also addressed to enable the comprehensive development of the CP model in this study.

In the third chapter, the development of the CP model is detailed including model formulation, solution sequence and a brief description of the computer code; the actual computer code is included in appendix II. The experimental apparatus that was used to verify model predictions is also described in the third chapter. Chapter IV deals with predictions of the model for various feed and operating conditions, an error analysis to verify the stability and accuracy of the model and a discussion on predicted versus experimental results.

A pilot-scale wastewater reclamation study in Lake Arrowhead that employed membrane treatment is discussed in appendix I; flux decline due to CP and fouling was a major concern during this project and a research need for more comprehensive understanding of membrane processes was identified during the course of the project.

The CP model in this dissertation was developed as a first step towards addressing the problems of flux decline that are common during membrane separation of wastewater effluents. The present model was verified experimentally on the pilot-scale membrane unit constructed for the Lake Arrowhead project.

CHAPTER 2

BACKGROUND LITERATURE REVIEW

2.1 Introduction to Membrane separation processes

2.1.1 Osmosis

Osmosis is the natural phenomenon that describes the passage of solvent between solutions of different concentrations separated by a semi-permeable membrane; solvent movement is normally from the less concentrated side to the more concentrated side in the absence of external forces as shown in Figure 2.1(a) [Findlay, 1913]. If the system is not subject to external influence such as removal of solvent, a hydrostatic pressure difference is established at equilibrium in the opposite direction at which point the net mass transport is zero as shown in Figure 2.1(b). This condition is known as osmotic equilibrium, and the corresponding pressure is referred to as osmotic pressure [Rautenbach, 1989].

The relationship between osmotic pressure and solute concentration can be explained using the chemical potential of the system; the chemical potential μ_i of component i is defined as

$$\mu_i = \left(\frac{\partial G}{\partial n_i} \right)_{P, T_s, n} \quad (1)$$

where G is the Gibbs free energy of the system, n_i is the number of moles of i , P is the system pressure and T_s is the system temperature. Equation 1 describes the rate of change of the Gibbs free energy with respect to component i when P , T_s , and the compositions of all other components are held constant. For an open system held at constant T_s (i.e., $dT_s = 0$) and P ($dP = 0$), the total change in G is written as the sum of individual contributions from all the components.

$$dG = -SdT_s + V_s dP + \sum_i \mu_i dn_i = \sum_i \mu_i dn_i \quad (2)$$

If the system contains two different phases α and β , the total change in G at constant T_s and P is written as

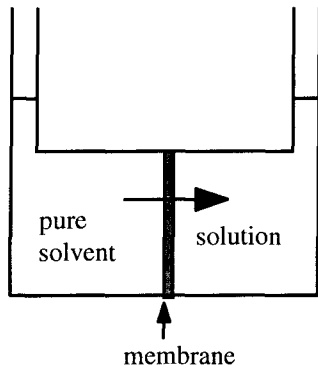
$$dG = dG_\alpha + dG_\beta = \sum_i \mu_{i,\alpha} dn_{i,\alpha} + \sum_i \mu_{i,\beta} dn_{i,\beta} \quad (3)$$

At equilibrium ($dG = 0$) using mass conservation ($dn_\alpha = -dn_\beta$), Equation 3 reduces to

$$\mu_{i,\alpha} = \mu_{i,\beta} \quad (4)$$

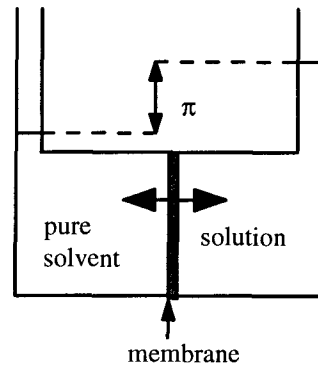
For the membrane system described in Figure 1, Equation 4 is used to illustrate that the chemical potential of solvent in solution and in pure solvent must be equal at equilibrium.

Osmosis



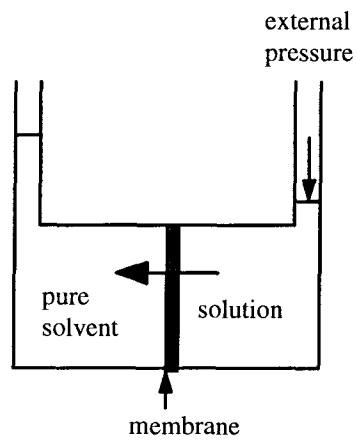
(a)

Osmotic equilibrium



(b)

Reverse Osmosis



(c)

Figure 2.1: Schematic description of osmosis, osmotic equilibrium and reverse osmosis (RO).

The chemical potential of the solvent is expressed as

$$\mu_i = \mu_i^\circ + R_g T \ln(a_w) \quad (5)$$

where μ_i° is the standard chemical potential for solvent ($a_w = 1.0$), R_g is the gas constant, and a_w is the activity of the solvent. The activity is further expressed as

$$a_w = \gamma_w \cdot x_w \quad (6)$$

where γ_w is the activity coefficient and x_w is the mole fraction of the solvent (water). Since the activity is always less than one in solution, the chemical potential of solvent in solution is always less than that of pure solvent. At equilibrium, the induced osmotic pressure π balances the difference in the chemical potential on either side of the membrane. If the chemical potential of solvent in solution at the new pressure $P+\pi$ is $\mu_w(T_s, P+\pi, a)$, then

$$\mu_w(T_s, P + \pi, a_w) = \mu_w^\circ(T_s, P, a_w = 1) \quad (7)$$

or

$$\mu_w^\circ(T_s, P + \pi) + R_g T_s \ln(a_w) = \mu_w^\circ(T_s, P) \quad (8)$$

which can be further deduced to (at constant T_s)

$$\begin{aligned}
-R_g T_s \ln(a_w) &= \mu_w^0(T_s, P + \pi) - \mu_w^0(T_s, P) \\
&= \bar{V}_w(P + \pi - P) = \bar{V}_w \pi
\end{aligned}
\tag{9}$$

where \bar{V}_w is the molar volume of the pure solvent. For a dilute two component solute-solvent system ($x_s \ll 1$), Equation 9 is written as

$$\begin{aligned}
-R_g T_s \ln(a_w) &= -R_g T_s \ln(1 - a_s) \\
&= -R_g T_s \ln(1 - x_s) = R_g T_s x_s = \bar{V}_w \pi
\end{aligned}
\tag{10}$$

where a_s and x_s are solute activity and molar fraction respectively. For dilute solutions,

$$\frac{x_s}{\bar{V}_w} = c_s
\tag{11}$$

where c_s is the molar concentration of the solute; therefore Equation 10 is rewritten as

$$\pi = c_s R_g T_s
\tag{12}$$

Equation 12 describes a linear relationship between solute concentration and the exerted osmotic pressure but is only valid for dilute solutions and for inorganic solutes (van't Hoff law);. For highly concentrated solutions (such as seawater), the magnitude of the higher order terms in the logarithmic expansion (Equation 10) are significant and cannot be ignored; a molar osmotic coefficient ϕ is generally used to account for these additional terms as described in Equation 13 [Robinson, 1955].

$$\pi = \phi \cdot c_s R_g T \quad (13)$$

For solutions containing organic compounds, macromolecular or colloidal material, empirical equations such as the power-law relationship (Equation 14) are more often used.

$$\pi = A + B \cdot c_s + C \cdot c_s^2 \quad (14)$$

2.1.2 Reverse Osmosis

If an external hydrostatic pressure is applied on the more concentrated side, and it exceeds the osmotic pressure exerted by the solution, then the flow of solvent is effectively reversed as shown in Figure 2.1(c); this process is commonly referred to as reverse osmosis (RO). All pressure-driven membrane separation processes function on the basis of application of hydrodynamic pressure as described above, to effect a solute-solvent separation across a membrane barrier; the solvent is forced through the barrier while some or all of the solute is retained on the feed side. No phase change occurs during the process and no heating is necessary [Sourirajan, 1977]. In environmental engineering applications such as water treatment, wastewater treatment and desalination, the solvent is always water and the solute is any of the various contaminants that are normally present in solution. Other membrane processes such as dialysis and electro-dialysis, which use different driving forces such as concentration gradient or electric potential gradient, are also generally included under membrane separation processes; these are not discussed in this work and study is restricted to pressure-driven membrane separation processes.

2.1.3 Classification of Membrane Processes

The classification of pressure-driven membrane separation processes is based either on the physical characteristics of the membrane mainly pore size distribution or on the chemical characteristics mainly membrane material type; both these classifications are briefly reviewed in this section.

a) Pore size distribution

The pore size distribution is the most important factor in selecting a membrane for a specific application. It also influences the solute rejection characteristics of the membrane, solvent flux, operating pressures, and even the nature of the problems that manifest during operation namely membrane scaling, fouling etc. [Parekh, 1988]. Historically, membranes are categorized into microfiltration (MF), ultrafiltration (UF) and reverse osmosis (RO) or hyperfiltration processes. MF membranes are coarse membranes with relatively large pore size distribution with a molecular weight cutoff (MWCO) of 1000 Å to 10µm, and are used to in applications where colloidal and particulate matter removal are important [Belfort, 1994]. Although sharp MWCO is desirable, most membrane cutoffs are gradual, meaning that solutes within a range of molecular weight are partially retained and partially permeated. By convention, a membrane MWCO value means that 90% of spherical uncharged solutes with that molecular weight will be retained on the feed side [Wok, 1992]. UF membranes have intermediate pore size distribution with MWCO of 30 Å to 20,000 Å, and are used in various applications ranging from protein purification in the pharmaceutical and biochemical industries to concentration of whey in the dairy industry to removal of trace

organics, heavy metals and pathogens during water and wastewater treatment. UF membranes are available in several pore size distributions which allows for application in specialized areas; the membranes which are manufactured in the lower MWCO (200 Å and less) are also referred to as nanofiltration (NF) membranes. RO membranes have the lowest pore size distribution with MWCO in the ionic radius range (2 to 20 Å), and were developed originally for desalination purposes. They are also used to remove organics, dissolved solids and pathogens during water and wastewater treatment and various industrial applications.

The mode of transport in the above processes is also markedly different. MF and coarse UF membranes operate mainly on the basis of sieve separation, while NF and RO processes are based on several different mechanisms including diffusion and capillary flow; a detailed discussion on membrane transport is discussed in section 2.2. From an operational standpoint, MF membranes operate at relatively low pressures while UF, NF and RO processes operate at increasingly higher pressures (Table 2.1). This is because in MF and UF processes, solutes that are retained are usually high molecular weight compounds which exert very little osmotic pressure. Consequently, the differences in operating expenditure for each of these processes is significant. From Figure 2, it can also be noted that there is an overlap between each of the processes; this is because some of the above processes are 'tailor-made' for rejection of larger or smaller molecules.

(b) Membrane materials

Membrane materials can be categorized into cellulosic (naturally occurring) and non - cellulosic (synthetic) types [Lloyd, 1985; Lloyd and Meluch, 1985]. Naturally

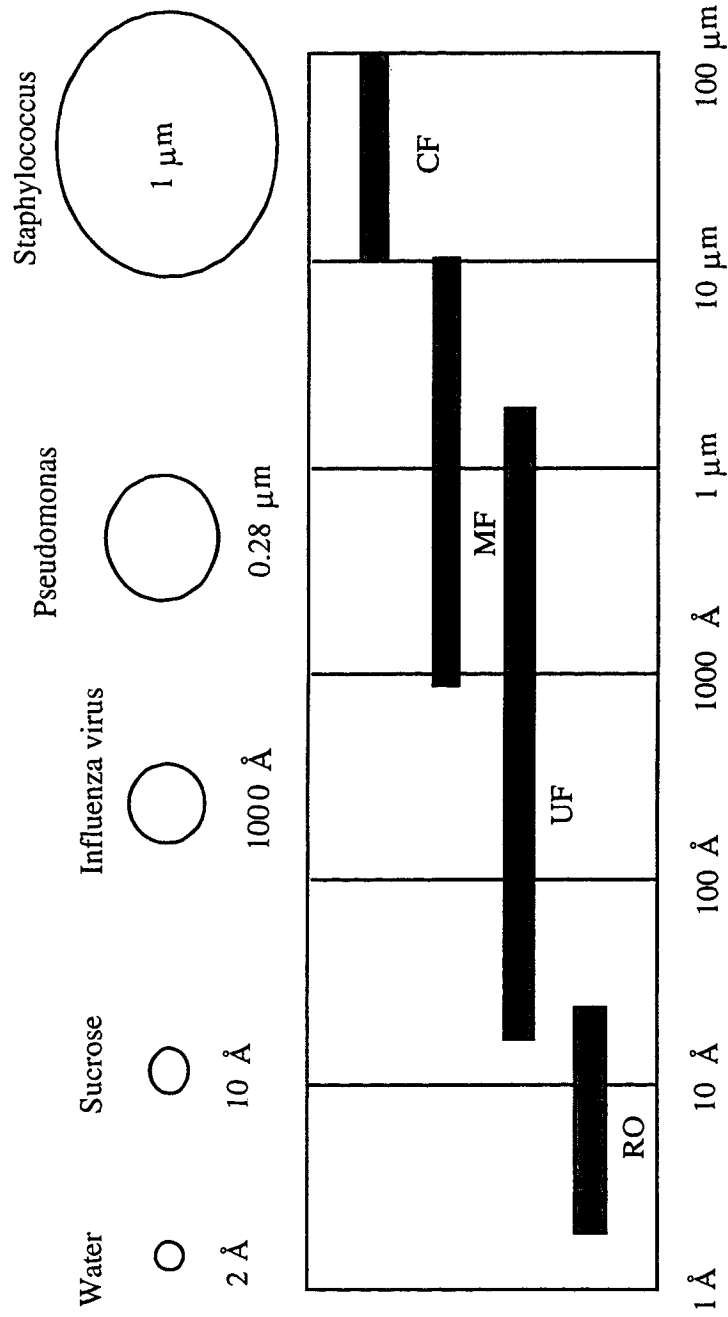


Figure 2.2: Illustration of different pressure driven processes and conventional filtration (CF) based on pore size distribution.

Table 2.1: Size-based classification of membrane processes.

Membrane	Operating pressures (PSI) ¹	Average Flux (GFD ²)	Modular Configuration	Membrane type
MF	50-125	10-15	Hollow-fiber, plate-frame	PA, TFC
UF	75-150	10-12	Spiral-wound, plate-frame, hollow-fiber, tubular	TFC, PA, CA, PS
NF	125-250	7-12	Spiral wound, hollow-fiber	TFC, PA
RO	150-400	8-12	Hollow-fiber, spiral wound, tubular	CA, TFC, PA

¹Pounds per square inch; ² Gallons/day/square feet of membrane area.

occurring membranes are generally biological and contain a lipid structure while synthetic membranes are manufactured from polymers. Cellulose acetate and cellulose tri-acetate are materials commonly used to manufacture cellulosic UF and RO membranes while polyamide and polysulfone membranes are popular synthetic membranes. Some of the important membranes are briefly reviewed in this section. Membranes are also classified as symmetric and asymmetric membranes. Symmetric membranes are 10 to 200 μm thick, and resistance to transfer is determined by the total membrane thickness. Asymmetric membranes have a dense top layer with a thickness of 0.1 to 1.0 μm supported on a porous secondary layer with a thickness of 50 to 150 μm . The top layer dictates the resistance to mass transfer and other membrane characteristics while the porous layer acts only as a support structure. Symmetric membranes generally have low permeate flux while asymmetric membranes dramatically enhance permeate flux. In addition, composite membranes are also commonly used in commercial UF and RO systems. Composite membranes are asymmetric membranes which contain different materials in the dense and porous layers [Parrett, 1982]; this form of casting allows for tailoring the membranes to remove specific contaminants of interest.

Cellulose Acetate (CA) Membrane

Historically, commercial RO membranes were first cast from cellulose acetate [Sourirajan, 1986; Loeb, 1966; Loeb, 1981]; they are still widely used in desalination and wastewater reclamation because of their excellent resistance to chlorine and oxidation. The membrane consists of a polyol made from acetylation of cellulose which consists of long beta-glucoside units (MW 25,000 to 65,000 daltons); the chlorine resistance comes from the cyclo-alipatic rings and the oxygen functionalities. However, the membrane has

a narrow optimum pH range of 5-6 as the ester groups in cellulose acetate are subject to hydrolysis in acidic (pH < 4) and basic (pH > 8) conditions [Wok,1992]. The membrane also has a temperature restriction of 38 °C, and suffers from compaction at high pressures. Another disadvantage of CA membrane is that it is amenable to microbial attack; this is normally prevented by periodic sanitizing or maintaining a steady level of chlorine in the feed (at < 1 mg/L). Cellulose tri-acetate membrane has comparatively improved physical and chemical strength over CA membrane which broaden its range of operating conditions [Cross, 1973; Kesting, 1985].

Polyamide (PA) Membrane

These membranes are cast from polymers that contain the -CN- linkage [Blais, 1977]: examples of polymers include aromatic polyamides (polybenzamides); aromatic polyhydrazides (polybenzhydrazides); aromatic polyureas and polyurethanes; polyvinylpyrrolidones; polyacrylamides; polyamic acids; nylons; and cyclodehydration products such as polybenzimidazoles and polyimides [Blais, 1977]. Examples include the Du Pont B-9 and B-10 permasep permeators [Wok, 1992]. The membranes have strong physical and chemical resistance, operate over a wider pH range (4 to 11) and can withstand higher temperatures than CA membranes. They also have superior rejection characteristics especially with respect to organic compounds [Chian, 1976]. As they are synthetic in nature, they are resistant to bacterial degradation; however, they are susceptible to bacterial growth and fouling [Eisenberg, 1986]. A serious drawback of the polyamide class of membranes is that they are extremely sensitive to chlorine and other oxidizing compounds. It is believed that the amide group is vulnerable to chlorine attack, and the search is still ongoing to modify this functionality to increase chlorine sensitivity

[Glater, 1994]. A few modified membranes have been developed that are less sensitive to chlorine but only at the expense of other membrane characteristics such as rejection and permeate flux [Glater, 1994]. Polyamide membranes are more often used than CA membranes because of their sheer versatility which comes from the numerous polymers that are available for casting.

PA membranes are also available in composite form mostly as thin-film composite (TFC) membranes. The thin film is formed from interfacial polymerization and deposited on a microporous support consisting of polysulfone. In most high performance membranes, the thin films involve aliphatic or aromatic amines condensed with acyl chlorides, isocyanates or other reactive groups; the resulting membranes usually consist of amide or urea linkages. Examples include the FT-30 membrane which is produced by Film-Tech, and the NS-100, NS-200 and NS-300 membranes pioneered by the North Star Research Institute (Chian, 1973). These membranes also have superior physical and chemical characteristics and operate over a very wide pH range; however, they are still susceptible to attack from chlorine and other strong oxidants such as ozone.

Polysulfone (PS) Membranes

Though polysulfone is widely used in fabricating the porous support layer in TFC membranes, it is also used in making UF membranes [Lloyd, 1985]. However, the PS membrane is not markedly superior to PA or TFC membranes; in addition, the membrane suffers compaction and degradation at elevated pressures and temperatures, and is incompatible with aromatic and chlorinated hydrocarbon solvents, and esters and ketones [Cadotte, 1981].

2.1.4 Commercial Membrane Modules

The role of membrane modules is to provide structural support and flow separation for the membranes [Strathman, 1984]. The support includes external housing, and compaction resistant backing and spacing. The objectives of the module design are to separate the feed and reject (concentrate) streams from the permeate (product) stream, provide maximum membrane surface area for separation, and optimum hydrodynamic design for fluid flow and controlling fouling and CP. The modules are generally fabricated from stainless steel, plastic and fiber-glass in order to withstand high operating pressures; the module must be able withstand pressures ranging from 200 psi to 1500 psi depending on the type of membrane that is used. The module should also exhibit resistance to mechanical forces such as abrasion, scouring and membrane compaction. The module should also be compatible with feed/reject streams and other chemicals that are used during pretreatment. The module should ideally have minimum holdup volume so that bacterial growth is minimized.

The hydrodynamic design of the module is as important in controlling the overall performance of the unit as the selection of membrane type and material. A proper module design should maintain good flow control of the feed solution at the membrane surface in order to minimize CP and fouling. Ideally, the module should allow for easy physical and chemical cleaning. Most commercial membrane modules are available in four different configurations: tubular, plate-frame, hollow-fiber and spiral-wound membranes. Of these, the hollow-fiber and spiral-wound membranes are popular and dominate the present membrane market because they are compact and pack considerable membrane

material. Each configuration is briefly discussed, but the emphasis is placed on spiral-wound membranes.

Tubular membranes

Tubular modules generally have the membrane inside a porous support tube; one membrane module can contain up to 30 tubes and can be up to 6m (20 feet) long. The support tubes are normally constructed from stainless steel. The main advantage of this type of configuration is that it is easy to operate, and can handle feed solutions with high concentrations of solids and other fouling compounds. Mechanical cleaning is possible in tubular modules, and membranes can be individually replaced thus minimizing membrane replacement costs. Historically, membranes were first installed and operated in tubular modules; they are still used in the food processing, and paper and pulp industries, for treating highly contaminated streams. The other main advantage of the module is that its diameter is large enough (about 0.5 inches for RO and UF applications) to maintain turbulent conditions without a large pressure drop; this minimizes the negative effects of solute accumulation near the surface of the membrane. The main disadvantage of the tubular configuration is that it has low membrane packing density and therefore requires high capital costs. These membranes also operate at low recoveries because they need high holding volume per unit area of the membrane. Its application in wastewater reclamation and desalination is very limited.

Plate-frame module

This configuration is modeled after the conventional filter press [Aeroget General, 1966]. Porous supporting disks, with membranes placed on each side, are stacked with spacers in between and held together by external tie bolts in a housing unit. The brine flow takes place in the space between the disks, and the product flows through the membrane into the porous support structure flowing outwardly (or inwardly) to a product water outlet. This module can accommodate significantly more membrane material than tubular module; however the membranes are more susceptible to fouling because many stagnant zones exist, and the module itself is difficult to clean because of the mechanical arrangement. The module has low membrane packing density and is therefore expensive. It is primarily used to produce potable water in small-scale applications; its application in reclamation and desalination is limited.

Hollow-fiber module

This configuration uses thousands of small fibers with diameter in the range of 5 to 100 microns, with the ends sealed into headers; the typical diameter to wall thickness ratio is 3-5 to 1. The fibers are bundled together and potted into an epoxy material. The water flows from the outside of the fiber into the inside where it is taken off at the opposite end of the feed entrance. The main advantage of the hollow-fiber configuration is that it packs the largest amount of membrane per unit volume, while retaining the mechanical strength required to sustain the high operating pressures; naturally, this results in low capital expenditure. The disadvantage of this type of configuration is that it cannot tolerate the presence of suspended solids in the feed stream; consequently the feed has to be highly pretreated to avoid membrane clogging. Hollow-fiber modules have been

extensively used in desalination and water treatment applications, but their use in wastewater reclamation has been limited.

Spiral-wound module

Spiral-wound membranes are ideal for applications where the feed stream is contaminated or has a considerable fouling potential; they have found widespread application in desalination, wastewater reclamation, water treatment and other chemical and biochemical industries. The membrane consists of a sealed envelope of two membranes with a product water spacer in between, and a feed brine spacer between two successive envelopes [Ohya, 1975]. The envelope is sealed on three sides, with the fourth edge open and sealed to a perforated product water collection tube on which the envelope is wrapped. The feed spacer which is usually 1-2 mm thick, permits adequate mixing. The feed enters the spacers and across the membrane in tangential flow while the permeate enters and exits through the inner product water collection tube. Spiral-wound membranes have several advantages over other membrane configurations: they have very low holding time and therefore can be operated at relatively high recoveries (50-90%); they have very high membrane packing capacity and therefore installation costs are relatively low; they also tolerate feed solutions with moderate suspended solids concentration. They are widely used in the RO industry because of its high surface area but its use in UF/MF is limited as it can handle only moderate suspended solids, and CP and fouling are difficult to control [Blatt, 1976]. The product water recovery per element is usually around 15% of the feed flow rate, and the pressure drop between the inlet and exit ports is approximately 5-10% per element.

2.1.5 Membrane Applications

The development of new spiral-wound and hollow-fiber membranes which can tolerate wide pH ranges, higher temperatures and more corrosive feed characteristics, and which operate at lower pressures with superior solute rejection and permeability characteristics has resulted in many applications for membrane processes. From traditional applications such as seawater and brackish water desalination to special applications for chemical and biochemical industry, membrane processes are increasingly becoming the treatment process of choice. There is vast information in the literature on membrane applications, and several books are available that tackle this topic in detail [Scott, 1981; Eisenberg, 1986; Parekh, 1988; and Heitmann, 1990]. Some of the important applications of membranes are summarized in Table 2.2 with selected references.

2.2 Membrane Transport

2.2.1 Fundamental equations

A generalized membrane separation system is shown in Figure 2.3; the most important characteristics of such a system are solvent flux and solute rejection. The solvent or water flux (J_w), which is defined as the volume of water passing through an unit area of the membrane is usually expressed as [Lonsdale, 1965]:

$$J_w = A(\Delta P - \Delta \Pi) \quad (15)$$

Table 2.2: Selected applications of membrane processes

Membrane	Application	Selected References
Microfiltration	Water treatment	Anselme [1994]
	Wastewater treatment	Pillay [1994]
	Industrial applications	
Ultrafiltration	Dairy	Rosenberg [1995]
	Water treatment	Comb [1994], Anselme [1994]
	Wastewater reclamation	Westerhoff [1994] Madireddi [1996]
	Industrial applications	
	Biochemical Protein purification	Milliseme [1994] Milleseme [1994]
Nanofiltration	Water treatment	Liu [1987], Weisner [1994], Jacangelo [1995]
	Wastewater reclamation	Madireddi [1996]
	Industrial applications	
Reverse Osmosis	Dairy	Rosenberg [1995]
	Desalination	Scott [1981], Marquardt [1990]
	Wastewater reclamation	
	Potable reuse	Argo [1979], Winfield [1979] Westerhoff [1994] Suzuki [1991]
	Recreational reuse	Edwards [1990]
	Irrigation	Wethern [1995], Smith [1995]
	Industrial reuse	

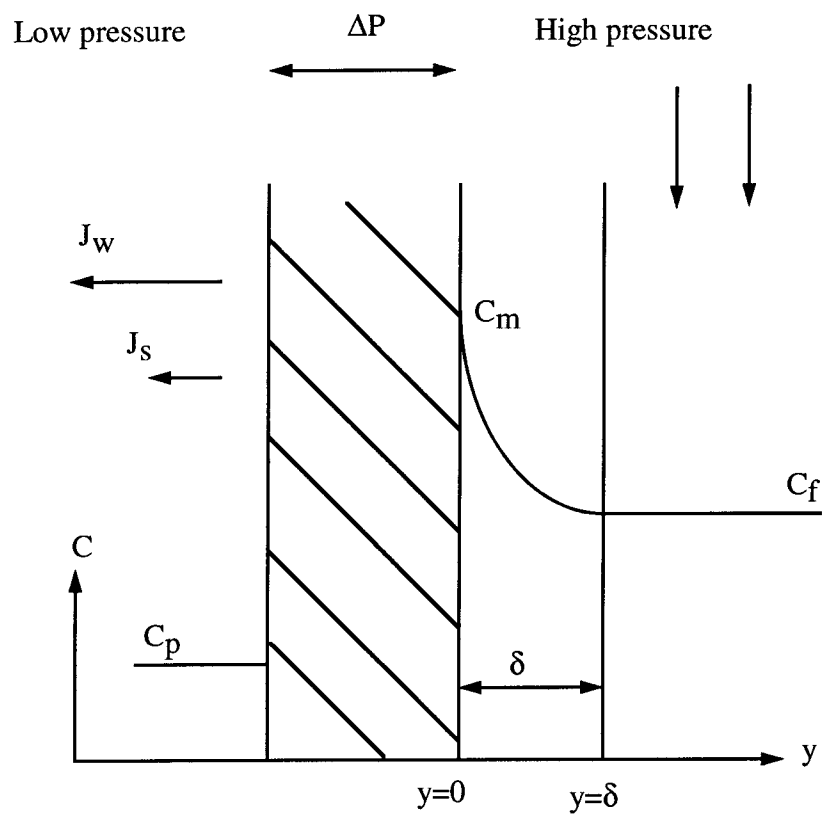


Figure 2.3: Schematic of a generalized membrane process.

where A is membrane permeability, ΔP is applied pressure difference and $\Delta \Pi$ is the osmotic pressure difference across the membrane surface. The solute rejection (R) is defined as [Barger, 1991]:

$$R = \frac{c_f - c_p}{c_f} \quad (16)$$

where c_f is the feed side solute concentration and c_p is the permeate side solute concentration. Solute rejection is generally a function of the salt flux (J_s) which is expressed as

$$J_s = B(c_m - c_p) \quad (17)$$

where B is the salt permeability, and c_m is the solute concentration at the membrane surface. The solute concentration at the membrane is usually greater than in the bulk solution due to polarization effects. The other important term that often appears in the context of membrane performance is solvent recovery (rec) which is defined as the percent ratio of the permeate flow (Q_p) to the feed flow (Q_f).

$$rec \text{ (as \%)} = \left(\frac{Q_p}{Q_f} \right) \times 100 \quad (18)$$

The equations expressed in the preceding paragraph are based on the popular solution-diffusion model [Lonsdale, 1965]. This and other important transport models are briefly reviewed in the following section.

2.2.2 Models for Membrane Transport

Models for RO transport are classified under two categories: (1) irreversible thermodynamic models which assume a black box approach and relate constituent fluxes across the membrane to generalized driving forces [Kedem, 1958; Speigler, 1966], and (2) models that assume a specific mode of solute and solvent transport within the membrane [Lonsdale, 1965; Merten, 1966; Kimura, 1967; Belfort, 1976]. In most of these models, the form of equations used to express solute and solvent fluxes is similar; it is only the coefficients (water and solute permeability) which are differently expressed. While excellent reviews of these models are available in literature (Soltanieh, 1981; Pusch, 1986), a brief review of the important models is presented in this section:

Irreversible Thermodynamics Model

The model of Kedem and Katchalsky [1958] relates the flow of each component in a system to the constituent forces which are acting on it; the model assumes the validity of linear laws and the Onsager Reciprocal Relationships. For membrane systems, assuming dilute solutions, the solvent (J_v) and solute (J_s) fluxes are related to their respective driving forces as

$$J_v = L_p(\Delta P - \sigma\Delta\Pi) \quad (19)$$

$$J_s = (c_s)_{in}(1 - \sigma)J_v + \omega\Delta\Pi \quad (20)$$

where $(c_s)_{ln}$ is the logarithmic mean average of the solute concentration across the membrane, σ is the reflection coefficient, L_p is the filtration coefficient, and ω is the solute permeability. It should be noted that J_v in equation 18 and J_w in equation 14 represent the same flux. The value of σ which ranges from 0 to 1, indicates the degree of solute-solvent flow coupling, with $\sigma = 1$ representing complete absence of any coupling. This model was further modified by Speigler and Kedem (1966) to account for large solvent volume flux and steep concentration gradients.

Solution-Diffusion Model

This model developed by Lonsdale [1965] assumes that both the solute and solvent dissolve in the nonporous and homogeneous surface layers of the membrane and then diffuse across it in an uncoupled manner due to respective chemical potential gradients ($\sigma = 1$); the gradients are assumed to be a result of temperature and concentration gradients across the membranes. The principal driving force for the solvent is assumed to be the pressure gradient, while for the solute it is the concentration gradient. Equations 15 and 17 show the relationship between solvent (water) and solute fluxes and their respective driving forces.

Solution-Diffusion-Imperfection Model

The model (Sherwood, 1967) is an extension of the previous model, and incorporates both diffusion and pore flow for solute and solvent transport across the membrane. The equations of solvent and solute fluxes are given as

$$J_v = A(\Delta P - \Delta \Pi) + (K_3 \Delta P)c_m \quad (21)$$

$$J_s = B(c_m - c_p) + (K_3 \Delta P)c_m \quad (22)$$

Finely Porous Model

In this model, permeation is considered to occur by viscous flow through pores, with flow hindrances described by attractive or friction forces [Merten, 1966]. The solute and solvent permeate the membrane through pores which connect the high pore and low pore faces of the membrane. The model is useful in describing transport in coarse UF and MF membranes.

Preferential Sorption-Capillary Flow Model

The model is based on generalized capillary flow model involving viscous flow for water transport, pore diffusion for solute transport, and film theory for boundary layers [Kimura, 1967]. Both the solute and water tend to permeate through the micropores of the membrane but it is assumed that water is preferentially adsorbed onto the pore walls and the solute is rejected at the surface for physico-chemical reasons. The basic equations of this model are similar to the solution-diffusion model except that the concentration at the membrane surface in the feed side is related to the bulk concentration using the film theory. In addition, explicit expressions are provided for water and solute permeability coefficients in terms of operating conditions such as feed pressure, concentration and temperature.

2.3 Concentration Polarization (CP) and Fouling

2.3.1 Basic Definitions

Concentration Polarization (CP)

The accumulation of solute near the membrane surface is generally referred to as concentration polarization (CP) [Matthiasson, 1980; Potts, 1981]. During the initial transient state, the solute molecules are transported to the membrane surface via advection as shown in Figure 2.4 (b); as accumulation of solute takes place, the advective transport is balanced by back diffusion, and at steady state a concentration profile exists as shown in Figure 2.4(c). CP as mentioned before leads to serious problems during membrane operation as it increases the overall resistance to solvent (water) flux. Some of the important negative effects of CP are:

1. A considerable decrease in membrane water flux resulting from increased resistance to flow. In RO systems, the increase in solute concentration induces greater osmotic pressure and therefore decreases the net driving force [Sourirajan, 1970]; for coarse membranes such as UF and MF, the increase in osmotic pressure component is negligible as the solute is generally either a macromolecule or a colloidal particle. However, there is still a net loss in flux as the solute particles offer resistance in the form of cake or gel layers [Bowen, 1995]. Matthiason and Sivik [1980] report that most commercial membrane plants operate at 2-10% of trans-membrane fluxes for pure water.

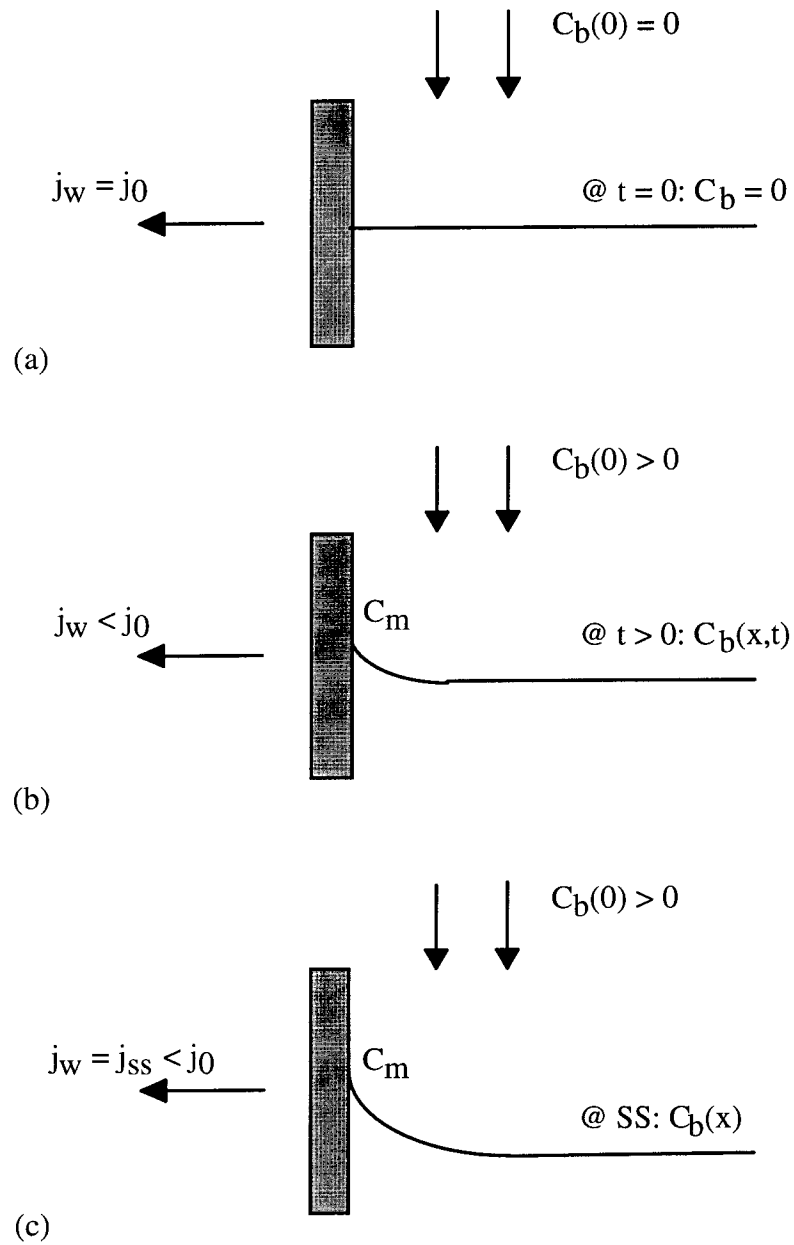


Figure 2.4: Development of concentration polarization (CP) in membrane processes: (a) initial state; (b) transient state; and (c) steady state.

2. The second important effect of CP is an increase in solute concentration in the permeate. Solute flux is directly proportional to the difference in salt concentration across the membrane $c_m - c_p$ (Equation 16); as c_m increases due to CP, the net solute flux also increases thus decreasing the permeate quality.
3. The third effect of CP is an increase in the likelihood of fouling. If the solute is a sparingly soluble inorganic compound such as CaSO_4 , the low solubility will cause precipitation fouling. In other cases where the feed water is contaminated by microbial matter, bacterial fouling and degradation is a major problem [Ridgway, 1985]. CP is a major aggravating factor in colloidal fouling of UF and MF membranes. CP also induces formation of gels during separation of macromolecular solutes during UF and MF treatment; these gels act as additional barriers to solvent flux, and are often difficult to clean [Belfort, 1984]. Other important consequences of CP include its effect on the durability and life-span of the membrane, and changes in the rejection characteristics of the membrane. In order to deal with CP, it is necessary to understand the transport phenomena at the membrane surface.

Fouling

Fouling is a complex phenomena that results in long term solvent flux decline (from few hours up to several months). The most informative and broadly applicable definition was given by Eykamp [1976]. 'Fouling is a condition in which a membrane undergoes plugging or coating by some element in the stream being treated, in such a way that its output or flux is reduced and in such a way that the foulant is not in dynamic equilibrium with the stream being filtered. In other words, something has occurred that makes the micro-environment near the membrane surface a non steady state situation'.

It is classified as follows depending on nature of solute that causes fouling (foulant) [Epstein, 1979; Potts, 1981]:

1. Precipitation and inorganic fouling
2. Particulate and dissolved organic matter fouling
3. Biological fouling

Gel formation is also considered to be a form of fouling by some authors [Kimura, 1975; Merson, 1976; Bhattacharya, 1978] but it is classified as a form of CP in this study. A more detailed review of fouling in membranes is given in section 2.3.3.

The general effects of fouling are similar to that of CP. There is a decrease in the solvent flux, and the quality of the permeate over time; in addition, the durability and life-span of the membrane is also negatively affected [Potts, 1981]. However, a major difference between CP and fouling is that the latter causes problems that are irreversible; thus preventive measures undertaken in the form of pretreatment with anti-foulants and anti-scalants are preferred to administering periodic cleaning. These measures are discussed in more detail in section 2.4.4

2.3.2 Fundamental Models for CP

A number of mathematical models are available to predict CP depending on the type of separation (UF, RO etc.), solution characteristics and ambient conditions; generally, simplifying assumptions are made to obtain a mathematical solution. Though

several detailed reviews are available in literature on modeling CP in membranes [Matthiason, 1980; Potts, 1981; Jonsson, 1984; Wakeman, 1986; Davis, 1992; and Bowen, 1995], the important models are reviewed in this section. Some of the models are more applicable to NF and RO systems (e.g. osmotic pressure model) while others are more representative of UF and MF systems (e.g. filtration model). The models reviewed in this section only represent solute-solvent behavior for simplified membrane systems (for example, dead-end filtration) with well defined boundary conditions; these are further used in conjunction with global transport equations to predict solvent flux behavior in commercial systems such as the spiral wound or hollow fiber module.

Thin-film model and CP dynamics

The basic formulation of CP is for the simple case of a steady one-dimensional system [Jonsson, 1984]; material balance for the solute is expressed as [Figure 2.3]

$$J_s = c_p J_v = c J_v - D_s \frac{dc}{dy} \quad (23)$$

subject to the following boundary conditions

$$c = \begin{cases} c_b & \text{at } y = 0 \\ c_w & \text{at } y = \delta \end{cases} \quad (24)$$

where D_s is the solute diffusion coefficient, c_b is the bulk solute concentration and is equivalent to c_p , c_w is the membrane surface (wall) concentration, J_v is the water volume

flux across the membrane (permeate flux) and δ is the thickness of the boundary layer. Integration and rearrangement leads to

$$\frac{c_w - c_p}{c_b - c_p} = \exp\left(\frac{J_v}{k}\right) \quad (25)$$

where k is the mass transfer coefficient equal to D/δ . The CP modulus M is given as

$$M \equiv \frac{c_w}{c_b} = \frac{\exp\left(\frac{J_v}{k}\right)}{R + (1-R)\exp\left(\frac{J_v}{k}\right)} \quad (26)$$

Appropriate correlations exist for calculating the mass transfer coefficient depending on the nature of flow; for turbulent conditions, it is based on the Chilton-Coburn analogy [Brian, 1966] and the Blasius formula for friction factor [Bird, 1960], while for laminar conditions similar expressions have been offered by Groeber [Belfort, 1984]. The correlations are usually are of the form

$$Sh = \frac{k \cdot d_h}{D_s} = K \cdot Re^a \cdot Sc^b \left(\frac{d_h}{L}\right)^c \quad (27)$$

where the constants Re , Sh and Sc are the Reynolds, Sherwood and Schmidt numbers respectively, d_h is the hydraulic diameter, and K , a , b , and c are constants calculated based on the flow regimes previously described.

Unsteady-state formulation (Thin-film model)

This form of formulation is useful in understanding the time periods involved in the development of CP. Unsteady-state build-up of CP has been studied for both RO and UF systems in batch cells [Matthiason, 1980, Fane, 1986]. In one dimensional unstirred batch cell that is assumed to be semi-infinite, the equation for mass balance is

$$\frac{dc}{dt} = |J_v| \frac{dc}{dy} + D_s \frac{d^2c}{dy^2} \quad (28)$$

with the initial and boundary conditions

$$c(0, y) = c_b \quad (29a)$$

$$c(t, \infty) = c_b \quad (29b)$$

$$|J_v|c(t, 0) = (1-R) |J_v|c(t, 0) - D_s \frac{dc(t, 0)}{dy} \quad (29c)$$

The solution for Equation 28 for $R = 1$ is [Dresner, 1964]:

$$M \equiv \frac{c_w}{c_b} = 2 - \left(1 + \frac{\theta}{2}\right) \operatorname{erfc}\left(\frac{\sqrt{\theta}}{2}\right) + \sqrt{\frac{\theta}{\pi}} \exp\left(-\frac{\theta}{4}\right) + \theta \quad (30)$$

where

$$\theta = \frac{J_v^2 t}{D_s} \quad (31)$$

For large times, Equation 30 describes a linear relationship between CP modulus and time. The same equations were solved for non-ideal membranes ($0 < R < 1$) by Raridon [1966]:

$$M \equiv \frac{C_w}{C_b} = 1 + \frac{1}{1-R} \left[(R-\phi)(2R-1)\exp(\theta \cdot R(R-1)) \right] + \frac{1}{2(1-R)} \left[|2R-1|\exp(\theta \cdot R(R-1))\operatorname{erfc}\left(\frac{\sqrt{\theta}}{2}|2r-1|\right) - \operatorname{erfc}\left(\frac{\sqrt{\theta}}{2}\right) \right] \quad (32)$$

where

$$\begin{aligned} \phi &= 1 \quad \text{when } R \geq 0.5 \\ \phi &= 0 \quad \text{when } R < 0.5 \end{aligned} \quad (33)$$

For a stirred batch cell system, it is assumed that the bulk liquid is completely turbulent and no concentration gradient exists, and that a thin laminar film exists over the membrane surface which offers the entire resistance to flow. The governing equation is still defined as in the unstirred batch cell system (Equation 28), but a boundary condition is defined at the edge of the boundary layer as

$$c(t, \delta) = c_b \quad (34)$$

The initial condition and the boundary condition at the membrane surface remain the same. The solution in this case is [Fane, 1986]

$$M \equiv \frac{c_w}{c_b} = \exp\left(\frac{J_v \delta}{D_s}\right) + \sum a_n \exp(-\lambda_n^2 t) X_n\left(\frac{\lambda_n^2 D_s}{J_v^2}, \frac{J_v \delta}{D}\right) \quad (35)$$

where λ_n and X_n are the eigen values and eigen functions of the solution.

Gel Polarization (GP) Model

In most solute-solvent separation systems, it is reasonable to expect that the numerical value of M cannot increase indefinitely and that after a certain degree of accumulation of the solute at the membrane surface, either precipitation or gellation will occur (Figure 2). In the case where the solute is a macromolecule such as proteins, the solution behaves more as a gel at high concentrations; this is the main assumption of the gel polarization (GP) model [Michaels, 1968, Blatt, 1970]. The concentration of the solution at the membrane surface does not increase after a certain gelling concentration c_g . However as the gel develops, it offers additional resistance to fluid flow and at steady state the convective transport of solute to the membrane surface is counter balanced by the diffusive back transport, which is limited by the gel concentration c_g . The limiting flux was given as follows by Michaels [1968] employing a mass transfer coefficient:

$$J_{vlim} = k \cdot \ln\left(\frac{c_g}{c_b}\right) \quad (36)$$

The salient features of this model are that the limiting flux is:

1. independent of the applied pressure
2. related to semi-logarithmically to the bulk concentration
3. approaches zero at a limiting bulk concentration which is equal to the gel concentration.

Low pressure

High pressure

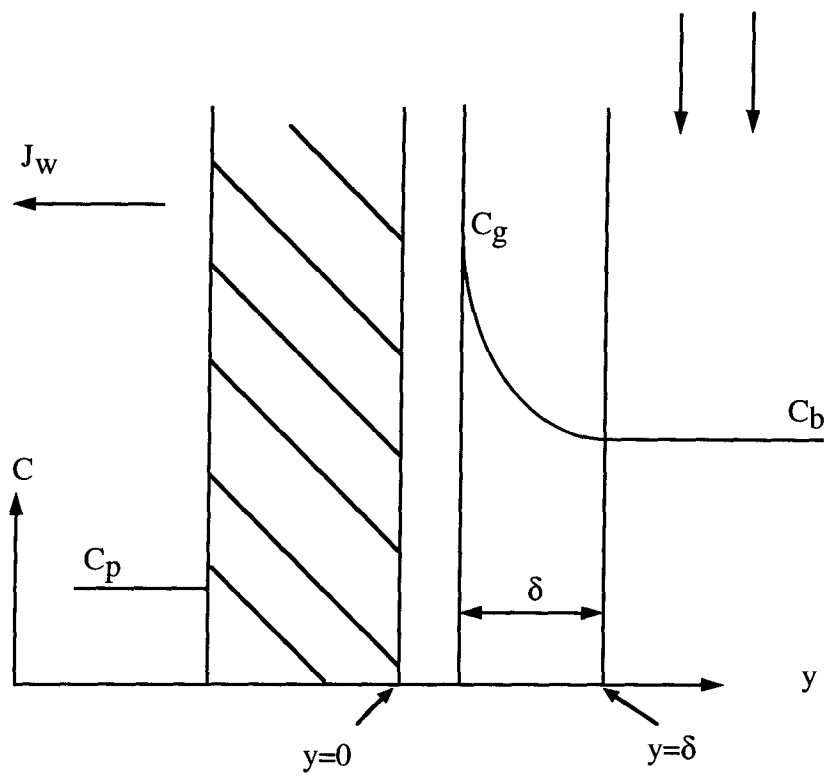


Figure 2.5: Schematic description of the gel polarization model

Many experimental studies [Porter, 1972a,b, Goldsmith, 1971, Henry,1972 and Madsen, 1977] on macrosolute and colloidal ultrafiltration have obtained results that confirm some of qualitative predictions of the model. The mass transfer solution is evaluated using the Leveque solution [Porter, 1972], and is of the following form for laminar conditions.

$$\text{Sh} = \frac{k \cdot d_h}{D_s} = 1.62 \left(\text{Re} \cdot \text{Sc} \cdot \frac{d_h}{L} \right)^{0.33} \quad (37)$$

For turbulent conditions, the mass transfer coefficient is evaluated using the following empirical relationship:

$$\text{Sh} = \frac{k \cdot d_h}{D_s} = K \cdot (\text{Re}^a \cdot \text{Sc}^b) \quad (38)$$

where K, a, and b are constants determined experimentally [Matthiason, 1981]. As in the case of the thin-film model, the gel polarization model was extended for studying stirred and unstirred batch cell UF systems [Trettin, 1980]; it was shown that solvent flux varied inversely with the square root of time.

Though the gel polarization model is qualitatively sound, there are some experimental discrepancies that are difficult to explain. Porter [1972] reported that for ultrafiltration of human albumin in spiral flow channel plates with 10 mm and 30 mm channel thickness for laminar and turbulent flow, the plots of flux versus bulk concentration gave different gel concentrations; a fact that cannot be reconciled by the model. Nakao [1979] reported similar results for macromolecular solutions; they found that gel concentrations were a function of bulk concentration and cross-flow velocity.

They also reported that at bulk concentration equal to gel concentration (as calculated from extrapolation of flux versus $\ln c_b$ plots), the permeate flux was not zero as predicted by the model. In other studies involving colloidal solutions, the permeate flux was several times greater than predicted by the model and is referred to as the flux paradox [Blatt, 1970]; this will be addressed in greater detail in the next section on alternative CP models. Fane [1981] observed that different limiting flux values were obtained when membrane properties such as permeability were changed; this is also in contradiction to the predictions of the model. In spite of these limitations, the model is still used because it is convenient from a practical point of view [Fane, 1986].

Osmotic Pressure Model

This model is based on the assumption that when M reaches high values (10-100), the osmotic pressure effects cannot be neglected in describing CP. In fact, osmotic pressure effects dominate in the operation of RO systems where the solutes are generally inorganic dissolved solids. Equation 18 describes the solvent flux based on Kedem and Katchalsky model [1958]. In addition, the van't Hoff infinite dilution relationship is used to relate the osmotic pressure with the solute concentration (Equation 12).

Equations 12 and 18 are generally used along with mass balance equations to predict CP and flux behavior; for RO systems, the osmotic pressure model is frequently the only model that is used along with the mass balance equations to predict CP [Kleinstreuer, 1984]. The model is also used to predict flux behavior in UF systems provided gelation does not occur [Goldsmith, 1971; Leung, 1979; Vilker, 1981]. As in the case of the thin-film model, the osmotic pressure model has been used along with

mass balance equations and presented for stirred and unstirred batch UF systems of low and medium molecular weight macrosolutes including BSA and Dextran [Vilker, 1981, Jonsson, 1984]; it was shown that the solvent flux was limited by the osmotic pressure and decreased with square root of time ($t^{-1/2}$) for the case of unstirred system. In an interesting analysis of UF membranes, Wijmans and co-workers [1984] showed that the osmotic pressure model and the gel polarization model were conceptually similar [Denisov, 1994]. This was proven by analyzing the relationship between solvent flux and its derivatives with parameters such as the applied pressure difference ΔP , the bulk concentration c_b and membrane resistance R_m . Furthermore, it was shown that lower values of R_m lead to more pronounced osmotic pressure effects, and that membrane resistance has diminishing importance as osmotic pressure effects increase.

Cake Filtration Model (Resistances Models)

This model [Fane, 1986] is important when the solute behaves as a particle and forms a cake layer on the feed side of the membrane. The cake then offers resistance which can be related to solute properties through Carmen relationship

$$R_s = \frac{\alpha V c_b}{A_m} = \frac{\alpha M_s}{A_m} \quad (39)$$

where α is the specific resistance of the cake, M_s is the mass of solute and A_m is the membrane area. α is given as

$$\alpha = \frac{180(1-\epsilon)}{\rho_s d_s^2 \epsilon^3} \quad (40)$$

where ε is the cake porosity, ρ_s and d_s are the density and diameter of the particle respectively. The permeate flux is then rewritten as

$$J = \frac{\Delta P}{(R_m + R_s)\mu} \quad (41)$$

where R_m is the membrane resistance, and μ is the viscosity of the solvent. The above equations were also used to solve CP dynamics for stirred and unstirred batch cell systems assuming the cake resistance develops over time [Chudacek, 1984]. The total resistance to solvent flux is assumed to be the sum of membrane and cake layer resistances; it was shown that solvent flux varied inversely with square root of time as in the case of the gel polarization model.

Other resistance models have also been postulated such as the gel polarization resistance model [Fane, 1986], which combines membrane, boundary layer and gel layer resistances to obtain the overall limiting flux (Equation 42), and the boundary layer resistance model [Wijmans, 1985], which assumes no gel-formation and combines membrane and boundary layer resistances to obtain overall limiting flux.

$$J = \frac{\Delta P}{(R_m + R_{bl} + R_g)\mu} \quad (42)$$

Alternative models

The model by Green and Belfort [1980] is applicable to colloidal and particulate suspensions; they extended the gel polarization model to include lateral migration (also

known as the ‘tubular pinch effect’). Lateral migration describes the tendency of neutrally buoyant spherical particles to move away from the membrane surface when subjected to cross flow; this accounts for the drastic over-prediction of flux decline by the gel polarization model during UF separation of colloidal and particulate suspensions [Blatt, 1970]. The permeate flux for tubular geometry, steady state conditions, laminar flow and constant axial velocity (u) is given as:

$$J_p = \left[1.295 \left(\frac{D_s^2}{Ld} \right)^{1/3} \ln \left(\frac{c_w}{c_b} \right) \right] u^{1/3} + \left[\alpha \kappa^2 \left(\frac{a}{v} \right) \left(1 - \frac{r^*}{d} \right) \right] u^2 \quad (43)$$

Diffusive term

Lateral migration term

where d is the tube radius, L is channel length, $\kappa = a/d$, a being the particle radius, r^* is the equilibrium position towards which the particles migrate, v is the kinematic viscosity of the solvent and α is an empirical constant. One limitation of the model is that it does not address solution chemistry such as ionic strength and pH. Nevertheless, experimental evidence supports the model for macromolecular and colloidal suspensions [Porter, 1972]. Altena and co-workers [1983] further extended the lateral migration concept for a range of conditions and different geometries. They concluded that particles with radius larger than $1 \mu\text{m}$ will be affected by lateral migration, a claim that matched the experiments involving hollow fiber ultrafiltration of blood with a cell size of $8 \mu\text{m}$ [Bauser, 1982].

Zydney and Colton [1986] proposed a CP model based on the film theory model and the classical Leveque solution for mass transfer. They incorporated a shear-induced hydrodynamic diffusivity based on the experiments of Eckstein [1977] instead of Stokes-Einstein particle diffusivity; shear induced hydrodynamic diffusion is a process that involves re-entrainment of solute particles into the bulk liquid under shear stress induced by the cross-flow [Leighton, 1987]. The model predictions matched experimental data for microfiltration of twelve different particulate suspensions [Zydney, 1986]. Other shear-induced hydrodynamic diffusion models include those by Davis and Leighton [1987], Romero and Davis [1988], and Davis and Sherwood [1990]; these models explain transient and steady-state CP and permeate flux behavior for microfiltration and ultrafiltration of particulate and macromolecular suspensions.

Recently Song [1995] developed a theory for explaining CP for a generalized solute-solvent separation in cross flow filtration systems. A dimension-less number called the filtration number (N_F) defined as

$$N_F = \frac{4\pi a_p^3 \Delta P}{3k'T_s} \quad (44)$$

is used in determining the factors that control CP. In equation 20, k' is the Boltzmann constant, a_p is the particle radius and T_s is the absolute temperature. They suggested that a critical value of N_F exists below which only CP layer exists, and above which an additional cake layer is formed. The flux is directly related to the applied pressure and the total resistance to flow. The theory was extended to include both concentrated and dilute suspensions, by modifying the Stokes equation for pressure drop across the

accumulated particle layer, through a correcting function according to Happel's Cell Model theory.

2.3.3 Models for Membrane Fouling

Models for long term flux decline are generally either empirical or semi-empirical in their approach because of the complexity that is involved in all fouling phenomena [Wakeman, 1986]. The models are also generally specific to nature of the foulant; for example, the kinetic growth model is aimed at explaining iron oxide colloids fouling while the resistances model is more suitable for macromolecular fouling, and precipitation models are used to describe inorganic fouling.

The simplest form of relationship that is used widely in RO applications is

$$J_f = J_i \cdot t^n \quad \text{where } n < 0.0 \quad (45)$$

where J_f is the fouled permeate flux and J_i is the original unfouled permeate flux. However, a major limitation in this relationship is that flux asymptotes to zero flux whereas real systems tend to approach a stable non-zero value [Fane, 1980].

Resistances model as described in section 2.5.2 is also used to describe long term flux decline; the following relationship is used to describe permeate flux.

$$J = \frac{\Delta P}{(R_m + R_{bl} + R_d)\mu} \quad (46)$$

R_d is the fouling layer resistance and is described by empirical time-dependent expressions [Wakeman, 1986].

$$R_d = \frac{\alpha_d m_d}{A_m} = \alpha_d M_d \quad (47)$$

where α_d is the specific resistance of the deposit, and M_d is the mass of the foulant deposited per unit area of the membrane.

The model by Kimura and Nakao [1975] is a modification of the gel polarization model as reviewed in section 2.5.2. They defined fouling as a competitive process between deposition and removal:

$$\frac{dM_d}{dt} = r_d - r_e \quad (48)$$

where r_d and r_e are the rate of deposition and removal respectively. The latter two terms were expressed in terms of the gel polarization model as

$$\frac{dM_d}{dt} = Jc_b - kc_b \ln\left(\frac{c_g}{c_b}\right) \quad (49)$$

The above equation was non-dimensionalized and solved for UF and low pressure RO membranes; however, the authors did not verify the model with experiments. The model simplifies to the standard gel polarization model for steady state conditions.

The model by Gutman [1977] also utilizes Equation 48 but provides expressions for r_d and r_e in terms of Reynolds Flux J_R ($J_R = J + k/2$) and turbulence burst mechanism respectively. The removal of solute from the fouling layer is ascribed to turbulence bursts that sweep down into the laminar sub layer and remove small portions of it. This rate is found to occur at regular time intervals proportional to μ/τ_w where τ_w is the wall shear stress. The foulant build-up is given by the following relationship:

$$\frac{dM_d}{dt} = J_R c_b - \beta_T M_d \quad (50)$$

where β_T is an empirical turbulence burst factor. The final flux relationship is of the form

$$\frac{J_f}{J_i} = f(c_b, u_b, t, k, \beta_T, \alpha_D) \quad (51)$$

Equation 51 was successful in predicting final fluxes in the colloidal fouling of RO membranes but predicted initial flux decline was not in good agreement with experimental data.

The model by Howell and Velicangil [1980] is more useful for explaining protein adsorption; the permeate flux decline is divided into three stages: the initial polarization period, a protein adsorption step, and finally the polymerization of the protein in the gel layer. The thickness of the deposit is related to the surface concentration by a second-order rate expression with the rate constant being determined empirically.

In the kinetic growth model for a porous tube [Probstein, 1981; Cohen, 1986], the rate of fouling is assumed to be a first-order reaction. The pressure drop across the membrane is assumed to be due to hydrodynamic resistance characterized by the Kozeny-Carman relation. In addition, foulant transport is assumed convection controlled with no transport away from the membrane. The authors theorized that a reaction layer existed directly adjacent to the fouling layer to which the solute was transported due to solvent permeation. Once the solute entered the reaction layer, a portion of the incoming solute formed a gel at a the rate is characterized by a constant K_d . An unsteady state solute mass balance was written as:

$$\delta_r \frac{\partial C^*}{\partial t} = C_0 V_0 - K_d C^* \quad (52)$$

where δ_r is the thickness of the reaction layer, C_0 is the dimensionless foulant concentration, V_0 is the permeation velocity, and C^* is the average foulant concentration in the reaction layer. The first term on the right hand side of Equation 52 describes the transport of the solute into the reaction layer, while the second term represents the rate of deposition on the membrane surface from the reaction layer. The permeate flux decline is calculated after integrating Equation 52 with the initial condition $C^* = C_0$. The model was in good agreement when compared with experimental data collected on stabilized iron oxide colloids [Cohen, 1986].

Finally, precipitation models are used to describe inorganic fouling; inorganic compounds such as calcium sulfate and calcium carbonate precipitate when their solubility limit is exceeded. This is in contrast to the models involving colloidal and macromolecular solutes that form gels at high concentrations. Precipitation models are

governed strongly by solution chemistry including pH and ionic strength as solubility of inorganic species is strongly dependent on these factors. Important models include the surface blockage model developed by Gilron and Hassan [1987], and the Fountoukidis model [1989] for explaining calcium sulfate fouling in RO; and the Jackson and Landolt model developed to describe iron oxide fouling.

It is emphasized that the models included this and the previous section on CP and fouling need to be extended for commercial systems such as hollow-fiber and spiral wound modules, by combining them with the overall fluid and mass balances on the feed and the permeate channels; this would depend mainly on the geometry of the membrane module. The existing modeling work on CP in such membrane systems is reviewed in section 2.6 as a preamble to the transient model developed in this study; the review is not extended to fouling analysis as it is not addressed in this work.

2.4 Minimizing CP and Fouling

Methods that are used for minimizing CP aim at increasing the back transport of the solute away from the membrane surface into the bulk solution. The most common way of increasing back transport is to construct a module that increases cross-flow; the flow in such a case will be either turbulent or high-shear stress laminar [Matthiason, 1980]. Tubular modules allow for membrane separation under turbulent conditions but at the expense of permeate recovery; spiral wound modules generally operate under laminar flow but solute mixing is enhanced by placing spacers in the feed channel. Spacers and mixers are also used in tubular and plate-and-frame units to increase mixing.

Experiments show that presence of mixers and spacers generally increase permeate flux for the same feed concentration and cross-flow velocity [Blatt, 1970].

Fouling, however is an irreversible process and therefore control strategies aim at minimizing and/or delaying the onset of the process. Methods that are used to control fouling fall into three broad categories [Wakeman, 1986].

1. Tailor or pretreat membranes
2. Modify or pretreat the feed solution
3. Adjustment of operating conditions.

Pretreatment processes that reduce potential fouling include coating the membrane with thin carbon layers and enzymes, and reacting with hydrophilic surfactants [Wakeman, 1986]. Pretreatment for feed solution includes both physical and chemical treatment such as filtration, coagulation, sedimentation and disinfection. Anti-foulants and anti-scalants are also generally added to reduce fouling; these compounds generally stabilize the solutes in solution and prevent gel formation, precipitation and scaling. The feed solutions are also characterized in terms of parameters such as the silt density index (SDI), the fouling index (FI) and the modified fouling index (MFI) to describe fouling potential [Potts, 1981; Schippers, 1980]. The most useful operating parameter for fouling control is the cross-flow velocity; increasing the cross-flow velocity decreases CP and therefore fouling by increasing diffusive mass transfer and lateral migration. Other control strategies include use of pulsating flow and back-flushing [Matthiason, 1980].

2.5 Modeling CP in Commercial Membrane Modules

In order to predict the effects of CP in full-scale membrane facilities, an appropriate membrane CP model must be used in conjunction with the equations of mass transport, continuity and flow balance along with appropriate boundary conditions. In order to obtain an accurate mathematical CP model for any of the four previously discusses membrane modules, it is necessary to start with the equations of motion, continuity, mass and energy transfer. For a generalized membrane system, these equations are [Kleinstreuer, 1983]:

$$\text{Continuity: } \frac{\partial \rho}{\partial t} + \nabla \cdot \rho \bar{v} = 0 \quad (53)$$

$$\text{Motion: } \frac{\partial}{\partial t} \rho \bar{v} + \nabla \cdot \rho \bar{v} \bar{v} = - \nabla P - \nabla \cdot \bar{\bar{\tau}} + \Sigma \bar{f} \quad (54)$$

$$\text{Mass transport: } \frac{\partial c}{\partial t} = - \nabla \cdot \bar{J}_c + S_c \quad (55)$$

$$\text{Energy transport: } \frac{\partial}{\partial t} \rho E + \nabla \cdot \rho E \bar{v} = - \nabla \cdot \bar{q}_H - \bar{\bar{\pi}} : \nabla \bar{v} \quad (56)$$

where $\bar{\bar{\tau}}$ is the stress tensor, \bar{J}_c and \bar{q}_H are the mass and heat flux vectors, E is the internal energy, \bar{S}_c is the solute source flux, and \bar{v} is the velocity vector. \bar{J}_c is generally written as [Song, 1995]

$$\bar{J}_c = -\bar{D}_s \cdot \nabla c + \bar{v}c + \frac{\bar{D}_s \cdot \bar{F}}{k_b T} c \quad (57)$$

where \bar{D}_s is the diffusion tensor, \bar{F} is the force vector and k_b is the Boltzmann constant.

Each of the terms in the last equation represent the contributions of solute diffusion, fluid motion and external forces. In most RO systems the solute comprises of dissolved solids present in water, and therefore the last term in the solute flux equation is neglected; for colloidal suspensions, this term cannot be ignored and the external force vector is generally expanded to include colloidal forces such as van der Waal and electric double layer (EDL) interactions [Song, 1995]. In addition, most membrane systems deal with isothermal flow and therefore the energy transport equation is also frequently ignored. The solute flux equation is substituted in the mass transport equation to yield a mass transport equation of the form:

$$\frac{\partial c}{\partial t} = \nabla \cdot (\bar{D}_s \cdot \nabla c) - \nabla \cdot (\bar{v}c) \quad (57)$$

that is commonly referred to as the convective-diffusion equation (CDE). In this section, existing models that attempt to solve the CDE in conjunction with Equations 53 and 54 for different membranes and membrane geometries are reviewed.

2.5.1 Momentum transport and velocity profiles

For isothermal systems represented by constant fluid and solute properties, Equations 52 and 52 reduce to the following in cartesian coordinates[Belfort, 1984]:

$$\text{Continuity: } \frac{\partial u}{\partial x} + \frac{\partial v}{\partial y} = 0 \quad (59)$$

$$\text{x-momentum: } \frac{\partial u}{\partial t} + u \frac{\partial u}{\partial x} + v \frac{\partial u}{\partial y} = -\frac{1}{\rho} \frac{\partial p}{\partial x} + \nu \left(\frac{\partial^2 u}{\partial x^2} + \frac{\partial^2 u}{\partial y^2} \right) \quad (60)$$

$$\text{y-momentum: } \frac{\partial v}{\partial t} + u \frac{\partial v}{\partial x} + v \frac{\partial v}{\partial y} = -\frac{1}{\rho} \frac{\partial p}{\partial y} + \nu \left(\frac{\partial^2 v}{\partial x^2} + \frac{\partial^2 v}{\partial y^2} \right) \quad (61)$$

where p is the pressure, ρ is the density and ν is the kinematic viscosity.

Channel with Two Porous Walls

Berman [1958] analyzed the above set of equations for steady state laminar flow in a channel with two porous walls as shown in Figure 2.6. The following boundary conditions

including constant permeation velocity were assumed to hold:

$$u(x, \lambda = \pm 1) = 0 \quad (62a)$$

$$\left(\frac{\partial u}{\partial \lambda} \right)_{\lambda=0} = 0 \quad (62b)$$

$$v(x, \lambda = 0) = 0 \quad (62c)$$

$$v(x, \lambda = \pm 1) = v_w = \text{constant} \quad (62d)$$

where λ is dimensionless variable $\lambda = y/H$ with $2H$ being the channel thickness; a perturbation solution was used to obtain the velocity profiles in the axial (x-) and transverse (y-) directions as

$$u(x, \lambda) = \frac{3}{2} u_{\text{avg}}(x) (1 - \lambda^2) \left[1 - \frac{\text{Re}_y}{420} (2 - 7\lambda^2 - 7\lambda^4) \right] \quad (63)$$

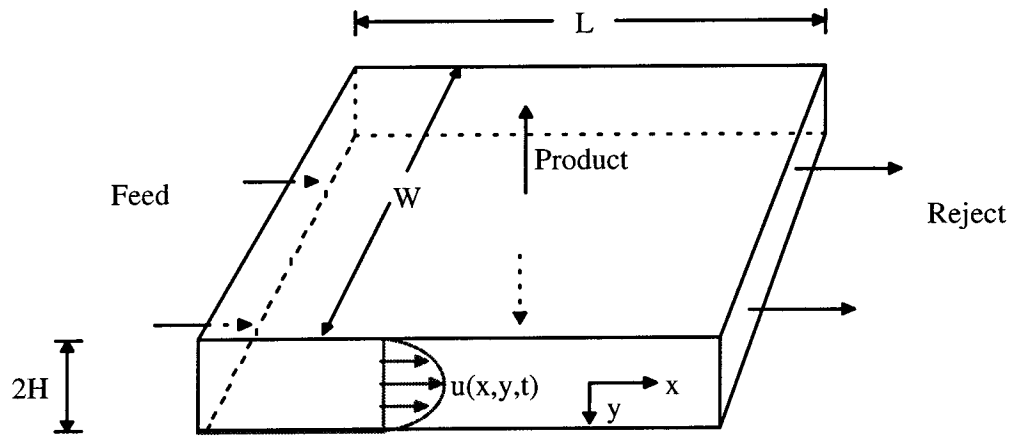
$$\frac{v(\lambda)}{v_w} = \frac{\lambda}{2} (3 - \lambda^2) - \frac{\text{Re}_y}{280} \lambda (2 - 3\lambda^2 + \lambda^6) \quad (64)$$

where

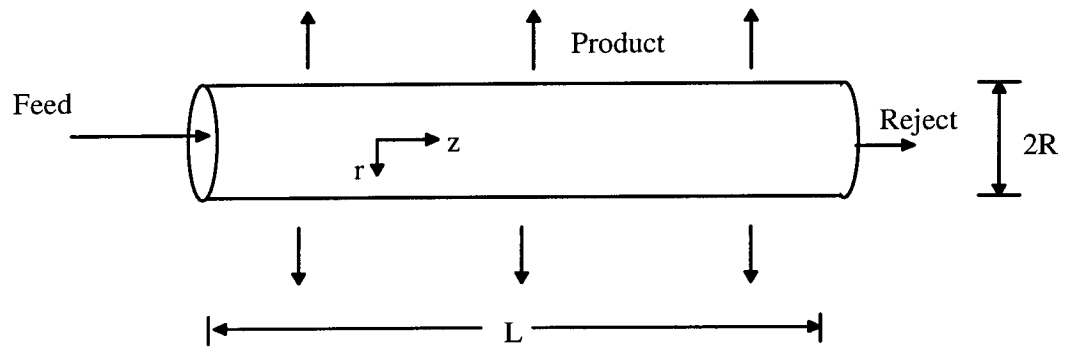
$$u_{\text{avg}}(x) = u_{\text{avg}}(0) - \frac{v_w x}{H} \quad (65)$$

and Re_y is the permeation Reynolds number defined as $\text{Re}_y = v_w h / \nu$. Equation 63 describes a parabolic profile for the axial velocity if permeation effects are neglected; this is in accordance with the standard solution for laminar flow in a channel with solid walls [Bird, 1965]. For non-uniform permeation velocity which is often the case in membrane systems, it is assumed that the form of the velocity profiles remains unchanged; however, the average axial velocity is obtained from an integrated mass balance as:

$$u_{\text{avg}}(x) = u_{\text{avg}}(0) - \frac{1}{H} \int_0^x v_w(x) dx \quad (66)$$



(a)



(b)

Figure 2.6: Flow in membrane modules. (a) Laminar flow in channels with two porous walls, and (b) radial flow in porous pipes.

The preceding equations are limited to systems where no-slip condition exists at the membrane surface i.e., $u(\lambda=1) = 0$. Singh and Laurence [1979] extended the analysis to include slip at the membrane surface; they showed that the presence of slip flattened the parabolic profile of the axial velocity.

Channel with One Porous Wall

Kleinstrauer [1983] performed a similar analysis but for channel flow with one solid wall and one porous wall; the velocity profiles in the axial and transverse directions were

$$u(x, \lambda) = u_{\text{avg}}(x) \left[\frac{3}{3}(1 - \lambda^2) - \frac{\text{Re}_y}{560} (-7\lambda^6 - 140\lambda^3 + 9\lambda^2 + 140\lambda - 2) \right] \quad (67)$$

$$\frac{v(\lambda)}{v_w} = \frac{1}{4}(\lambda^3 - 3\lambda - 2) - \frac{\text{Re}_y}{1120} (-\lambda^7 - 35\lambda^4 + 3\lambda^3 + 70\lambda^2 - 2\lambda - 35) \quad (68)$$

where the average axial velocity $u_{\text{avg}}(x)$ was defined as

$$u_{\text{avg}}(x) = u_{\text{avg}}(0) - \frac{1}{2H} \int_0^x v_w(x) dx \quad (69)$$

Porous Pipe

Similar analysis on steady state laminar flow in a porous pipe of radius r_m with constant permeation velocity is also available (Figure 2.6) [Yuan, 1956]; the equations of continuity and flow balance are

$$\text{Continuity: } \frac{\partial(ru)}{\partial z} + \frac{\partial(rv)}{\partial r} = 0 \quad (70)$$

$$\text{z-momentum: } u \frac{\partial u}{\partial z} + v \frac{\partial u}{\partial r} = -\frac{1}{\rho} \frac{\partial p}{\partial z} + v \left(\frac{\partial^2 u}{\partial r^2} + \frac{\partial^2 u}{\partial z^2} + \frac{1}{r} \frac{\partial u}{\partial r} \right) \quad (71)$$

$$\text{r-momentum: } u \frac{\partial v}{\partial z} + v \frac{\partial v}{\partial r} = -\frac{1}{\rho} \frac{\partial p}{\partial r} + v \left(\frac{\partial^2 v}{\partial z^2} + \frac{\partial^2 v}{\partial r^2} + \frac{1}{r} \frac{\partial v}{\partial r} - \frac{v}{r^2} \right) \quad (72)$$

The velocity profiles in the axial and radial directions for small values of permeation velocity and tube radius have the following form provided permeation distortions are neglected [Ma, 1985]:

$$u(r, z) = 2u_{\text{avg}}(z) \left(1 - 2 \left(\frac{r}{r_m} \right)^2 \right) \quad (73)$$

$$v(r) = v_w \left(2 \frac{r}{r_m} - \left(\frac{r}{r_m} \right)^3 \right) \quad (74)$$

where the average axial velocity $u_{\text{avg}}(z)$ at a downstream position z is given by

$$u_{\text{avg}}(z) = u_{\text{avg}}(0) - 2 \frac{zV_w}{r_m} \quad (75)$$

Channel with Feed Spacer and Two Porous Walls

For flow in a channel with two porous walls and spacers in between, the transverse velocity profile is assumed to remain the same while the axial velocity profile is modified to include lateral fluid displacement effects caused by the spacer [Miyoshi, 1982]; the profile has the following form

$$u(x, y) = \frac{dP}{dx} \frac{h^2}{\eta m^2} \left(1 - \frac{v_w x}{u_0 h}\right) \left\{ (m+1) \ln \left[m \left(1 - \frac{y}{h}\right) + 1 \right] - m \left(1 - \frac{y}{h}\right) \right\} \quad (76)$$

where m is an eddy constant associated with the spacer [$m = (\text{eddy viscosity})h/\nu$], and the term $(1 - v_w x/u_0 h)$ represents permeation loss. The following expression is used to obtain the eddy constant [Miyoshi, 1982]:

$$m = 2.1 \times 10^5 \left[n_s (t_s - d_s) \right]^{2.4} \left(\frac{1 - \epsilon}{\epsilon^3} \right)^{0.8} \quad (77)$$

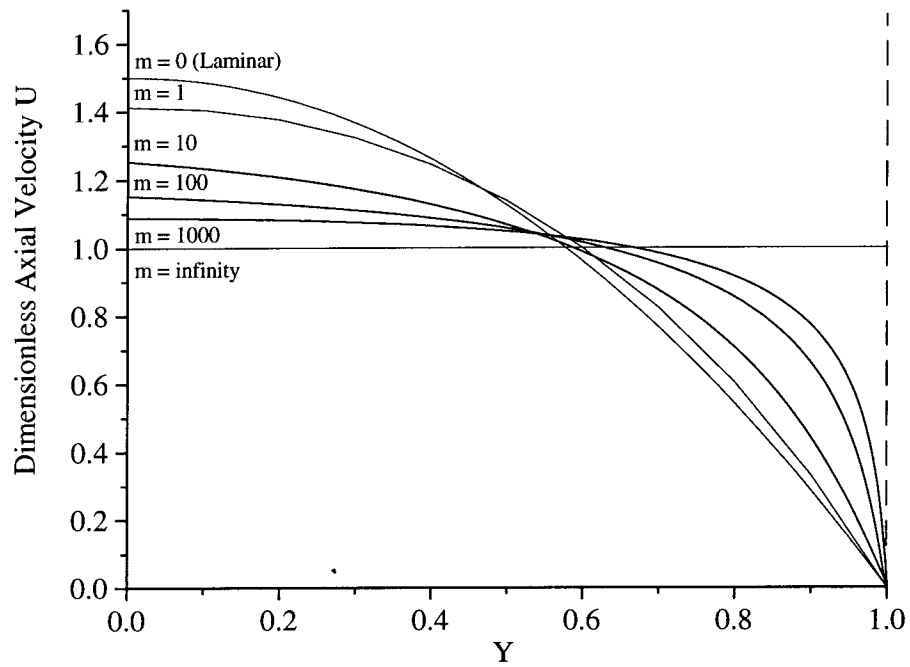


Figure 2.7: Effect of the eddy constant m on axial velocity in a spiral wound membrane [Miyoshi, 1982].

where n_s is the number of spacers, d_s is the diameter of the fiber, t_s is the spacer thickness, and ϵ is the spacer void fraction. A high value of m represents high level of mixing in the channel; such a parameter is very useful in fabricating feed spacers for membranes. Figure 2.7 illustrates the effect of m on the axial velocity profile; high values of m lead to flatter profiles indicating high level of mixing and turbulence.

The average initial velocity u_0 is calculated from

$$u_0 = \frac{dP}{dx} \frac{h^2}{\eta m^3} [(m+1)^2 \ln(m+1) - 1.5m^2 - m] \quad (78)$$

2.5.2 Pressure Profiles

For rectangular channel with width (W) much larger than the thickness ($2H$), and in the absence of the permeation, the pressure drop is described by [Bouchard, 1994]:

$$P_0 - P(x) = \frac{3\bar{u}_0 \eta x}{H^2} \quad (79)$$

For channel with porous walls, modifications of the above profile are available that include permeation effects [Berman, 1958; Kleinstrauer, 1983]; however, the permeation

velocity in membrane systems is smaller than the axial velocity, and the effects are negligible. Similar pressure profiles are also available for tubular flow [Ma, 1985].

2.5.3 Mass Transport

Two approaches have been used in solving the mass balance equation: (1) the non-conservative approach that involves substituting the continuity equation in the mass balance equation; and (2) the conservative approach where the two equations are not combined [Brian, 1965; Roache, 1982]. For channel systems, the equations are obtained by expanding the terms in Equation 57 as

$$\frac{\partial c}{\partial t} = D_s \frac{\partial^2 c}{\partial y^2} - u \frac{\partial c}{\partial x} - v \frac{\partial c}{\partial y} \quad (\text{Non-conservative}) \quad (80)$$

$$\frac{\partial c}{\partial t} = D_s \frac{\partial^2 c}{\partial y^2} - \frac{\partial u \cdot c}{\partial x} - \frac{\partial v \cdot c}{\partial y} \quad (\text{Conservative}) \quad (81)$$

However, for tubular and hollow-fiber configurations, the mass balance equation is available in non-conservative form only as [Ma, 1985]:

$$\frac{\partial c}{\partial t} + u \frac{\partial c}{\partial z} + \left(v - \frac{D_s}{r} \right) \frac{\partial c}{\partial r} = D_s \frac{\partial^2 c}{\partial r^2} \quad (82)$$

2.5.4 Solution techniques

Methods for solving the CDE (Equation 57) are generally classified as: (1) asymptotic and (2) numerical. Asymptotic methods and perturbation solutions are available but only for simplified systems that assume constant permeation velocity, low solvent recovery and constant fluid properties [Sherwood, 1964; Kozinski, 1970]. Several numerical techniques are available that tackle Equations 80-82 in conjunction with the solutions of the flow balance and continuity equations; these methods are preferred because of the complexity of the mass balance equation. Some of the important numerical methods are reviewed in this section. It has to be noted that most of these studies are limited to steady-state analysis except the model of Ma and co-workers [1985]. Finite difference (FD) method is the method of choice, because it is conceptually elegant and easy to implement; models that use other numerical techniques such as the integral method (MIR) and the finite element method (FEM) are also available [Belfort, 1984; Bhattacharya, 1990].

Non-conservative models

Singh [1979] applied a general implicit FD scheme for steady state flow in a channel with two porous walls. The mass balance equation (Equation 79) was represented as a finite difference equation and solved in a numerical block; two adjacent slices in the transverse direction were used in developing the solution. The solution was assumed to be known for the slice i , and this was used in computing the values on the unknown slice $i+1$. The finite difference equation that represented mass balance for the node $(i+1, j)$ consisted of one first-order correct analog in the axial direction (I term in

Equation 83), and two second order correct analogs in the transverse direction (II and III terms in Equation 83):

$$\begin{aligned}
 u_{i+1,j} \left[\frac{c_{i+1,j} - c_{i,j}}{\Delta x} \right] + v_{i+1,j} \left[\frac{c_{i+1,j+1} - c_{i+1,j-1}}{2\Delta y} \right] \\
 = D_s \left[\frac{c_{i+1,j+1} - 2c_{i+1,j} + c_{i+1,j-1}}{\Delta y^2} \right]
 \end{aligned} \tag{83}$$

Similar equations were written for all the nodes on the unknown slice. This resulted in J equations for a slice with J+2 unknowns; however, the boundary conditions for j=1 and j=J were used in eliminating the two unknowns. The boundary conditions that were used in that study are given below:

$$c(0,y) = c_0 \tag{84a}$$

$$\left(\frac{\partial c}{\partial y} \right)_{y=0} = 0 \tag{84b}$$

$$v_p(x) \cdot c_m(x) = D_s \cdot \left(\frac{\partial c}{\partial y} \right)_{y=H} \tag{84c}$$

The J equations were arranged in a tri-diagonal matrix form, and solved using the Thomas algorithm. The procedure was repeated for all values of k; the boundary condition at x=0 was used to start the entire calculation procedure. In this model, the axial velocity profile included for slip at the membrane surface; the form of expression is

similar to the standard parabolic profile but at the membrane surface, the velocity assumes the value

$$u(x,H) = \phi H \frac{\partial u}{\partial y} \quad (85)$$

where ϕ is the slip coefficient. The above numerical procedure was used to simulate steady state fluxes for various feed conditions and different slip coefficients.

Similar implicit numerical solutions are also available for channel flow with imperfect walls [Lebrun, 1989], and one porous wall [Kleintrauer, 1983]; for the case of imperfect flow, the y-boundary condition near the membrane surface is modified to include the permeate contribution to mass flux. A dynamic FD numerical model was developed by Ma and co-workers [1985] to explain CP in low pressure hollow-fiber UF membranes; this included a modified Crank-Nicholson analog in the radial direction, and modified center-difference analogs in axial direction and time. There was good agreement between experimental and predicted flux values. Bhattacharya [1990] developed a steady state model employing Galerkin finite element technique for predicting CP in spiral-wound RO membranes; the model was verified experimentally with various feed solutions including water-NaCl, water-sucrose, and a Bingham fluid (Tomato juice).

Conservative Models

For the conservative mass balance equation, Brian and co-workers [Brian, 1965] used a two step Crank-Nicholson FD method; in this model, the velocity profiles were

simplified versions of the Berman expressions where distortions from permeation were neglected (Equations 63 and 64). The solution procedure was similar to the non-conservative approach; however, three corresponding nodes were chosen in the known and unknown slices of the solution block, and solved using tri-diagonal Thomas algorithm. The entire procedure is more accurate because of the lower magnitude of the truncation error. In a recent comparative study by Bouchard and co-workers [1994], it was shown that when the FD increments (Δx and Δy) were small, both the conservative and non-conservative approaches gave accurate solutions; and when the increments were large, the conservative approach gave more meaningful results.

2.5.5 Limitations of Existing Work

A major limitation of the previously reviewed CP models (except the model of Ma and co-workers) is the assumption of the steady-state condition; the absence of time dependent term in the convective diffusion equation (CDE) limits these models from being extended for including fouling and long term degradation. In real systems however, the steady state condition rarely exists as several complex phenomena simultaneously take place; for example, in wastewater reclamation, the initial steady state from CP is quickly attained but permeate flux decline continues over several hours or even days.

A recent pilot study on wastewater reclamation conducted in Lake Arrowhead, CA demonstrated these problems during nanofiltration (NF) and ultrafiltration (UF) treatment of tertiary treated municipal effluent; the main objective of the project was to demonstrate the feasibility of reclaiming municipal wastewater effluent for indirect potable reuse after extensive treatment and subsequent storage (See Appendix I for the

overview of the project and plant performance). Spiral wound thin-film composite UF and NF membranes were used as a pretreatment step for subsequent RO treatment and removal of inorganic solids and trace organics. The UF/NF processes operated at an initial permeate recovery of approximately 75% while the RO membranes operated at approximately 90% permeate recovery. The feed to the UF/NF units was tertiary treated municipal effluent; processes that were used in treatment included denitrification to remove nitrogen, alum clarification and rapid sand filtration to remove phosphorus and turbidity, ozonation to disinfect bacteria and pathogens, and granular activated carbon to remove organic carbon.

Figure 2.8 shows the permeate flux decline of the NF membranes over a period of three months of continuous operation. The decline was considerable (40-70%) and manifested in two ways: a reversible decline that was recovered through weekly cleaning and an irreversible decline that eventually forced the membranes to be replaced. The cleaning regimen included low pH (4-4.5) cleaning to remove scaling, followed by moderately high temperature (100 F) - high pH (11-11.5) surfactant cleaning to remove organic gels and bacterial slime; the total cleaning time was approximately one hour. In this study, the high pH cleaning recovered a major portion of flux decline confirming that organic gels and bacterial slime were the important factors, and that the formation of these layers generally takes from several hours to days.

A transient flux decline of the kind described above cannot be represented by a steady state model; thus, a major objective in this study is to develop a global model to predict transient behavior but that is not limited by a single membrane flux model such as the osmotic model. The model will be developed so that other phenomena such as gel

formation, cake formation and colloidal deposition that are differently described and manifest over longer time periods could also be incorporated.

Another limitation of existing work is that commercial systems such as spiral-wound and hollow-fiber systems have not been comprehensively analyzed; the model of Ma and co-workers [1985] describes permeate flux behavior in hollow-fiber units but is limited to low permeate recovery. The model of Bhattacharya and co-workers describes flux behavior in spiral-wound units but is limited to steady-state analysis and was verified only for low permeate recovery. Recently Marinas and Urama [1996] developed a CP model for a spiral-wound RO unit applying thin-film theory, and assuming the unit behaves as a continuously stirred tank reactor; however, the analysis was limited to steady-state systems and very low permeate recovery. All these limitations are also addressed in this study.

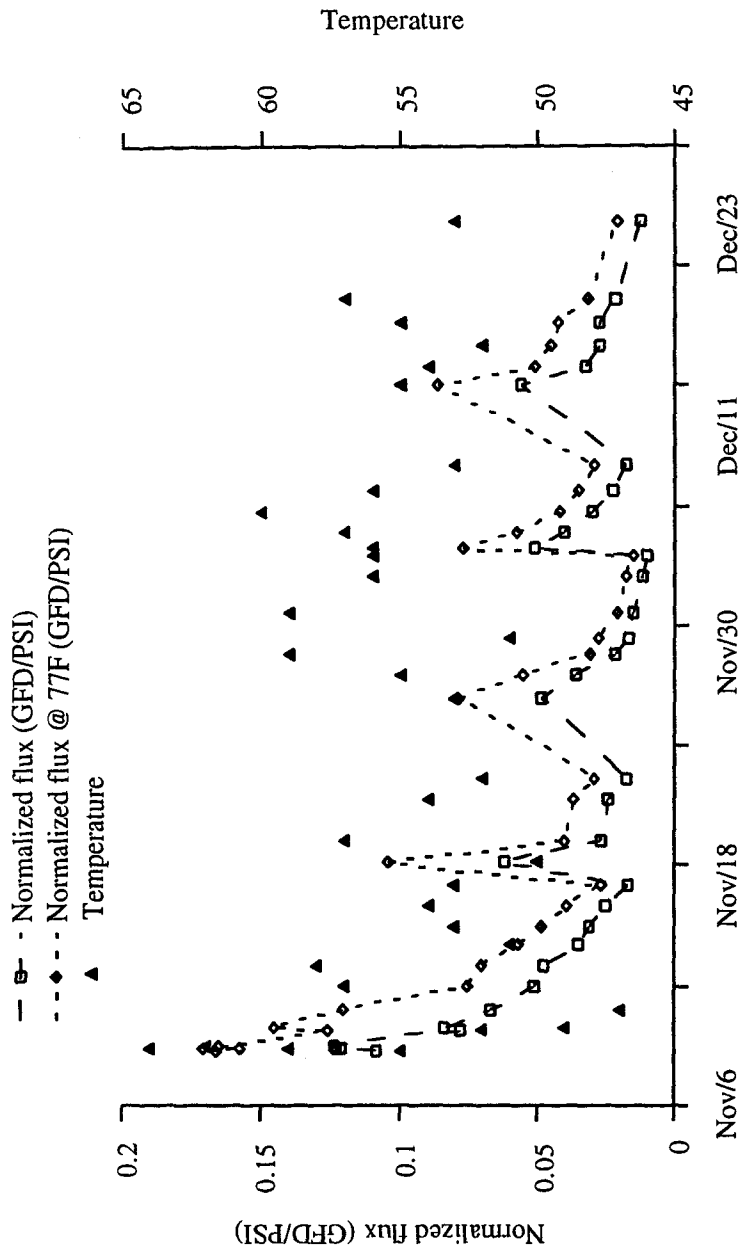


Figure 2.8: Permeate flux decline during NF separation of wastewater effluent for a 12 week test period in Lake Arrowhead, CA with weekly chemical cleaning: normalized flux (GFD/psi) at ambient temperature and at 77 °F depicted over time.

CHAPTER 3

MODEL DEVELOPMENT AND EXPERIMENTAL METHODS

3.1 Model Development

3.1.1 Mathematical Formulation

The main objective of the model is to predict permeate flux behavior in a spiral wound membrane by solving the convective diffusion equation (CDE) for mass balance (Equation 57) in conjunction with the flow balance and continuity equations. The main assumptions and basic features of the model are:

1. The feed solution consists of one solute (NaCl), component 1, and a solvent (water), component 2.
2. The spiral wound membrane is approximated by a thin horizontal rectangular channel of length L and width W bounded by two porous walls (Figure 2.6a); spiral effects are ignored for computing purposes. The thickness of the feed spacer is equal to the channel thickness ($2H$).
3. The flow in spiral wound membranes is laminar at high permeate recoveries; in experiments conducted to verify this model, the cross-flow Reynolds Number Re_x was below 200. Accordingly, the flow in the channel is assumed to be laminar and two-dimensional.

4. Existing fluid flow profiles such as the Berman profile (Equations 62-65) or Miyoshi profile (Equations 75-77) are included for representing channel flow with and without feed spacers, respectively. In addition, completely mixed flow is also included to study the effects of mixing on CP; this will be accomplished by assuming that the cross-flow velocity profile is completely flat (i.e., the motion is plug flow).
5. The non-conservative form of the mass balance equation is used in generating CP information and permeate flux behavior. The boundary conditions are defined as in the case of unstirred batch RO, using the thin-film model.
6. The model assumes that the membrane is permeable to solute (Rejection R is less than or equal to 1).
7. Isothermal conditions exist.
8. The diffusivity of salt is assumed to be constant.
9. The mass density and viscosity is independent of the solute concentration.
10. Finally to simplify computing complexity in initial start-up period, it is assumed that fluid flow is fully developed and at steady state at the start of each run; furthermore, it is assumed that the profiles will not distort under permeation and CP effects.

The extended form of the following mass balance CDE for the conditions described above is:

$$\frac{\partial c}{\partial t} = D_s \cdot \frac{\partial^2 c}{\partial y^2} - v(x, y, t) \cdot \frac{\partial c}{\partial y} - u(x, y, t) \cdot \frac{\partial c}{\partial x} \quad (86)$$

where c is the concentration of the salt on the feed side and is a function of spatial coordinates x and y and time t , u and v are the horizontal and vertical components of fluid velocity, and D_s is the solute diffusivity. The mass balance CDE is a second order partial

differential equation that requires one initial condition, one boundary condition in the axial direction and two boundary conditions in the transverse direction.

The appropriate initial and boundary conditions are

$$c = 0 \quad @ \quad t = 0 \quad (x > 0, y \geq 0) \quad (87a)$$

$$c = c_0 \quad @ \quad x = 0 \quad (y \geq 0, t \geq 0) \quad (87b)$$

$$\frac{\partial c}{\partial y} = 0 \quad @ \quad y = 0 \quad (x \geq 0, t \geq 0) \quad (87c)$$

$$D_s \cdot \frac{\partial c}{\partial y} = v \cdot c - v_p \cdot c_p \quad @ \quad y = H \quad (x \geq 0, t \geq 0) \quad (87d)$$

The initial condition (Equation 87a) describes pure solvent permeation across the membrane at time $t = 0$; the axial boundary condition (Equation 87b) describes the start of an individual run for a feed solution c_0 . The first boundary condition in the transverse direction describes symmetry at the lateral center-line; the numerical solution is generated for one-half of the channel and then duplicated for the other half. The second boundary condition (Equation 87d) describes solute mass flux across the membrane: on the feed side, the two competing flux terms are the convective mass flux towards the membrane surface and the diffusive mass flux away from the membrane surface; on the permeate

side, the net solute flux is the solute concentration in the permeate multiplied by the permeate fluid flux. The last equation describes CP effect at the membrane surface.

To aid in the development of the model, the following dimensionless terms were defined, and the CDE was scaled accordingly:

$$C = \frac{c}{c_0} \quad (88)$$

$$U = \frac{u}{u_0} \quad (89)$$

$$V = \frac{v \cdot L}{u_0 \cdot H} \quad (90)$$

$$X = \frac{x}{L} \quad (91)$$

$$Y = \frac{y}{H} \quad (92)$$

$$T = \frac{t \cdot u_0}{L} \quad (93)$$

$$D = \frac{D_s \cdot L}{u_0 \cdot H^2} \quad (94)$$

After substituting the above terms, the CDE was converted into the following dimensionless equation:

$$\frac{\partial C}{\partial T} = D \cdot \frac{\partial^2 C}{\partial Y^2} - V \cdot \frac{\partial C}{\partial Y} - U \cdot \frac{\partial C}{\partial X} \quad (95)$$

subject to the following initial and boundary conditions

$$C = 0 \quad @ \quad T = 0 \quad (96a)$$

$$C = 1 \quad @ \quad X = 0 \quad (96b)$$

$$\frac{\partial C}{\partial Y} = 0 \quad @ \quad Y = 0 \quad (96c)$$

$$D \cdot \frac{\partial C}{\partial Y} = V \cdot C - V_p \cdot C_p \quad @ \quad Y = 1 \quad (96d)$$

In Equation 96d, V_p and C_p are non-dimensional solvent flux and solute concentration on the permeate side of the module. The following fluid flow profiles in their dimensionless form were employed for substitution in Equation 95:

Axial Direction (U): Three different profiles were used depending on the axial flow pattern (laminar, turbulent and spiral wound flow)

Laminar Flow:

$$U(X, Y, T) = U_{avg}(X, T) \cdot \frac{3}{2}(1 - Y^2) \quad (97)$$

The above equation is a dimensionless version of the Berman solution (Equation 62) where the distortion terms from permeation are neglected.

Completely Mixed Flow:

$$U(X, Y, T) = U_{\text{avg}}(X, T) \quad (98)$$

The above equation describes maximum mixing and plug flow conditions.

Spiral Wound Flow:

$$U(X, Y) = U_{\text{avg}}(X, T) \cdot \frac{\{(m+1)\ln[m(1-Y)+1] - m(1-Y)\}}{(m+1)^2 \ln(m+1) - 1.5m^2 - m} \quad (99)$$

The average dimensionless axial velocity is defined as:

$$U_{\text{avg}}(X, T) = 1 - \int_0^X V_w(X, T) \cdot dX \quad (100)$$

Transverse Flow (V): The same profile was assumed to hold for all three flow categories (laminar, completely mixed and spiral wound).

$$V(X, Y, T) = V_w(X, T) \cdot \frac{Y}{2}(3 - Y^2) \quad (101)$$

The preceding axial velocity equations (97-99) assume constant permeation velocity; however, the permeation velocity for moderate to high permeate recoveries is a function

of the axial position and time. For model calculations, the permeation velocity was calculated at each time and axial position and the average axial velocity was computed from an incremental mass balance as shown in Equation 100.

The following pressure profile in the axial direction was employed:

$$P(X) = P(0) - \Delta P_{ax} \cdot X \quad (102)$$

This equation was adopted as pressure drop in spiral wound modules was greater than straight channels (Equation 79) because of the presence of feed spacers. In this study, the maximum axial pressure drop (ΔP_{ax}) was observed to be 10% of the inlet pressure in all experiments; this value was substituted in Equation 102 to compute $P(X)$.

Furthermore, a membrane permeation flux equation based on the osmotic model was used to obtain membrane permeation velocity:

$$V_w(X, T) = A \cdot (\Delta P(X, T) - \Delta \Pi(X, T)) \quad (103)$$

where A is the membrane permeability, and ΔP and $\Delta \Pi$ are the applied pressure and the induced osmotic back pressure. This equation replaces the constant fluid flux boundary condition (Equation 62d) after each initial transverse iteration.

3.1.2 Determination of Experimental Parameters

The key parameters in the solution of Equation 88 are the membrane permeability A , the solute diffusivity D_s and the osmotic pressure constant K_{osm} . The membrane permeability was evaluated from select pure water permeation experiments on the membrane at different operating pressures and ambient temperatures. Equation 96 was used to relate permeation flux in gallons per day per square feet of membrane area (GFD) with the average operating pressure in psi for two different feed flow rates, and subsequently compute the proportionality constant A defined as the permeability coefficient (Figure 3.1 and 3.2); the second term on the right hand side of Equation 103 is neglected because of the absence of any solute and corresponding osmotic pressure. The computed permeability coefficient values are plotted versus ambient temperature as shown in Figure 3.3.

NaCl-water system was used to verify model predictions. According to Sourirajan [1970], there is negligible variation in the value of solute diffusivity D_s for the range of NaCl concentrations from 0 to 1.6 M; hence, a value of $1.61 \times 10^{-5} \text{ cm}^2/\text{sec}$ that represents molecular diffusivity was used in all model runs. Sourirajan [1970] also documented the effect of NaCl concentration on osmotic pressure at different ambient temperatures; the osmotic pressures were plotted versus NaCl concentrations in the range of 0.1 M to 1.0 M at different temperatures. A linear relationship of the form described by Equation 104 was assumed to hold (Figure 3.4), and the corresponding osmotic pressure constants K_{osm} were computed and plotted (Figure 3.5).

$$\Pi = K_{osm} \cdot c \quad (104)$$

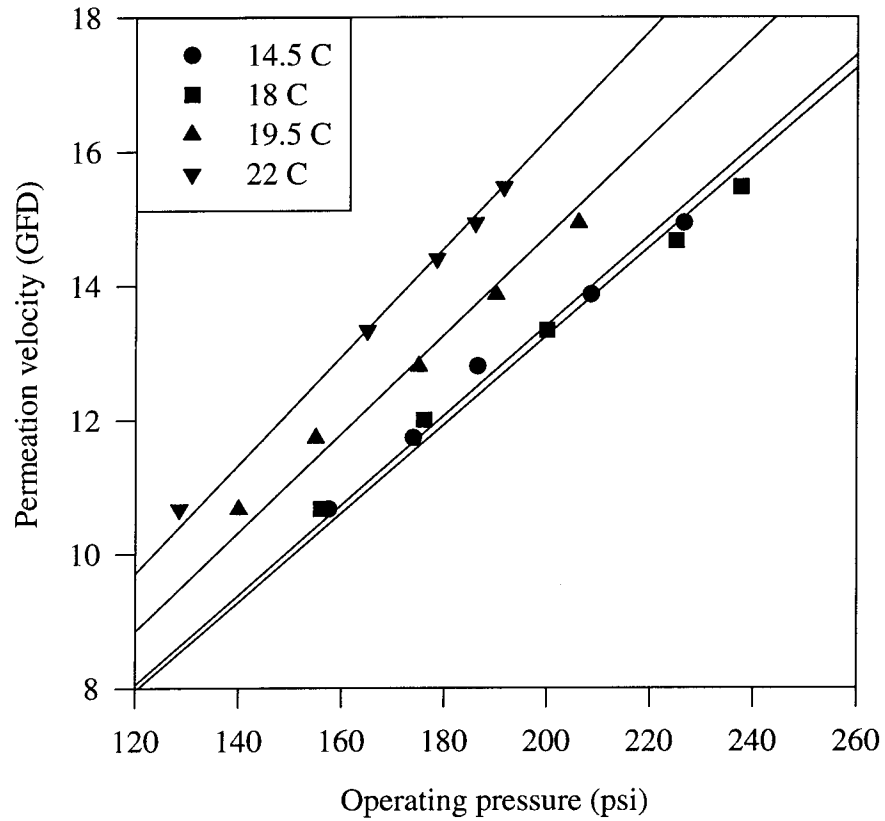


Figure 3.1: Pure water permeability tests conducted on a spiral wound RO unit at various temperatures and constant feed flow of 3.0 gallons per minute (GPM). Permeation velocity in gallons per day per square foot of membrane area (GFD) versus operating pressure in psi; permeability coefficient A is defined by the slope of each line.

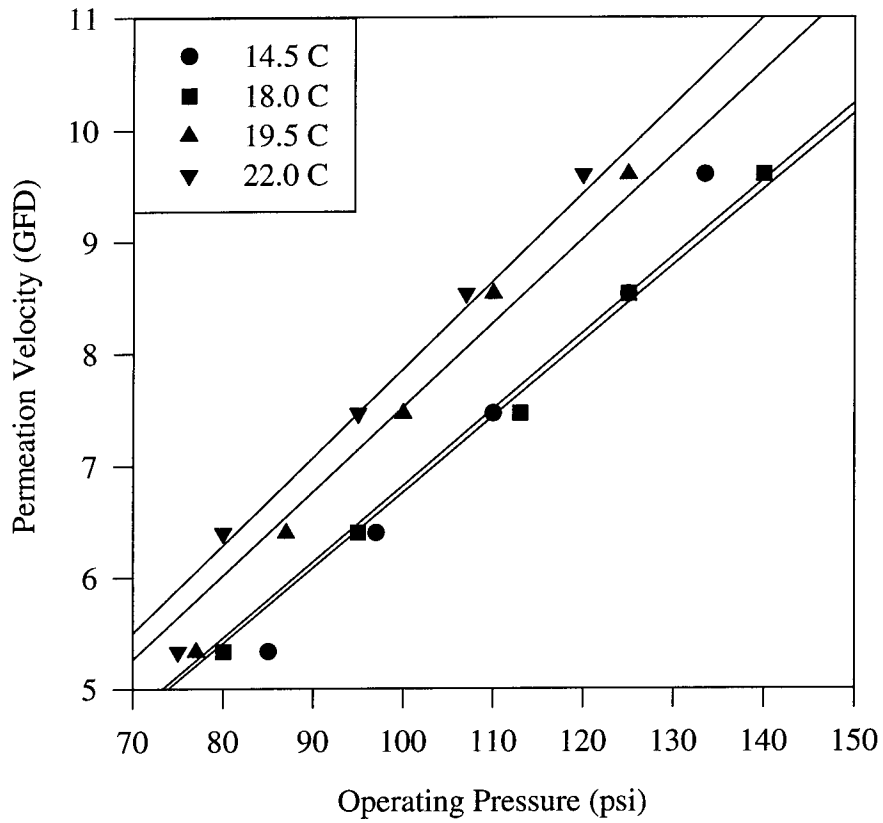


Figure 3.2: Pure water permeability tests for constant feed flow of 2.0 GPM. Permeation velocity in GFD versus operating pressure in psi; the permeability coefficient A is defined by the slope of the best-fit lines.

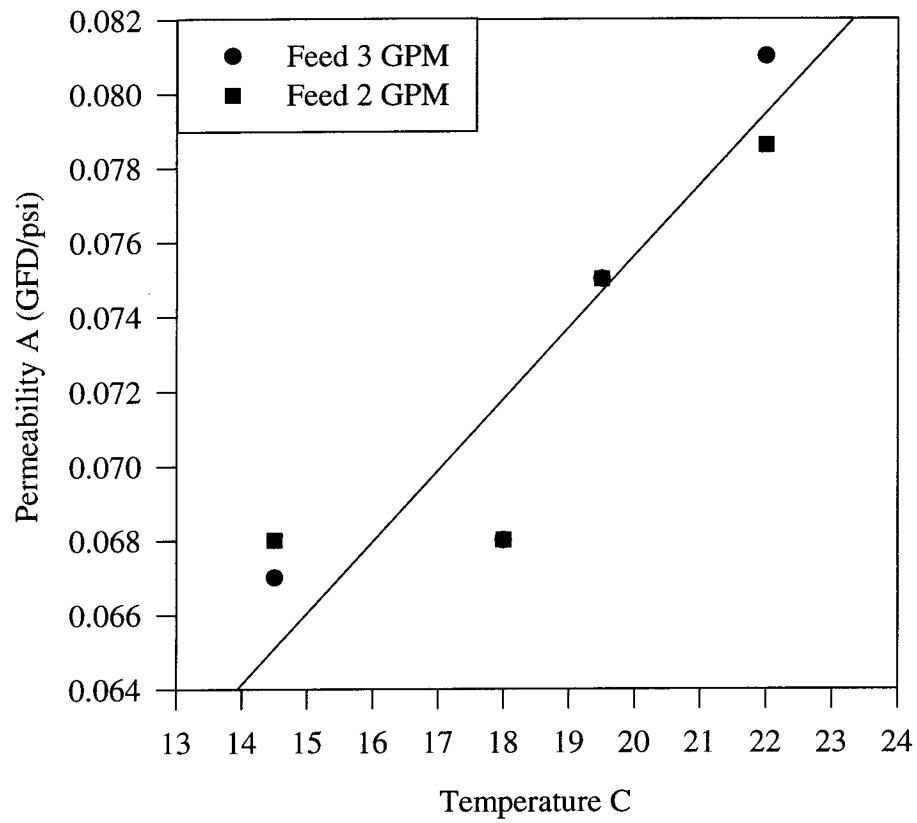


Figure 3.3: Permeability coefficient A (GFD/psi) versus ambient temperature in °C for constant feed flows of 2 and 3 GPM.

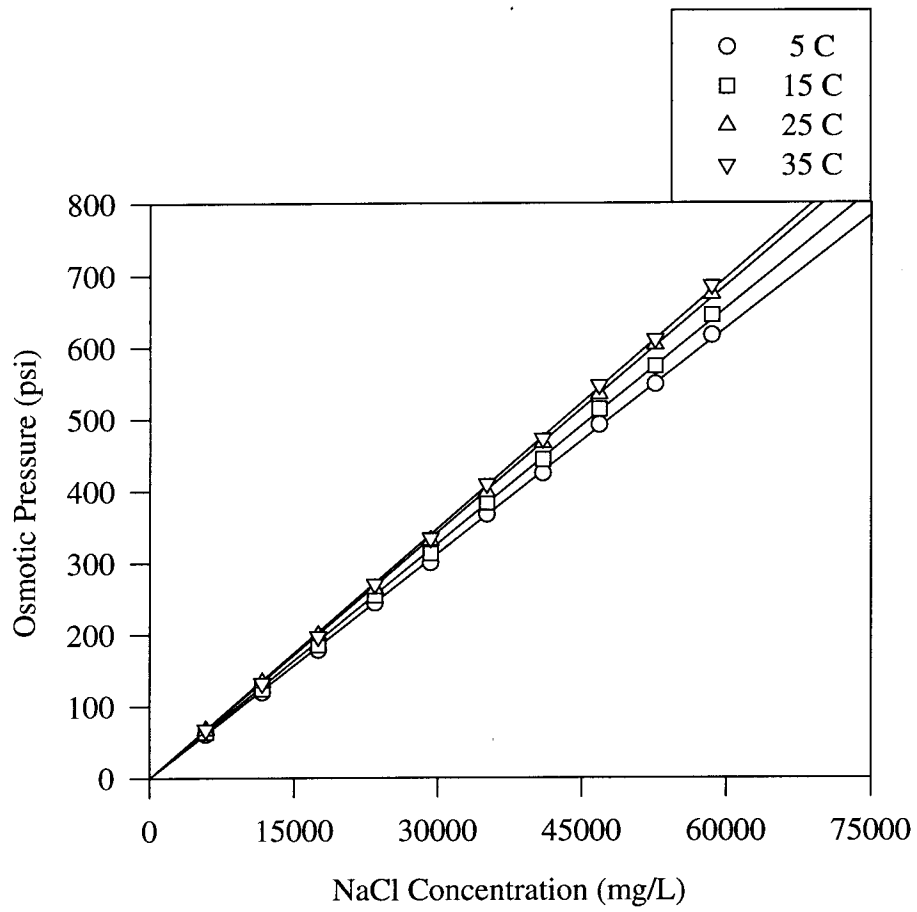


Figure 3.4: Osmotic pressure versus solute (NaCl) concentration at various temperatures (Data from Sourirajan [1970]).

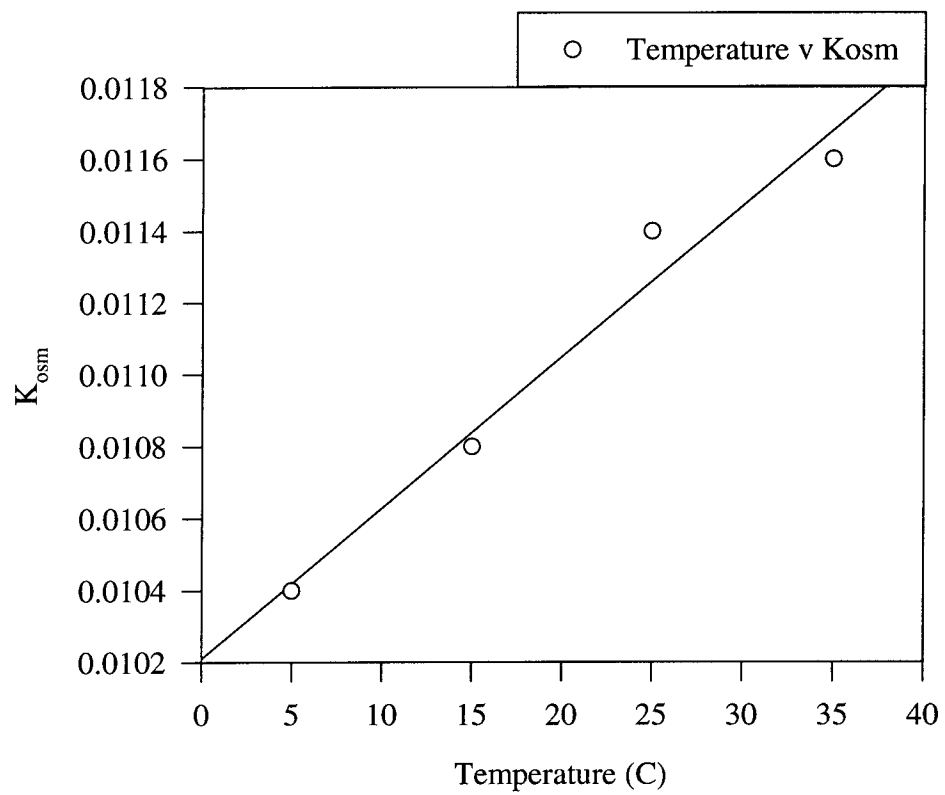


Figure 3.5: Osmotic pressure constant K_{osm} (psi.L/mg) versus temperature based on data from Sourirajan [1970].

The experiments in this study were conducted at room temperature (20-25 °C) and therefore parameters corresponding to these temperatures were used in the model.

3.1.3 Numerical Solution of Model Equations

Finite Difference Equation

A finite difference (FD) formulation was employed to solve Equation 88 and the supporting fluid flow and membrane permeation equations. First and second order partial differential equations are generally classified as elliptic, parabolic, and hyperbolic depending on the nature of the physical problem represented [Hoffman, 1992]; equilibrium problems are represented by elliptic equations while propagation problems are represented by parabolic and hyperbolic equations. Examples of elliptic equations include steady state heat conduction and mass diffusion; examples of parabolic equations include unsteady state phenomena dominated by diffusion alone or by diffusion and convection equally while examples of hyperbolic equations include pure convection or wave propagation phenomena. Different techniques are used to solve these equations as they give rise different types of numerical instability and error [Hoffman, 1992]. In this case, Equation 95 is numerically parabolic in the transverse direction and hyperbolic in the axial direction.

A three dimensional numerical grid was established to represent the two spatial coordinates and time as shown in Figure 3.6. The following FD analogs were chosen for each of the terms in Equation 95; these included a space averaged center-difference analog for time derivative, a time averaged center-difference analog for the axial

derivative, and modified Crank-Nicholson analogs for the transverse derivatives. The analogs were written at the center of the grid unit and the subscripts i , j and n refer to axial, transverse and time coordinates.

$$\frac{\partial C}{\partial T} = \frac{\partial C}{\partial T} \Big|_{i-\frac{1}{2}, j, n+\frac{1}{2}} = \frac{1}{2} \left\{ \frac{C_{i-1, j, n+1} - C_{i-1, j, n}}{\Delta T} + \frac{C_{i, j, n+1} - C_{i, j, n}}{\Delta T} \right\} \quad (105)$$

$$U \frac{\partial C}{\partial X} = U \Big|_{i-\frac{1}{2}, j, n+\frac{1}{2}} \cdot \frac{\partial C}{\partial X} \Big|_{i-\frac{1}{2}, j, n+\frac{1}{2}} \quad (106)$$

where

$$\frac{\partial C}{\partial X} \Big|_{i-\frac{1}{2}, j, n+\frac{1}{2}} = \frac{1}{2} \left\{ \frac{C_{i, j, n} - C_{i-1, j, n}}{\Delta X} + \frac{C_{i, j, n+1} - C_{i-1, j, n+1}}{\Delta X} \right\} \quad (107)$$

$$V \frac{\partial C}{\partial Y} = V \Big|_{i-\frac{1}{2}, j, n+\frac{1}{2}} \cdot \frac{\partial C}{\partial Y} \Big|_{i-\frac{1}{2}, j, n+\frac{1}{2}} \quad (108)$$

where

$$\begin{aligned} \frac{\partial C}{\partial Y} \Big|_{i-\frac{1}{2}, j, n+\frac{1}{2}} = \frac{1}{4} \left\{ \frac{C_{i-1, j+1, n} - C_{i-1, j-1, n}}{2\Delta Y} + \frac{C_{i-1, j+1, n+1} - C_{i-1, j-1, n+1}}{2\Delta Y} \right. \\ \left. + \frac{C_{i, j+1, n} - C_{i, j-1, n}}{2\Delta Y} + \frac{C_{i, j+1, n+1} - C_{i, j-1, n+1}}{2\Delta Y} \right\} \end{aligned} \quad (109)$$

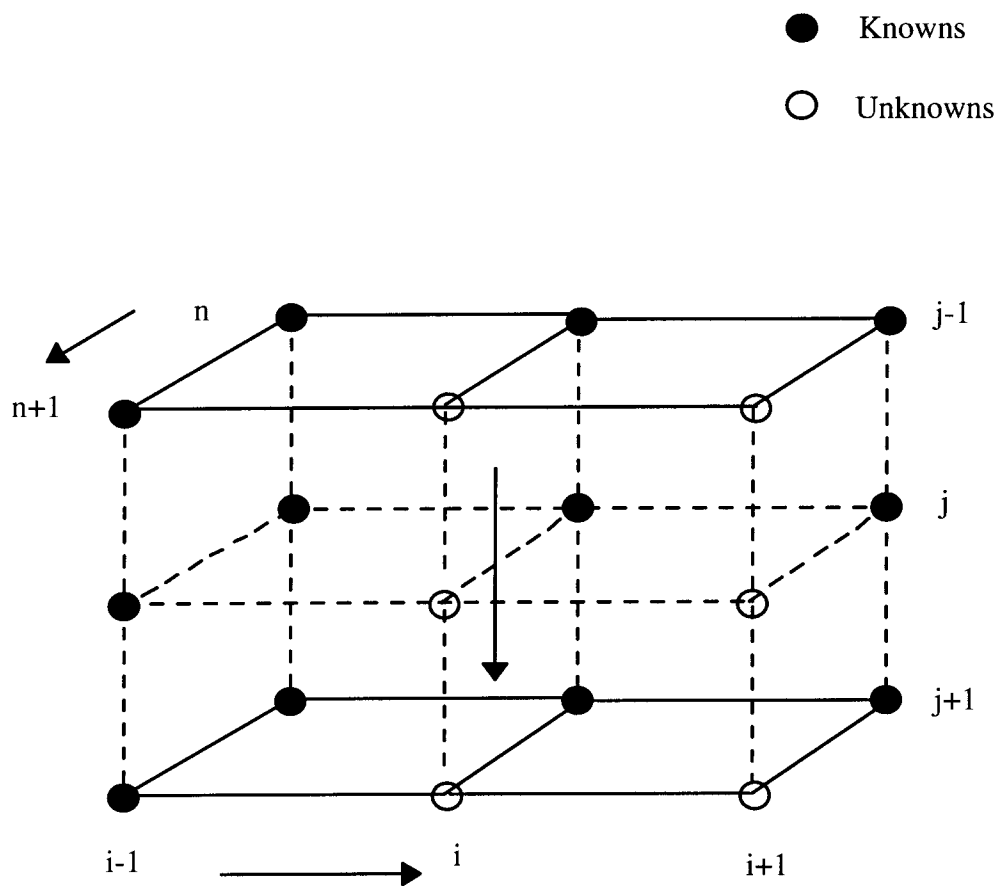


Figure 3.6: Graphical representation of the finite difference (FD) solution.

$$\begin{aligned}
D \cdot \frac{\partial^2 C}{\partial Y^2} = D \cdot \frac{1}{4} & \left\{ \frac{C_{i-1,j+1,n} - 2C_{i-1,j,n} + C_{i-1,j-1,n}}{\Delta Y^2} + \right. \\
& \frac{C_{i-1,j+1,n+1} - 2C_{i-1,j,n+1} + C_{i-1,j-1,n+1}}{\Delta Y^2} + \\
& \frac{C_{i,j+1,n} - 2C_{i,j,n} + C_{i,j-1,n}}{\Delta Y^2} + \\
& \left. \frac{C_{i,j+1,n+1} - 2C_{i,j,n+1} + C_{i,j-1,n+1}}{\Delta Y^2} \right\}
\end{aligned} \tag{110}$$

The axial and transverse velocities at the center were calculated employing four-point average method as follows:

$$U_{i-\frac{1}{2},j,n+\frac{1}{2}} = \frac{1}{4} \left\{ U_{i-1,j,n} + U_{i,j,n} + U_{i-1,j,n+1} + \underline{U_{i,j,n+1}} \right\} \tag{111}$$

$$V_{i-\frac{1}{2},j,n+\frac{1}{2}} = \frac{1}{4} \left\{ V_{i-1,j,n} + V_{i,j,n} + V_{i-1,j,n+1} + \underline{V_{i,j,n+1}} \right\} \tag{112}$$

All the unknowns in Equations 105-112 (terms that are underlined) are rearranged to yield an equation of the form:

$$a_j \cdot C_{i,j-1,n+1} + b_j \cdot C_{i,j,n+1} + d_j \cdot C_{i,j+1,n+1} = e_j \tag{113}$$

where a_j , b_j and d_j are coefficients that involve constants and velocities as computed using Equations 111 and 112 while e_j is the term that involves constants, known concentrations and velocities. It should be noted that the last term in Equations 111 and 112 are unknowns that depend on solute concentration at the membrane surface at the new time level. An iterative technique as detailed in the next section was employed to circumvent this problem. Equation 113 was solved using the tri-diagonal Thomas algorithm incorporating the necessary boundary conditions [Hoffman, 1992].

Solution Sequence

As the permeation recoveries were relatively significant (above 50%), the following method was used to solve the mass balance equations. The spiral wound unit was divided into K equal elements axially; the values ranged from 1 to 10 depending on the size of the module and the initial operating recovery. Each element was individually scaled in the same manner as Equations 88-94; however, element characteristics and initial axial velocities at each inlet were employed for scaling. The overall effect was of solving the mass balance equation successively for K elements with low recoveries in contrast to solving the mass balance as a single unit operating at high recovery. This procedure increased the computation time but considerably decreased numerical stability problems and also increased the overall accuracy of the model.

The computation was started at the inlet to the first element ($K=1$). The solute concentration values at $n=1$ (old time level) were computed for all values of i and j from the initial condition; simultaneously, the concentration values at $n=2$ (new time level) were computed for $i=1$ and all values of j from the axial boundary condition at the inlet.

Thus, the concentrations are known for three columns shown in Figure 3.6 marked by dark circles; the last column consists of terms with unknown solute concentrations and velocities, and therefore equations analogous to Equation 113 are written for all transverse grid points from $j=1$ to $j=j_{\max}$ based on solute mass balance, and arranged tri-diagonally. The first term of the first equation ($aC_{i,1,n+1}$) and the third term of the last equation ($dC_{i,j_{\max},n+1}$) are eliminated employing the two transverse boundary conditions at $Y=0$ and $Y=1$. The remaining equations are conveniently solved for concentration values employing the Thomas algorithm.

The velocities that are required to compute the coefficients a, b and d are based on four-point average as in Equations 111 and 112; these velocities are dependent on solute concentration at the old and new time levels. In order to remove this non-linearity, an iterative technique is employed; the velocities at the new time level and at $i=2$ are assumed to be equal to old time level values for the first guess, the coefficients a, b and d are then computed and equation 113 is solved for all values of j at $i=2$. The new solute concentration is used to compute the osmotic pressure from Equation 104, and the membrane permeation velocity at the new time level from Equation 103; the new value is then substituted in the transverse velocity profile (Equation 101) to obtain values for all j . The axial velocities at the new time level are subsequently computed from an incremental flow balance. These values are substituted in Equations 111 and 112, and the procedure is repeated to convergence. For this study, a convergence criterion of 0.5% was chosen for old and new values of the permeation velocity.

The solution progresses through successive axial increments until all the grid concentrations are computed at the new time level for the first element ($K=1$).

Simultaneously, the permeation velocities are computed and integrated axially to yield the permeate flow for this element at the new time level. The calculations proceed through successive elements ($K=2,3..$) until all the elements are solved for solute concentrations at the new time level. The permeation velocities in individual elements are computed as before and integrated to yield permeate flows for the elements; the permeate flows for each element are summed up to yield the total permeate flow from the module at the new time level. Calculations proceed through successive time steps until steady state is attained.

The model was also extended to include recycle flow; it was assumed that at the start of each run, the fluid flow (pure water) was at steady state with constant recycle. In this case, the introduction of solute in the feed flow does not appear as a constant boundary condition at the inlet; it starts at a numerically lower value than the feed concentration because of recycle mixing. As time progresses, the recycle solute concentration increases consequently increasing the inlet feed concentration to a constant value at steady state. However, this did not disturb the sequence of calculations in the numerical model.

Computer Program

A computer program was written in FORTRAN for the model described previously. After analyzing the model for stability, five or ten transverse grid elements were found to be sufficient; a time step equal to one-two hundredth of the nominal residence time was chosen for each element in the module. As the CDE was hyperbolic in the axial direction, the same number of axial steps were also chosen; a characteristics averaging

scheme is more suitable for hyperbolic equations where the axial grid steps are taken in proportion the axial velocity propagation. In this study however, the axial velocities varied from the inlet to exit section of each element and also in the transverse direction making it difficult for characteristics averaging to be employed. Some numerical error from numerical dispersion is unavoidable because of the presence of non-uniform velocity profiles. However in the model, the division of the spiral wound module into several axial elements gave the effect of solving low recovery problems successively and thus decreased the magnitude of the numerical error in the axial direction. The program was run on an IBM RISC 6000/550E power station. For a typical transient run from start-up to steady state involving five hundred to thousand time steps, approximately one minute of computing time was required; this time could be further reduced if larger time steps are taken as the problem reaches steady state. Because of the speed of computation, model was used to predict behavior for a range of operating pressures, feed concentrations and ambient conditions; the results are discussed in chapter 4.

3.2 Experimental Methods

A pilot-scale RO unit that was operated in Lake Arrowhead, CA as a part of a reclamation study was used to verify model results experimentally. A brief summary of the membranes that were used is given in Table 3.1. The unit was purchased from DESAL Inc., and consisted of three spiral wound RO elements 40 inches in length and 4 inches in diameter placed in series in a single module, and mounted on a transportable skid with the along with two feed pumps, cartridge filters, and stainless steel piping. A centrifugal booster pump was used to push the flow across two one-micron cartridge filters to remove any particulates while a positive displacement pump was used to

Table 3.1: Feed and operating conditions, and membrane characteristics of the spiral wound RO unit employed in this study for experimental verification and parametric analysis.

Membrane Description
Module type: spiral wound RO
Number of elements: 3
Membrane type: thin-film composite
Membrane Characteristics
Solute rejection R: 0.98
Permeability A (20 °C): 0.078 GFD/psi (5.3E-04 cm/sec-Mpa)
Channel width 2H: 30 mils (0.0762 cm)
Length per element L': 40 in (1.01 m)
Area per element Ar': 90 ft ² (8.36 m ²)
Operating Conditions
Ambient temperature T _g : 293 K
Operating pressure: 100-180 psi (0.7-1.25 Mpa)
Flow regime: Laminar
Feed Reynolds number Re: 101
Feed flow Q ₀ : 4320 GPD (1.9E-04 m ³ /sec)
Initial inlet velocity u ₀ : 0.06 m/sec
Fluid Properties
Feed solute concentration: 1000 mg/L
Solute diffusivity: 1.61E-09 m ² /sec
Osmotic pressure constant K _{osm} : 0.01 psi.L/mg

develop the dynamic head (up to 300 psi) necessary for RO separation. The design flow ranged from 3-5 GPM for permeate recoveries between 50 to 95%. The feed to the unit was NaCl-water solutions prepared from 'pure water' with electric conductivity (EC) less than 10 $\mu\text{mhos/cm}$, and non-iodized salt. The pure water was essentially RO treated produced in batches of 250 gallons for each experiment from the community drinking water in Lake Arrowhead; this procedure was used instead of using laboratory grade DI water because an unusually large quantity (250 gallons) was required to prepare the feed solution for each experimental run. As this procedure for producing pure water inevitably fouled the membranes, the permeability data was collected on 'used' membranes at the end of all the experimental runs instead of the newly purchased membranes. Thus in all the development of the model, an adjusted value of the membrane permeability A was used to include any fouling and/or degradation effects instead of the clean membrane permeability.

Parameters such as fluid temperature, operating pressures and fluid concentrations were measured during and at the end of each experimental run to facilitate both transient and steady-state analysis. Each experimental run was conducted for one hour which was approximately five times the feed side residence time; it was estimated from preliminary runs that this time period was sufficient for steady-state conditions to develop. Since the main emphasis of the experiments was only verify transient and steady-state CP behavior, all the experimental runs were limited to one hour. The data were collected in intervals of two minutes for the first 20 minutes, and in intervals of 10 minutes for the remaining forty minutes. Temperature was measured using an on-line temperature probe, and inlet and downstream operating pressures were measured using on-line pressure gauges. Feed,

permeate and concentrate concentrations were measured employing an EC meter; it was assumed that EC was linearly related to the salt concentration.

Four different feed NaCl concentrations (200, 500, 1000 and 2000 mg/L) in addition to pure water were used to study the effect of feed solute concentrations on CP and flux decline. In addition, two feed flow rates (2 GPM and 3 GPM) and three different recycle rates (recycle ratios of 0.0, 0.5 and 1.0) were used to verify the effects of different cross-flow velocities. All the experiments were performed in the temperature range of 18 to 20 °C.

P-Pressure gauge
T-Temperature
F-Flow meter

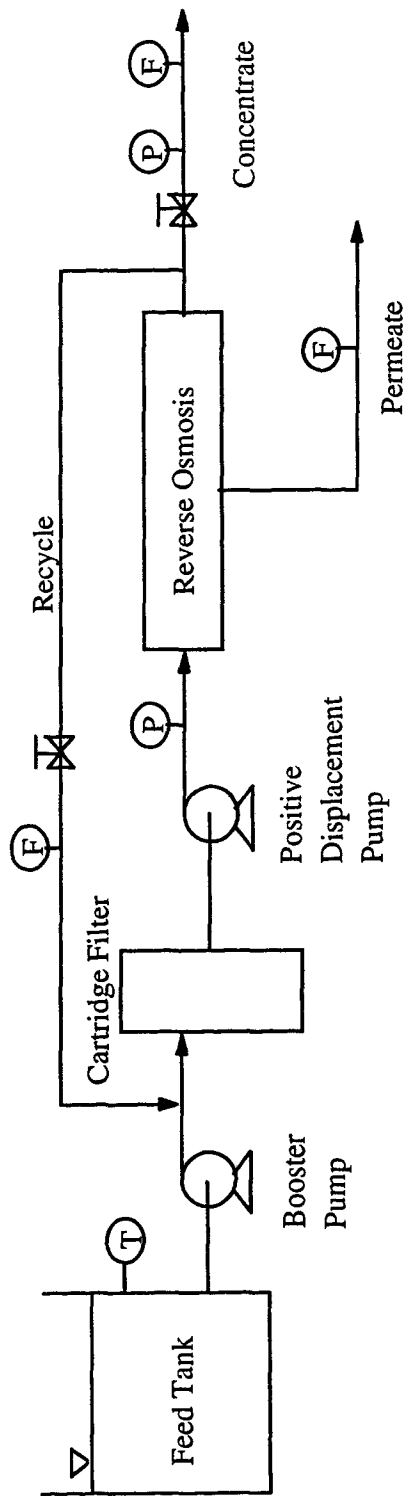


Figure 3.7: Schematic description of the pilot-scale spiral wound RO unit.

CHAPTER 4

RESULTS AND DISCUSSION

The numerical model was used to generate transient and steady-state CP and permeate flux decline behavior in spiral wound membranes for a various feed and operating conditions. However, the model was first tested for numerical stability, consistency and accuracy through parametric studies; the model was also verified with experiments performed on a pilot-scale spiral wound RO unit for separation of NaCl solutions. These results are discussed in this chapter.

4.1 Numerical Stability

Stability is generally associated with propagation problems where the solution develops in time; these problems are represented by parabolic and hyperbolic equations. A finite difference (FD) method is considered stable if it produces a bounded solution when the exact solution is bounded, and is unstable if it produces an unbounded solution when the exact solution is bounded [Hoffman, 1992]. FD methods for parabolic and hyperbolic equations are accordingly classified as stable, conditionally stable and unstable. If the solution is bounded for all values of grid and time spacings i.e., the numerical error decreases as the solution propagates in time, the method is stable. If the solution is bounded only for certain values of grid and time spacings, the method is considered conditionally stable. If the solution is unbounded for all values of grid and time spacings, the method is considered unstable.

In this study, the CDE (Equation 86) consisted of coefficient terms that varied spatially as well as in time and therefore some stability problems were anticipated. In order to minimize these problems, an analysis of error propagation as a function of time and grid spacings was performed before generating CP information for any specific conditions. The more direct stability analysis based on the von Neumann method or the matrix method was not performed because of the non-linearities that existed in the CDE which made such analysis difficult.

Solute concentration on the membrane surface ($Y=1$) and at the axial mid-point ($X=0.5$) after a time $t = t_r$ corresponding to the residence time on the feed side of the membrane was chosen for stability analysis. For instance, the variation of $C(0.5,1.0,t_r)$ with respect to time and grid spacings for the conditions listed in Table 3.1 are plotted in Figures 4.1, 4.2 and 4.3. For the method to be stable, the concentration at any specific point in the solution domain should be independent of time and grid spacings; however, for conditionally stable methods, the solution is independent of the time and grid spacings within a limited range.

The variation of $C(0.5,1.0,t_r)$ was plotted independently versus ΔT and ΔY to test the error in the parabolic (transverse) direction (Figures 4.1 and 4.2); it was concluded that the method was conditionally stable in this direction. A preliminary analysis based on several model runs revealed that the stability criterion was of the form

$$D \cdot \frac{\Delta T}{\Delta Y^2} \leq \epsilon \quad (114)$$

where ε depended on several factors including axial and permeation velocities, solute diffusivity and membrane permeability; this condition is similar to the stability criterion of an explicit forward difference solution of a one-dimensional parabolic equation. The result was initially surprising since the solution employed an apparent implicit method; implicit methods generally produce stable solutions. However, a more careful analysis revealed that the computation at every axial column $(i, n+1)$ depended on three columns of known values at $(i-1, n)$, (i, n) and $(i-1, n+1)$ as shown in Figure 3.3; thus, the method was more explicit than implicit, and therefore conditionally stable. Another difficulty was caused by the non-linear CP boundary condition at the membrane surface where both the solute concentration and permeation velocity were unknown; this problem was minimized by assuming sufficiently small time increments for computation at each time level. For the operating conditions involved in this study, the value of ε ranged from 0.2 to 0.4 depending permeate recovery. This variation indicated that the numerical grid needed to be sized differently when permeate recovery changed; for high recoveries, smaller time increments were employed.

The CDE was hyperbolic in the axial direction, and hence numerical errors arising from numerical diffusion and dispersion were expected; the solution in the axial direction was approximately based on the method of characteristics (MOC) generally employed to avoid diffusion and dispersion errors. For one-dimensional hyperbolic equations, characteristics are lines or curves along which the numerical solution propagates. The numerical grid points are located on these curves so that information could propagate along the grid points in time.

In the present study, developing characteristic lines proved to be cumbersome because the axial velocity varied spatially and in time; instead, the average inlet velocity to each axial section and the time increment ΔT were used to locate the axial grid points according to the relationship

$$U_0^{\text{avg}} \cdot \frac{\Delta T}{\Delta X} = 1 \quad (115)$$

With this procedure some numerical error from the axial direction was unavoidable. To further to study the effect of the first term in Equation 115 is effect $C(0.5,1.0,t_r)$ was plotted versus $U\Delta T/\Delta X$ as shown in Figure 4.3. It can be concluded from the figure that a value of 1.0 for first term in Equation 115 (i.e., $\Delta T = \Delta X$) placed the solute concentration in the plateau region indicating that it was independent of the increments; higher values of the same ratio i.e., lower ΔX gave only marginally superior results and were not undertaken to save computational time. Figure 4.4 shows a plot of $C(0.5,1.0,t_r)$ versus number of axial elements, and thus the significance of dividing the membrane unit into several axial elements so that a series of low permeate recovery problems could be solved instead of one high recovery problem that yielded considerable numerical error. During this study, three axial elements were chosen to minimize this error while conserving computational time.

4.2 Accuracy

The model was also tested for numerical accuracy by comparing with results of a steady state CP model for commercial membranes. The CP model of Bhattacharya and co-workers was chosen for comparison for two reasons: (1) predicted flux behavior of

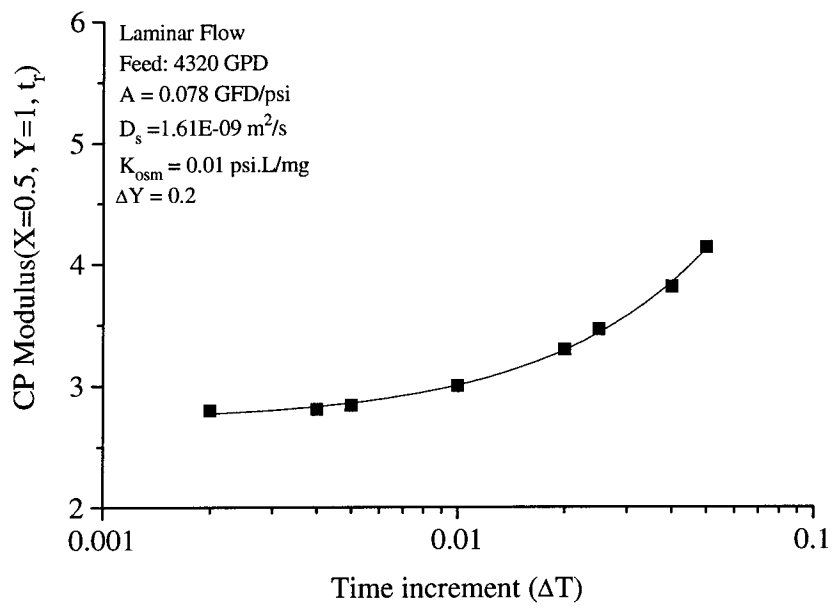


Figure 4.1: Stability as a function of time increment ΔT -CP modulus calculated at the axial mid-point on the membrane surface after t_r .

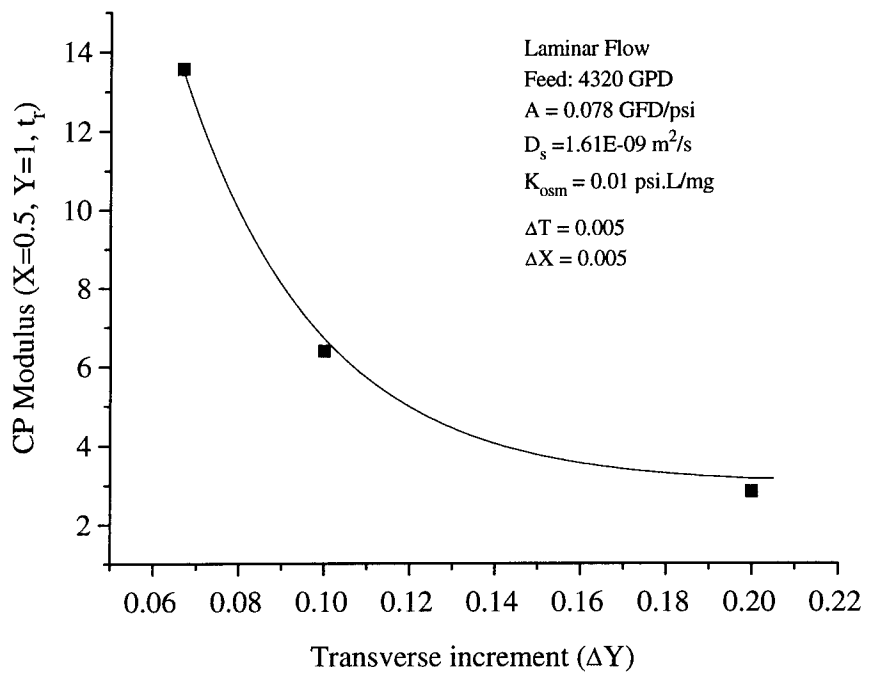


Figure 4.2: Stability as a function of transverse increment ΔY -CP modulus calculated at the axial mid-point on the membrane surface after t_r .

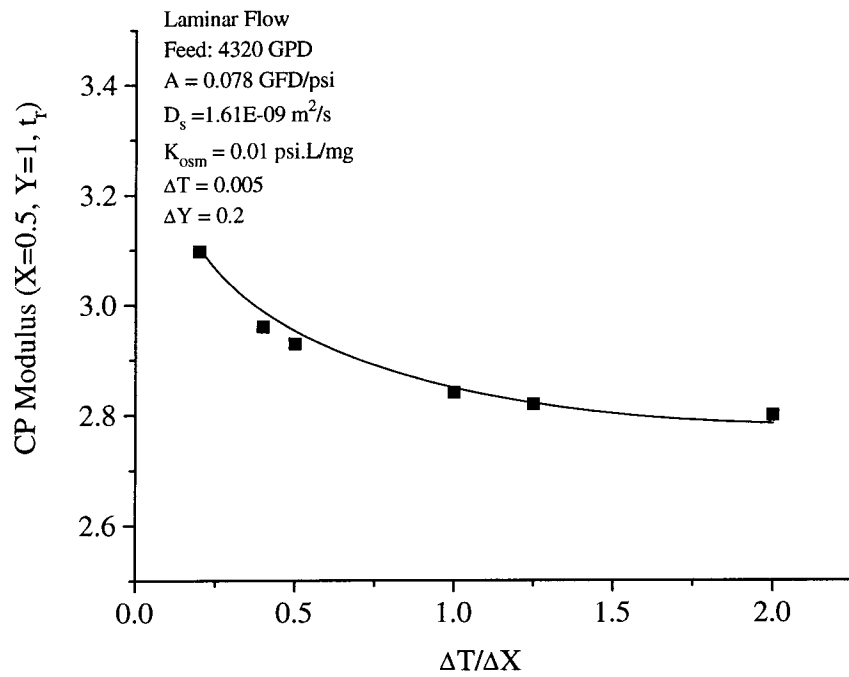


Figure 4.3: CP modulus versus ratio of time and axial increments-CP modulus calculated at the axial mid-point on the membrane surface after t_r .

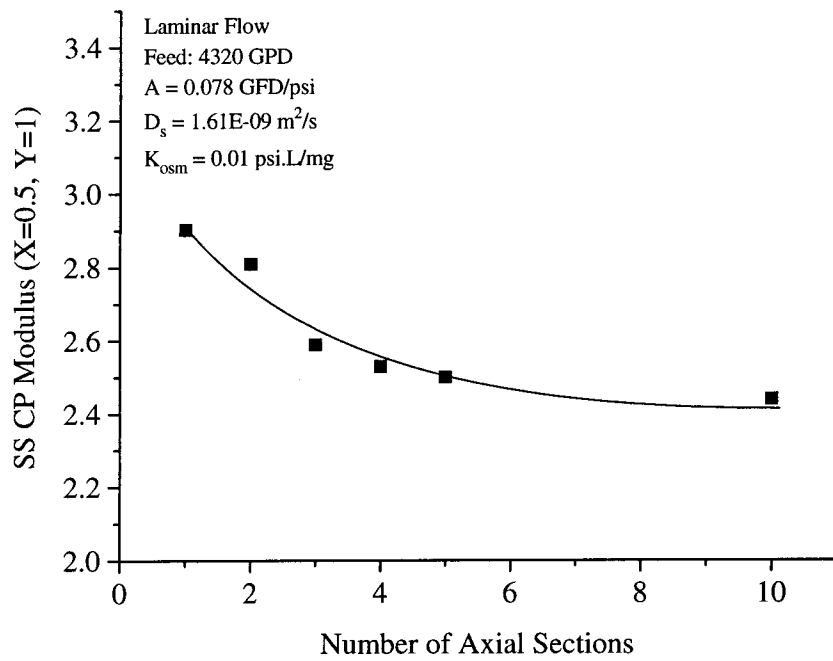


Figure 4.4: Steady state CP modulus versus number of axial divisions of the membrane unit (Operating conditions based on Table 3.1).

Table 4.1: Description of feed and operating conditions for comparisons with the
Bhattacharya FEM model (accuracy analysis).

Membrane Description
Module type: Channel flow with two porous walls
Number of membrane elements: 1
Membrane Characteristics
Solute rejection R: 0.98
Permeability A (20 °C): 0.109 GFD/psi (7.45E-04 cm/sec-Mpa)
Channel width 2H: 31.5 mils (0.08 cm)
Length per element L': 78 in (2.0 m)
Width per element W: 19.5 in (0.5 m)
Operating Conditions
Ambient temperature T_s : 298 K
Operating pressure: 440 psi (3.04 Mpa)
Flow regime: Laminar
Feed Reynolds number Re: 1333
Feed flow Q_0 : 13600 GPD (6.0E-04 m ³ /sec)
Initial inlet velocity u_0 : 0.75 m/sec
Fluid Properties
Feed solute concentration: 5000 mg/L
Solute diffusivity: 1.61E-09 m ² /sec
Osmotic pressure constant K_{osm} : 0.01 psi.L/mg

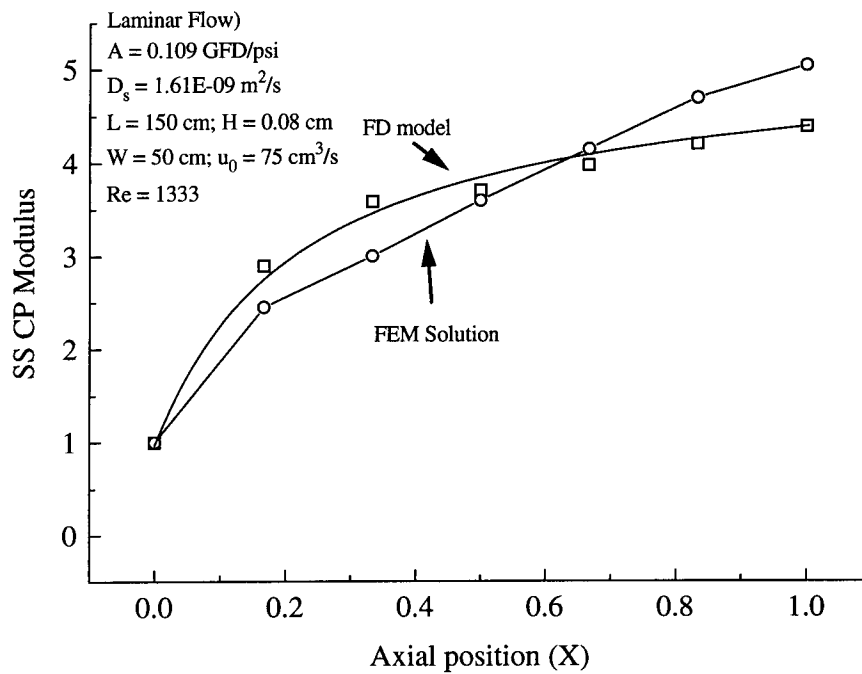


Figure 4.5: Comparison of the model with earlier steady state FEM solution by Bhattacharya [1990]: data points represent model predictions in both cases.

their model closely matched the predictions of analytical solutions of Sherwood [1966] for simplified operating conditions, and (2) the model was based on an alternate solution technique namely a finite element formulation and was therefore useful for avoiding numerical errors that are specific to finite difference formulations. The operating conditions and membrane characteristics for this comparison are listed in Table 4.1, and the results are plotted in Figures 4.5. CP build-up along the axial length of the membrane module is shown in Figure 4.5; it was found that the steady state predictions of the transient model were within 10% of the predictions of the Bhattacharya model.

4.3 Parametric Consistency

In order to verify the behavior of the model, a parametric study was also undertaken. This included varying certain key model parameters such as membrane permeability and observing the behavior of the model and ascertaining if it matched expected physical variations; for instance, increasing membrane permeability effectively increased permeation rates and therefore increased CP. In this study three parameters were chosen for verifying parametric consistency: membrane permeability A , solute rejection coefficient R and the solute osmotic pressure coefficient K_{osm} . The feed and operating conditions for these tests are listed in Table 4.1.

Figures 4.6 and 4.7 show the effect of membrane permeability A on CP and flux decline. CP modulus, which is the ratio of the solute concentration to the feed solute concentration, calculated at the axial mid-point on the membrane surface is plotted versus initial permeate recovery for various values of permeability (Figure 4.6). It was observed that the value of CP modulus steadily increased from $A=0.025$ (GFD/psi) to $A=0.1$; this is

expected since increasing A effectively increases permeation rate and therefore the transport of solute to the membrane surface.

The effect of A on permeate flux decline was also plotted to confirm this result (Figure 4.7). Steady state values of permeate flow (in GPD) were plotted versus initial permeate flow (also in GPD); in the absence of CP, which is the case for pure water, it is expected that such a plot will be linear with a slope of unity i.e., there is no change in the permeate flux over time. However, the presence of solute results in CP and therefore the permeate flux decreases over time and eventually reaches a steady state value that is lower than the starting flux. The overall decline is dependent on factors that aggravate CP; for instance, increasing permeability increases CP and causes a greater permeate flux decline. This result is depicted in Figure 4.7 where higher values of A cause the flux curves to bend towards the abscissa; conversely, lower values of A result in curves that are linear to a greater extent reflecting low CP.

Figures 4.8 and 4.9 show the effect of solute rejection coefficient R on CP and flux decline. From a physical viewpoint, decreasing R results in passage of solute molecules across the membrane barrier instead of accumulating near the surface. From Figure 4.8, it can be observed that decreasing R from 98% to 60% results in lower values of CP modulus at the membrane surface confirming the physical intuition. The steady state permeate flow plot (Figure 4.9) also reveals the same result namely lower values of R do not cause significant variation in permeate flux decline.

Figures 4.10 and 4.11 show the effect of osmotic pressure coefficient K_{osm} on CP and flux decline. K_{osm} indicates the magnitude of osmotic pressure that is induced by a

solute; increasing K_{osm} results in a high value of $\Delta\Pi$ and therefore an overall decrease in the solvent driving force $\Delta P - \Delta\Pi$. This translates to lower permeation rates and therefore lower CP. Two values of K_{osm} were chosen for ascertaining parametric consistency: 0.005 psi.mg/L and 0.01 psi.mg/L. From Figures 4.10 and 4.11, it can be observed that the lower K_{osm} value causes relatively larger CP modulus and a greater permeate flux decline.

The model was also tested for parametric consistency with respect to solute diffusivity D_s ; however as it was used as a key parameter during initial scaling, it was concluded that varying D_s significantly (order of magnitude change) would automatically alter the numerical stability criterion (Equation 114) thus requiring different time and spatial increments. Instead the model runs were generated for two values of D_s : $1.61E-09$ m^2/s which is the molecular diffusivity of NaCl in water and $3.12E-09$ m^2/s which is twice the molecular diffusivity; the effect on CP and permeate flux decline is shown in Figures 4.12 and 4.13. As expected, increasing D_s decreased CP because solute back diffusion into the bulk stream is higher.

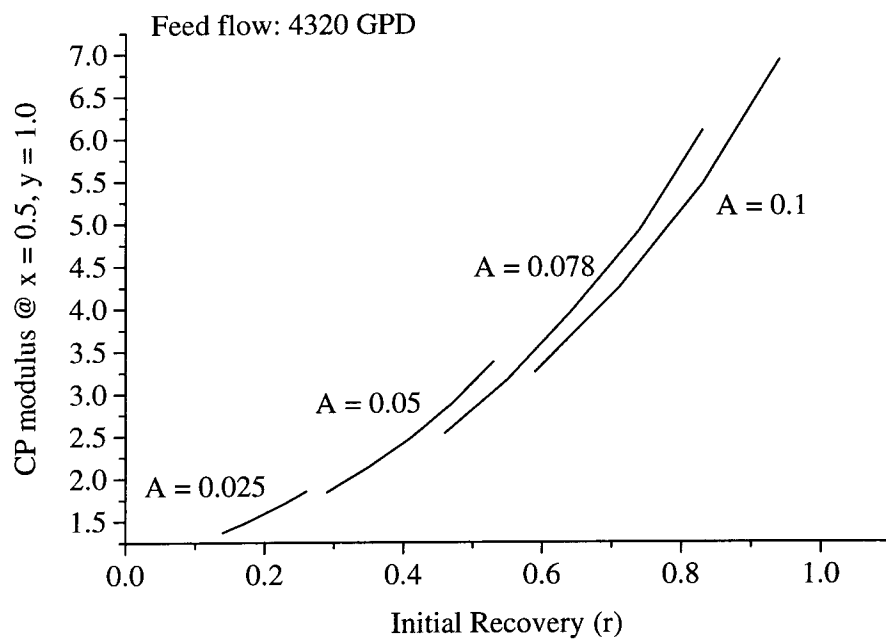


Figure 4.6: Effect of membrane permeability A on CP: plot shows the ratio of solute concentration on the membrane surface at the axial mid-point to feed solute concentration versus starting permeate recovery.

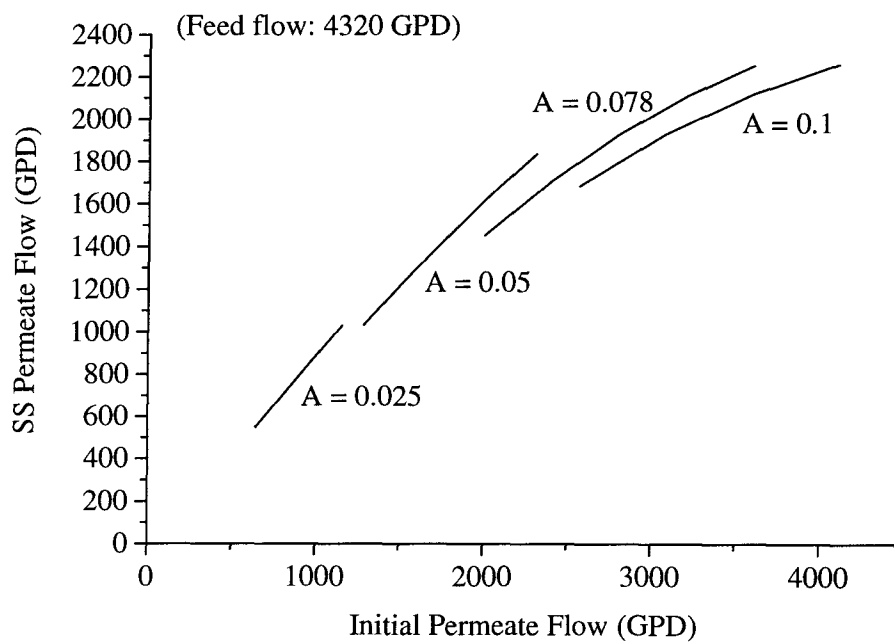


Figure 4.7: Effect of membrane permeability A on flux decline: plot shows steady state permeate flow versus initial permeate flow.

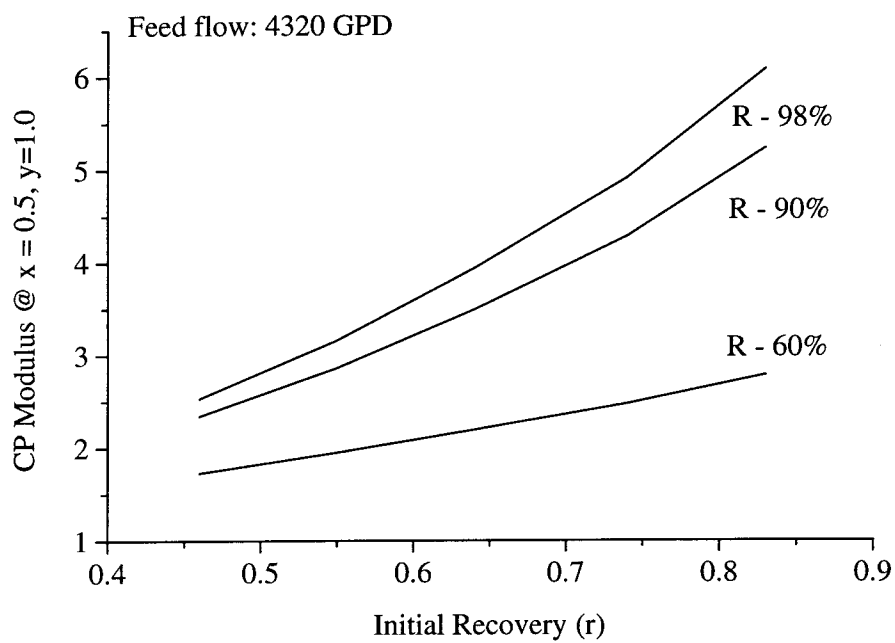


Figure 4.8: Effect of solute rejection coefficient R on CP: plot shows the ratio of solute concentration on the membrane surface at the axial mid-point to feed solute concentration versus initial permeate recovery.

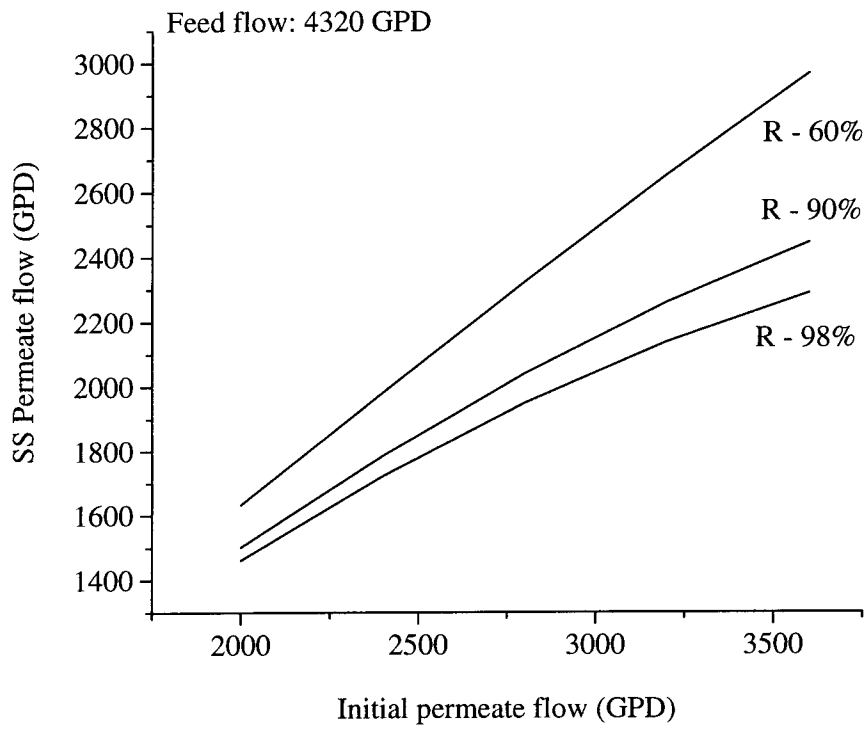


Figure 4.9: Effect of solute rejection coefficient R on flux decline: plot shows steady state permeate flow versus initial permeate flow.

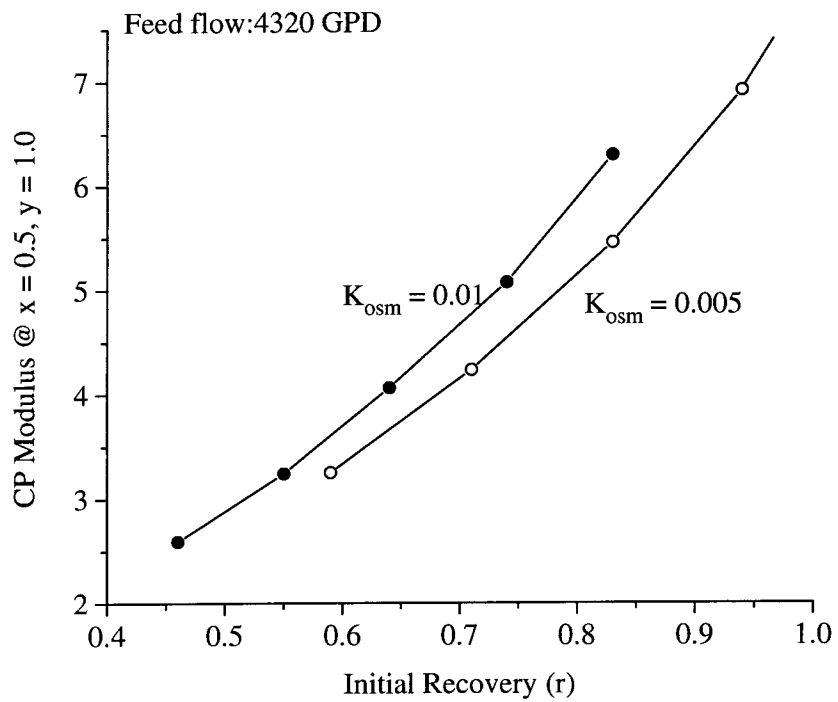


Figure 4.10: Effect of the osmotic pressure constant K_{osm} on CP: plot shows the ratio of solute concentration on the membrane surface at the axial mid-point to feed solute concentration versus starting permeate recovery.

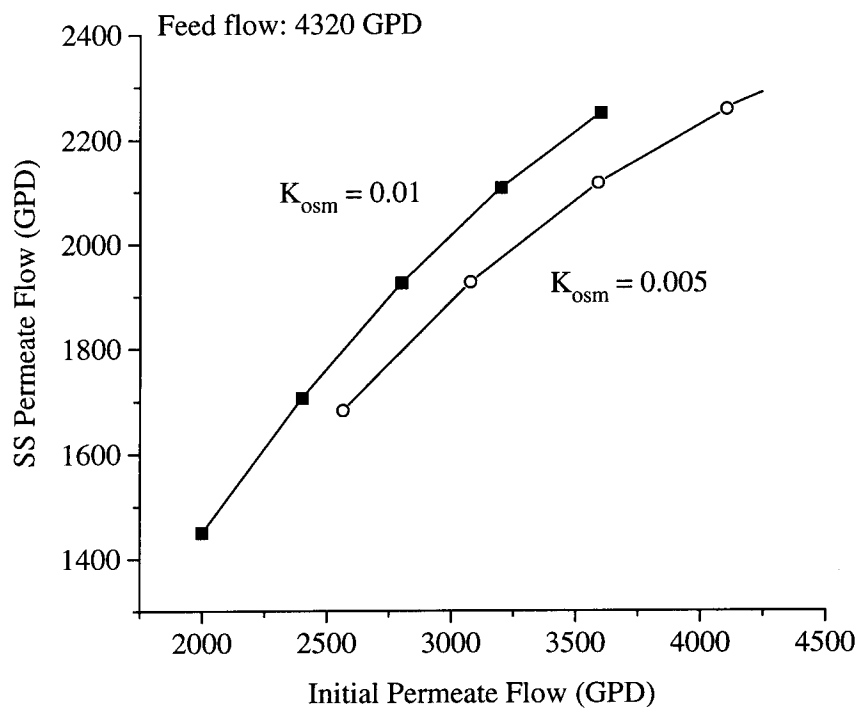


Figure 4.11: Effect of the osmotic pressure constant K_{osm} on flux decline: plot shows steady state permeate flow versus initial permeate flow.

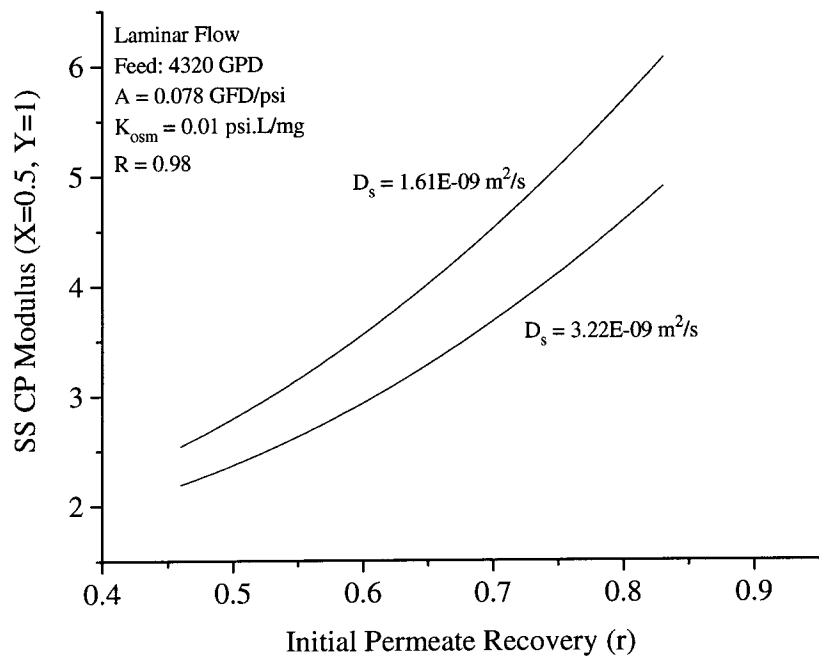


Figure 4.12: Effect of solute diffusivity D_s on CP; plot shows steady state CP modulus at the axial mid-point on the membrane surface versus D_s .

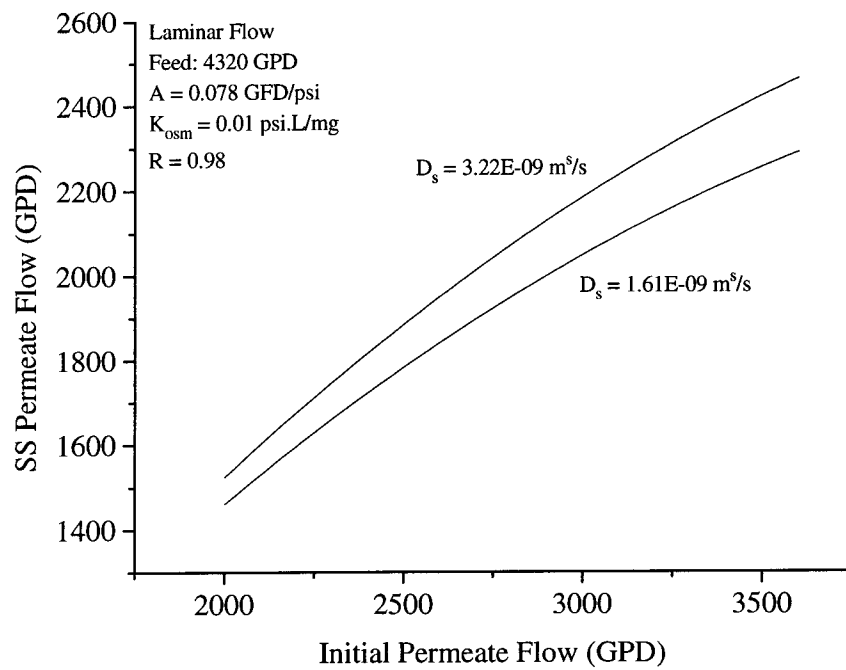


Figure 4.13: Effect of the solute diffusivity D_s on permeate flux decline: plot shows steady state permeate flow versus initial permeate flow.

4.4 Model Predictions

Once the stability, accuracy and parametric consistency of the model were established, it was used to generate information on CP and permeate flux decline for various feed and operating conditions. As mentioned in Chapter 3, three different axial velocity profiles were used to duplicate laminar flow, completely mixed flow and spacer-induced mixing (partial mixing) regimes described by Equations 97-99. Some of the results were verified with experiments and are discussed in the next section; however, in this section the important model results and the implications for design of commercial membrane facilities are discussed. The main emphasis is on flow under laminar conditions and spacer-induced mixing.

4.4.1 Laminar Flow

The model was used to generate information for various feed solute concentrations, feed flow rates, permeate recoveries and recycle flow rates. Five feed solute concentrations were chosen for model runs at 10, 200, 500, 1000 and 2000 mg/L; four feed flow rates at 2, 3, 15 and 30 GPM and three recycle rates at recycle ratios of 0.0, 0.5 and 1.0 were chosen to investigate the effect of cross-flow. In addition, the effect of ambient temperature was also investigated at 15, 20 and 25 °C. Transient flux decline data that the model is capable of generating is illustrated for laminar flow for different feed concentrations in Figure 4.14; the permeate fluxes are plotted as a function of time until steady state conditions are attained. However, this procedure was not adopted for illustrating all model results. To conserve presentation, only steady state results are shown for different feed and operating conditions, and different flow geometries.

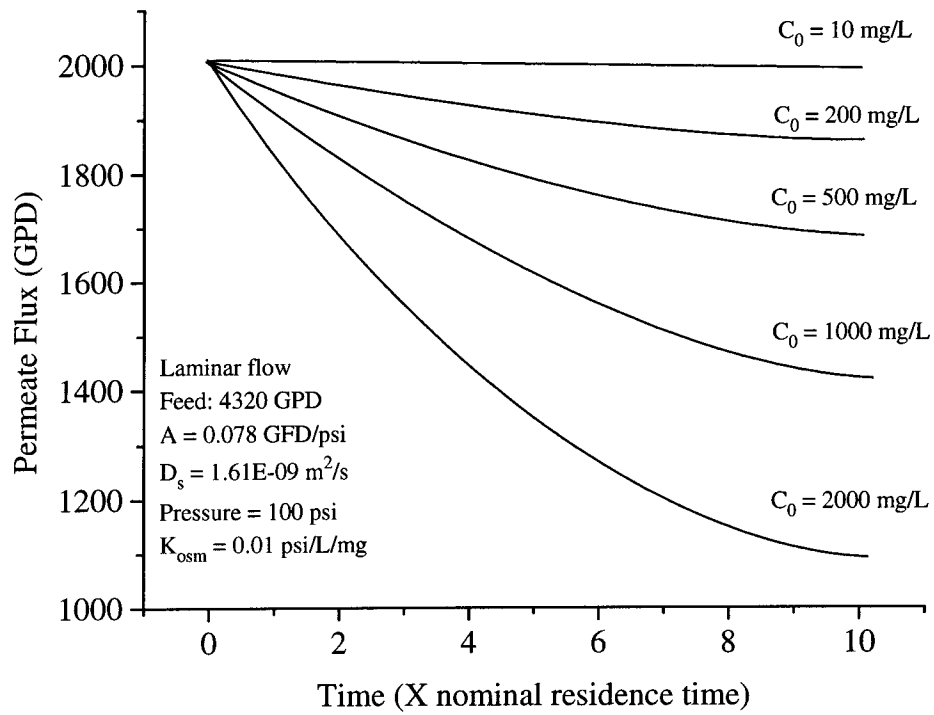


Figure 4.14: Transient state model predictions: flux decline (in GPD) is plotted versus time in multiples of nominal residence time t_r .

CP data is represented by CP modulus at the axial mid-point on the membrane surface at steady state ($X=0.5$, $Y=1.0$). Information was generated for various operating pressures (different recoveries), and therefore CP modulus was plotted versus initial permeate recovery for different feed concentrations as shown in Figure 4.15. Lower feed concentrations resulted in higher CP modulus values because of higher permeation rates. Permeate flux decline was plotted as in the case of parametric consistency runs (Figure 4.16): the steady state permeate flow (in GPD) was plotted versus the initial permeate flow (in GPD). Deviations from linearity indicated the extent of flux decline; as expected, the decline increased with increasing feed solute concentration. Since experiments were conducted only for salt concentrations ranging from 10 to 2000 mg/L, the model predictions and discussion are limited to this range. The lower concentrations ranging up to 500 mg/L reflect those found in typical municipal and industrial wastewater discharges while higher concentrations up to 2000 mg/L are representative of most brackish water sources. Though seawater desalination was not considered in this study, it is emphasized that the model is capable of predicting CP in such a case as well where salt concentrations reach up to 35,000 mg/L. From Figure 4.16 it can be concluded that for laminar flow conditions, CP can cause a permeate flux decline of up to 30% for municipal effluents with salt concentrations of 500 mg/L and a decline of up to 50% for brackish waters with salt concentrations of 2000 mg/L; this drop is considerable given the high operating costs associated with membranes.

The model runs on laminar flow where the axial velocity assumes a parabolic profile were also compared completely mixed flow regimes. In the latter case, the axial velocity was assumed to be plug flow with a flat profile defined by Equation 98. The

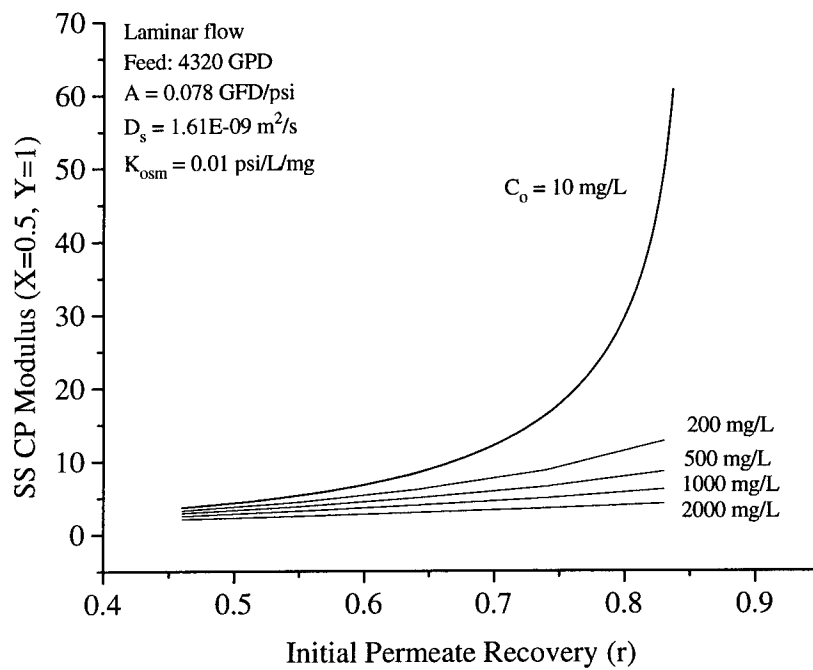


Figure 4.15: Steady state CP modulus at the axial mid-point on the membrane surface versus initial permeate recovery for various feed solute concentrations.

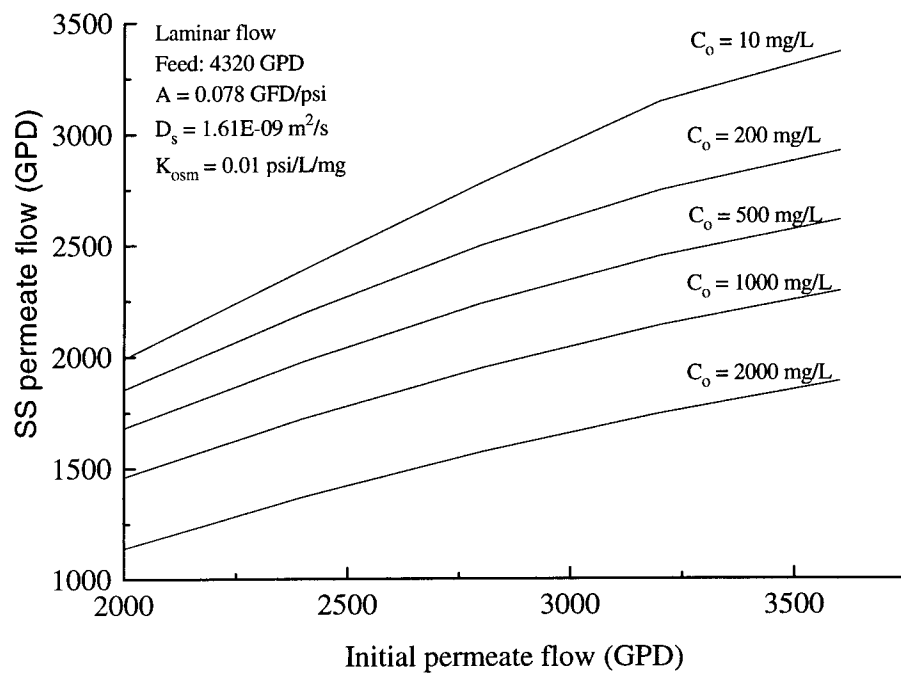


Figure 4.16: Steady state versus initial permeate flow for various feed solute concentrations for laminar flow conditions.

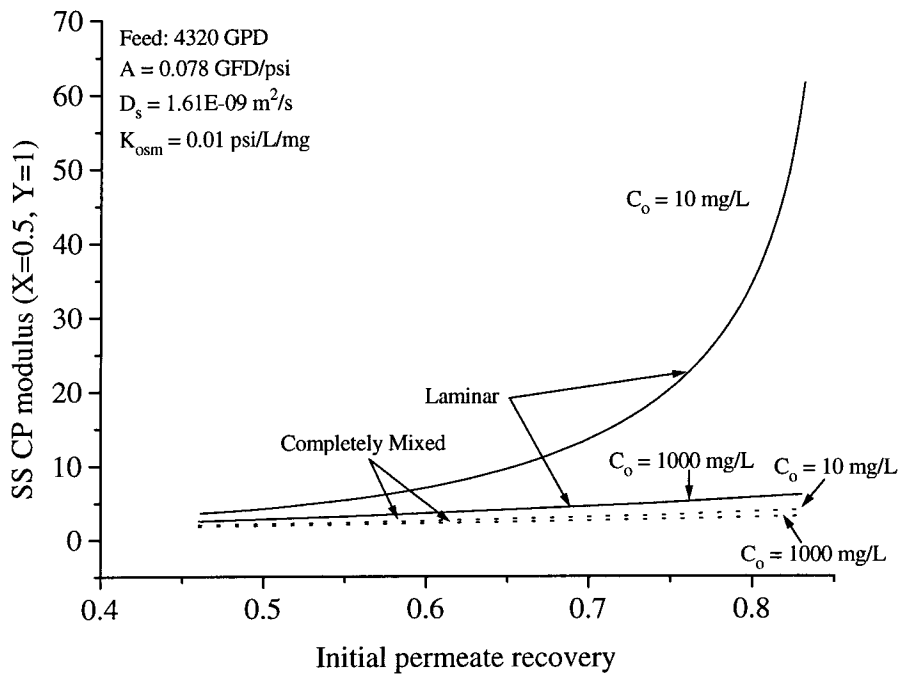


Figure 4.17: Effect of laminar vs completely mixed flow regimes on CP build-up: CP modulus is plotted versus initial permeate recovery for different feed solute concentrations.

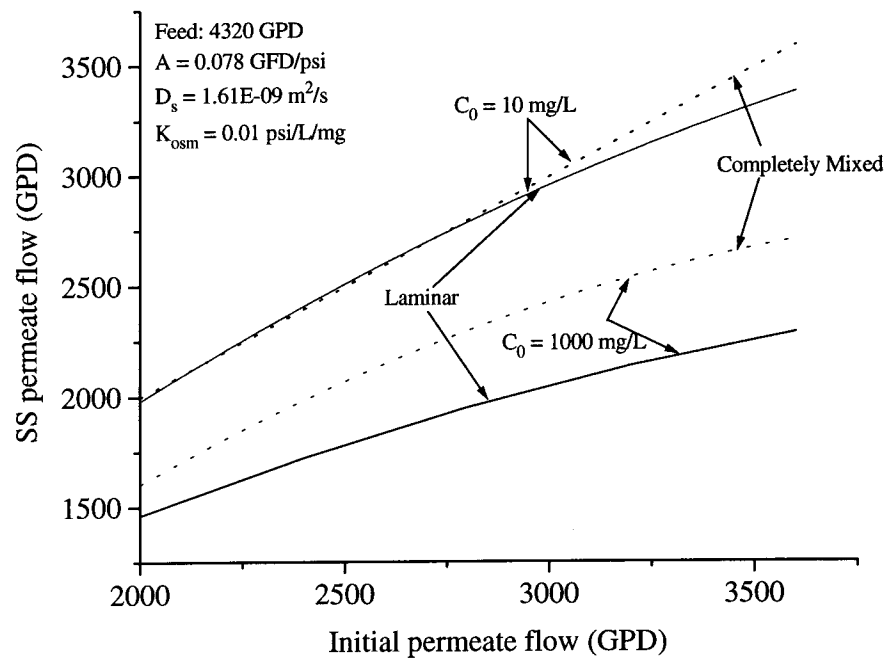


Figure 4.18: Steady-state versus initial permeate flow for laminar and completely mixed flow regimes: flux decline for two feed solute concentrations are depicted.

results are compared with respect to CP modulus and permeate flux decline for two feed concentrations: 10 mg/L and 1000 mg/L; the results are shown in Figures 4.17 and 4.18. From these figures, it can be concluded that a flat velocity profile reflecting complete mixing decreased CP because of effective mass transfer.

The effect of increasing cross-flow velocity was investigated in two ways: (1) increasing feed flow, and (2) increasing recycle flow. The effect of increasing feed flow on CP and permeate flux decline are shown in Figures 4.19 and 4.20 while the effects of recycle flow rates are shown only for flux decline in Figure 4.21; CP is not compared for the latter case because the relative feed concentration at the unit inlet increased over time as recycle water mixed with the influent flow. Two different flow rates were used to verify the model with experiments at 2 and 3 GPM; however, the model was also tested at flow rates of 15 and 30 GPM and the results from this increase which are more dramatic are shown in the figures. As expected, higher feed flow rates directly reduced CP and flux decline because of increased cross-flow and effective mass transfer.

The impact of increasing recycle flow rates was more complicated because there were competing factors that influenced CP. The increase in cross-flow velocity had the impact of reducing CP and flux decline but it also contributed to an effective increase in feed concentration because of mixing with the more concentrated recycle fluid. While the latter effect was found to be dominant at lower recycle rates (recycle ratios up to 1.0), CP was found to be reduced at higher recycle flow rates (recycle ratios above 1.0). However, the results are only preliminary and need to be verified experimentally; this is especially important at higher cross-flow velocities because of the impact on axial pressure drop. In all the above model runs, a constant axial pressure drop of 10% was assumed; this could

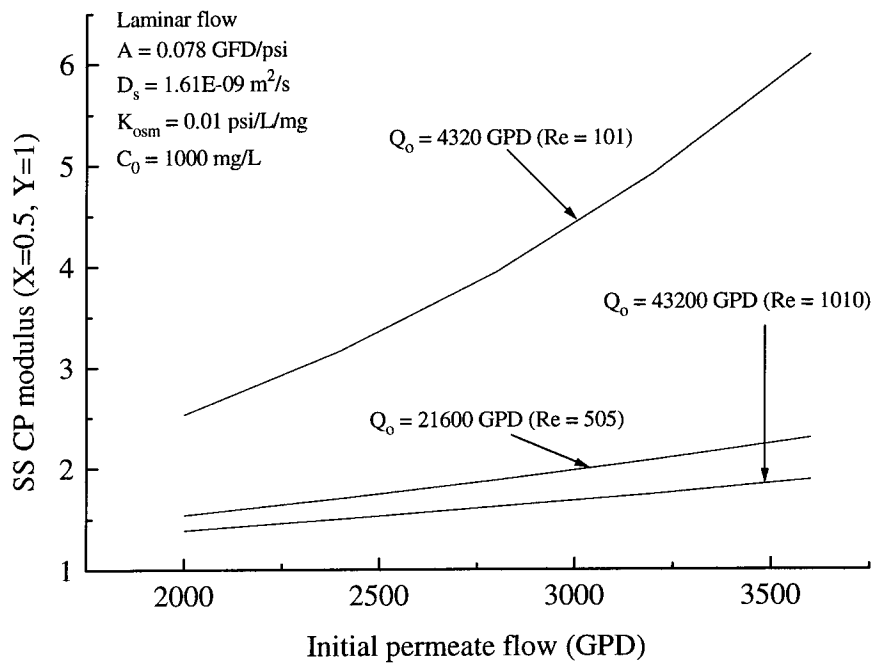


Figure 4.19: Effect of cross-flow Reynolds' number on CP through an increase in feed flow: steady state CP modulus ($X=0.5$, $Y=1$) plotted versus initial permeate flow.

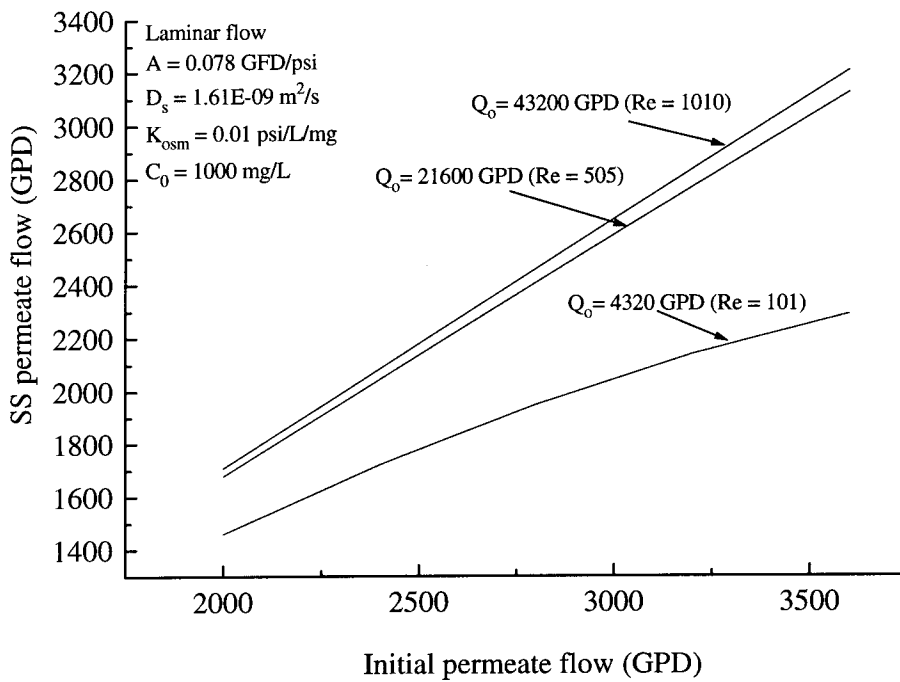


Figure 4.20: Effect of cross-flow Reynolds' number based on feed flow rate on permeate flux decline.

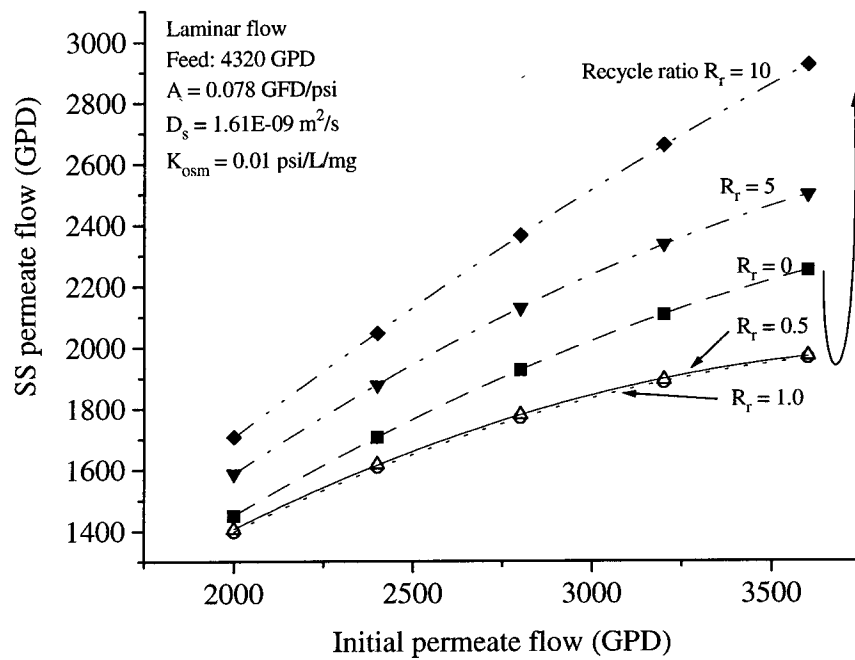


Figure 4.21: Effect of recycle ratio on permeate flux decline.

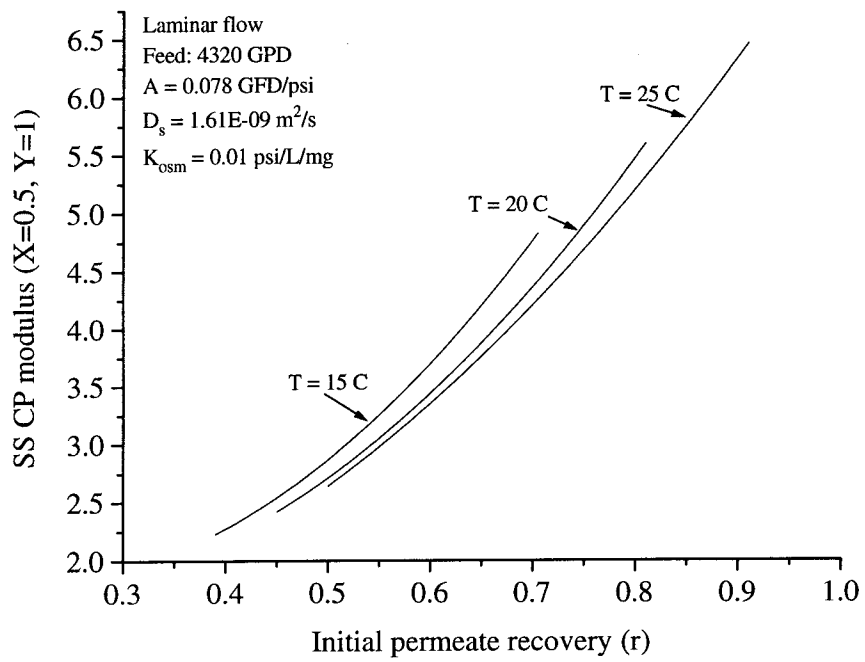


Figure 4.22: Effect of ambient temperature on CP for laminar channel flow.

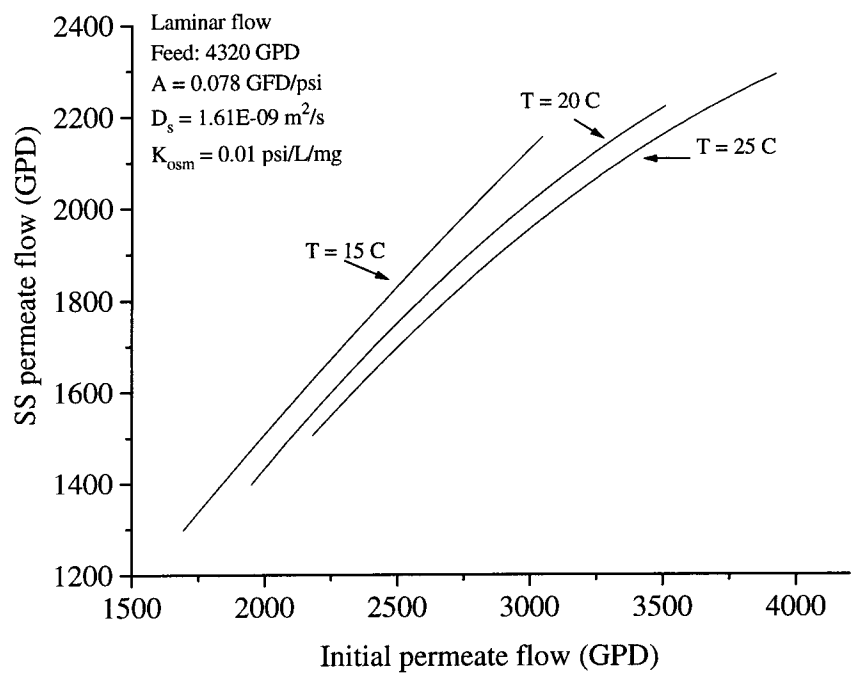


Figure 4.23: Effect of ambient temperature on permeate flux decline.

be higher in real systems leading to greater flux decline than that is shown in the Figure 4.21.

The effect of temperature on CP and flux decline is illustrated in Figures 4.22 and 4.23. Temperature was mainly assumed to influence membrane permeability A and the osmotic pressure coefficient K_{osm} . Since the permeability experiments on the membrane were conducted in the limited range of 15 to 25 °C, the model runs were limited to this range. Nevertheless, increasing temperature had the effect of increasing permeability, and therefore increased CP and flux decline.

4.4.2 Spiral Wound Membranes

The model was also used to generate CP and flux data on spiral wound membranes based on axial velocity profile provided by Miyoshi and co-workers (Equation 76). The main parameter of interest was the eddy viscosity constant m which defined the extent of mixing induced by the spacer. Based on the specifications provided by the manufacturer in this study (Desal Inc., San Diego, CA) on the spacer namely spacer thickness (0.762 mm), cross-bar thickness (0.216 mm) and spacer porosity at approximately 0.9, the constant was calculated to be 8.7 employing Equation 77.

The results on CP and flux decline for various feed solute concentrations are shown in Figures 4.24 and 4.24. Simultaneously, flux decline data for a specific feed concentration (500 mg/L) are compared with laminar and completely mixed flow ($m = 4$) regimes and plotted in Figure 4.26. The laminar flow regime gave the highest CP and flux decline values confirming the need for effective solute mass transfer during membrane

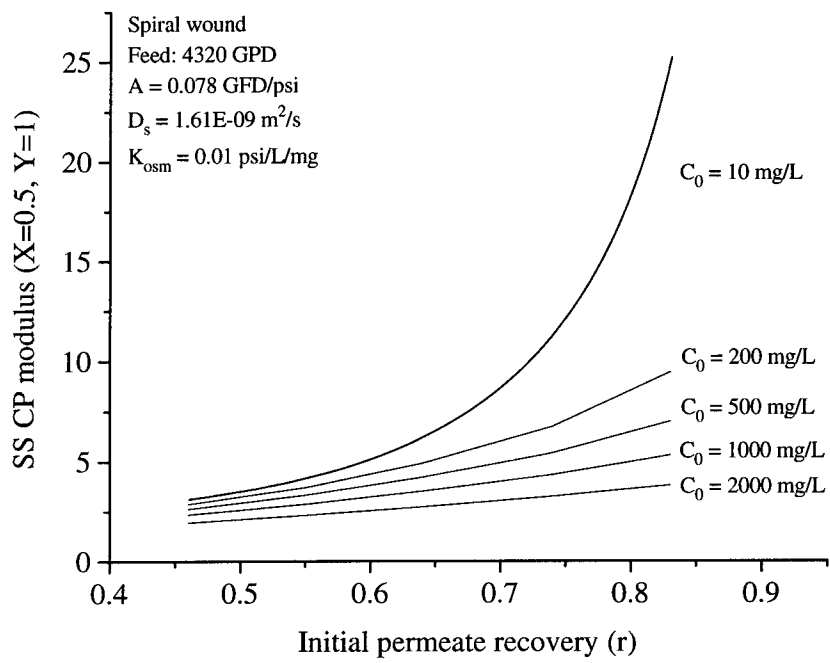


Figure 4.24: Effect of feed solute concentration on CP for spiral wound flow.

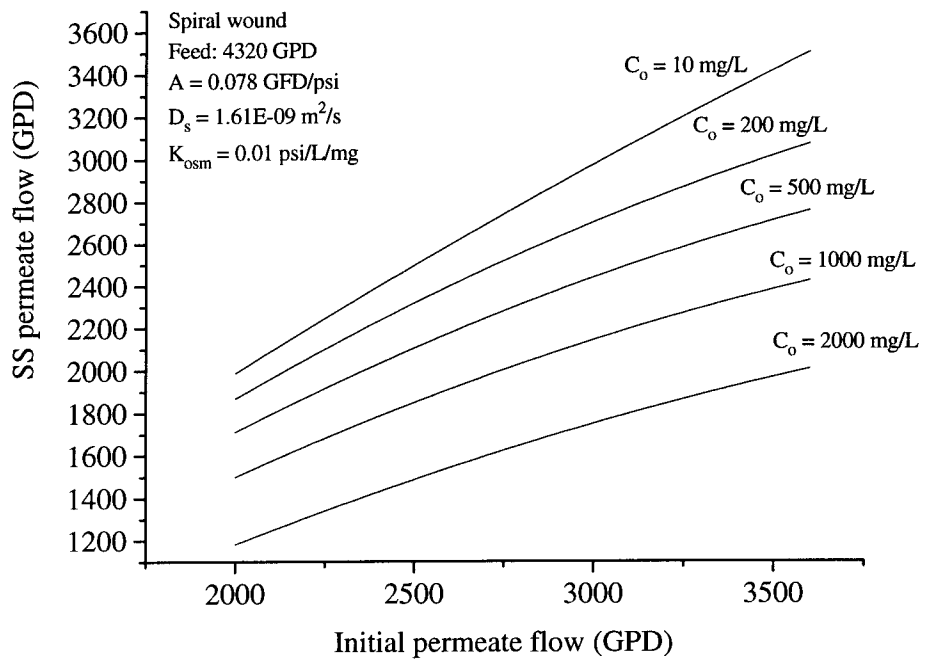


Figure 4.25: Effect of feed solute concentration on permeate flux decline for spiral wound flow.

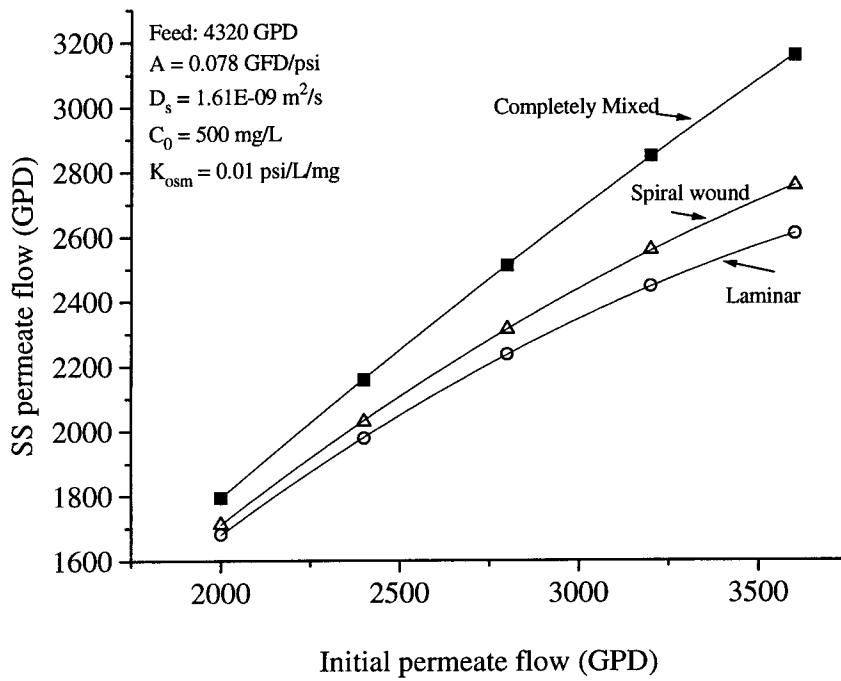


Figure 4.26: Effect of various cross-flow regimes on permeate flux decline.

separation; the presence of the spacer only decreased CP and flux decline but the change was marginal. This result indicates the improvements that are necessary for increasing the effectiveness of the mixers by increasing m ; for instance, decreasing spacer porosity considerably increases m thus insuring adequate mixing.

As in the case of laminar flow, the model was tested to establish the effect of cross-flow velocity by increasing feed flow and recycle ratio; the results were exactly similar to the laminar case. Three feed flow rates at 3, 15 and 30 GPM were used to produce the data; results indicated that increasing feed flow had a direct and considerable impact on reducing CP and permeate flux decline. As in the laminar flow regime case, several recycle rates with recycle ratios ranging from 0.0 to 10 were used to ascertain the effect of recycle on CP; results indicated that higher recycle flow rates (>1) decreased CP and flux decline but not to the same extent as that observed with greater feed flow. Temperature was also used as a parameter to test CP and flux decline in the presence of feed spacers; three temperatures at 15, 20 and 25 °C were used to generate the data. The observed trends on CP modulus and permeate flux decline were identical to the laminar case; the main effect of increasing temperature was found be enhanced permeability and therefore higher CP and flux decline. The model was also used to study the effect of channel half-width H and the degree of mixing; the latter effect was represented by the eddy constant m . The results on permeate flux decline for initial starting recovery of 0.83 are presented in Figure 4.27; five values of H at 20, 25, 30, 35 and 40 mils (1 mil = 0.762 mm), and four values of m at 1, 10, 100 and 1000 were chosen for model runs. The permeate flux decline was lowest for H value of 20 mils and m value of 1000; lower H values essentially increased cross-flow velocity while higher m values represented a greater degree of mixing and turbulence.

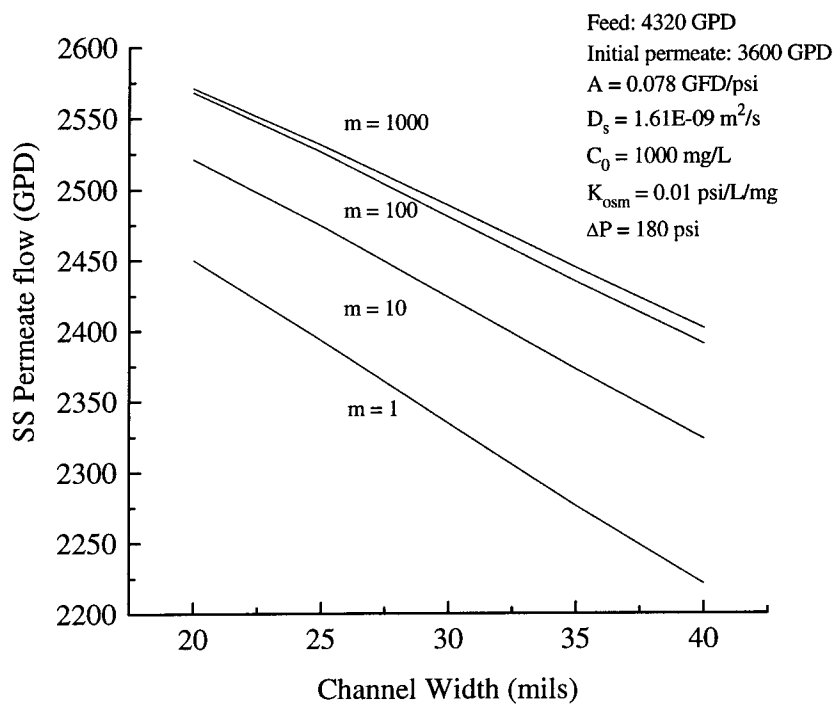


Figure 4.27: Effect of channel width and spacer eddy constant m on permeate flux decline.

4.5 Experimental Verification

Experiments were conducted on the pilot-scale RO system that was constructed for the Lake Arrowhead wastewater reclamation project (See Appendix I). Both transient and steady state results are presented in this section; the experimental data is compared with model runs for all the cases of axial velocity namely laminar flow, completely mixed flow and flow with feed spacers.

Figure 4.28 represents normalized flux decline data for a typical 1 hour experiment conducted on the unit; for the feed flow rates used in these experiments (2 and 3 GPM), the 1 hour test period was approximately 30 times the feed side fluid residence time. This test period was found to be adequate for the permeate flux to decline to a steady state value. The experimental flux values were adjusted for variations in the operating pressure since it varied, though within 10%, over the test period; this procedure aided easy comparison with model results where the operating pressure was assumed to be constant. From Figure 4.27, it can be observed that there is approximately a 10% discrepancy between experimental flux decline and model predictions based on spacer-induced mixing; however, it was lower than the flux decline predicted by completely mixed flow.

This difference is primarily attributed to two factors: (1) numerical error that is normally associated with any FD solution and/or (2) the limitations associated with the description of the eddy constant m . For instance in the latter case, the authors who provided expressions for the axial velocity ignored the effects of drag induced by the

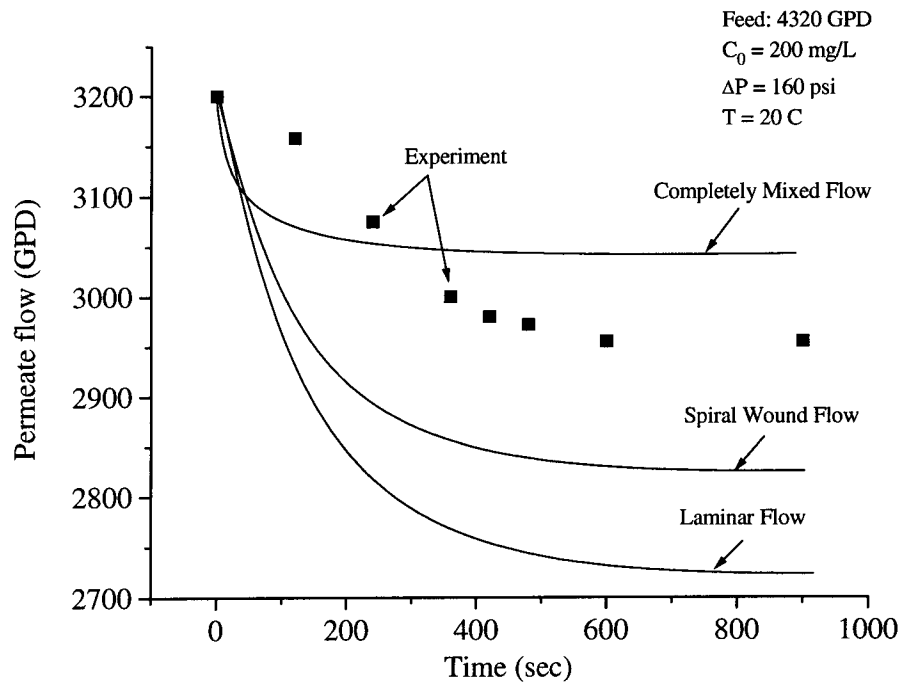


Figure 4.28: Development of CP and flux decline over time: Model results for three flow regimes (laminar, turbulent and spacer induced mixing) are compared with experimental data from a pilot-scale RO unit.

spacer in order to simplify analysis. In addition, empirical expressions were provided for m based on limited experiments conducted on standard spacers.

Another discrepancy between experimental data and model predictions is the rate of development of CP and eventual flux decline; for instance, it can be observed from Figure 4.28 that the flux decline in the case of experimental data is slower as compared to all the three model curves. This discrepancy is attributed to some of the basic assumptions associated with the model namely that the fluid is already at a steady state on the feed side of the membrane before salt is introduced as a step function (i.e., from initial pure solvent to a specific feed concentration). However, this was not observed during the experiments because of the large quantity of pure solvent (water) that was necessary for each experiment. For instance, a typical experimental run consisted of operating the RO unit at a specific permeate recovery initially on 250 gallons of clean water (with an approximate salt concentration of 10 mg/L) in a total recycle mode with both the concentrate and permeate being recycled to the feed tank. The RO unit was then suspended for a brief period of two minutes to mix a predetermined quantity of salt in the feed tank to attain a specific concentration and restarted to conduct the flux decline experiment for that salt concentration. Thus, the procedure automatically insured that there was a delay in the build-up of CP and flux decline associated more with the positive displacement feed pump reaching its operating rpm. This discrepancy was limited to within two to three minutes of operation and did not affect flux decline thereafter. The steady state values of CP modulus and flux decline that depended only on feed and operating conditions such as recovery, feed solute concentration and ambient temperature were also unaffected.

Steady state data were collected from the unit are compared with modeling results for various feed concentrations, operating pressures and recycle flow rates. In general, the modeling results based on spaced on laminar and spacer induced flow regimes consistently over-predicted the flux decline. However, the flux decline based on completely mixed turbulent flow was consistently lower than that observed during the experiments. Some of the steady state results with respect to flux decline are shown in Figures 4.29, 4.30, 4.31 and 4.32 for two feed concentrations (200 mg/L and 1000 mg/L) and flow rates (2880 and 4320 GPD), and two recycle ratios (0.0 and 1.0); the initial and steady state permeate flows from the experiment are plotted along with model predictions. In general, these results are useful in providing an approximate measure of CP and expected flux decline for a given set of operating conditions.

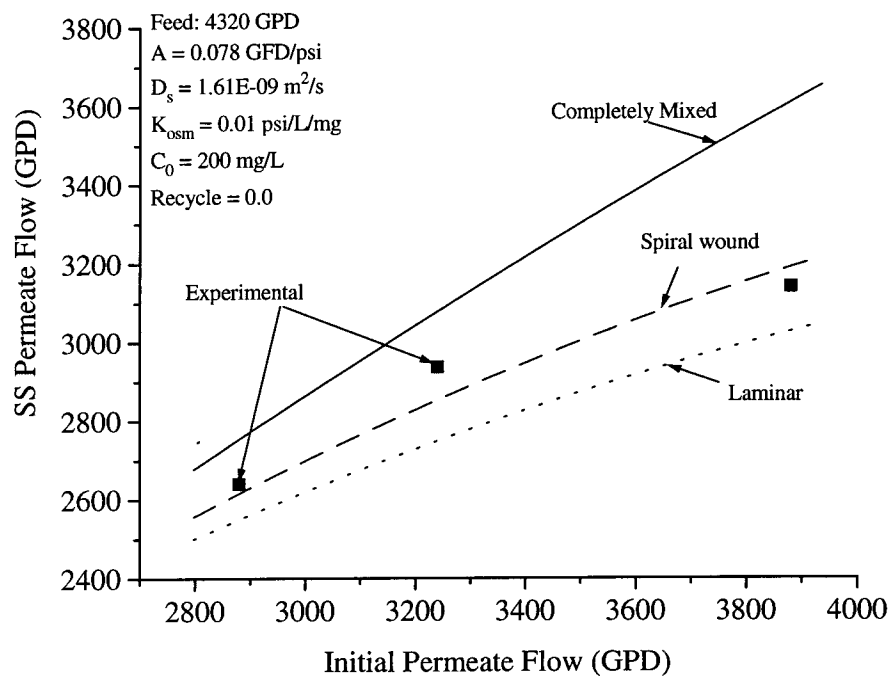


Figure 4.29: Permeate flux decline for a feed concentration of 200 mg/L for various initial recoveries at zero recycle: Model results versus experimental data are depicted.

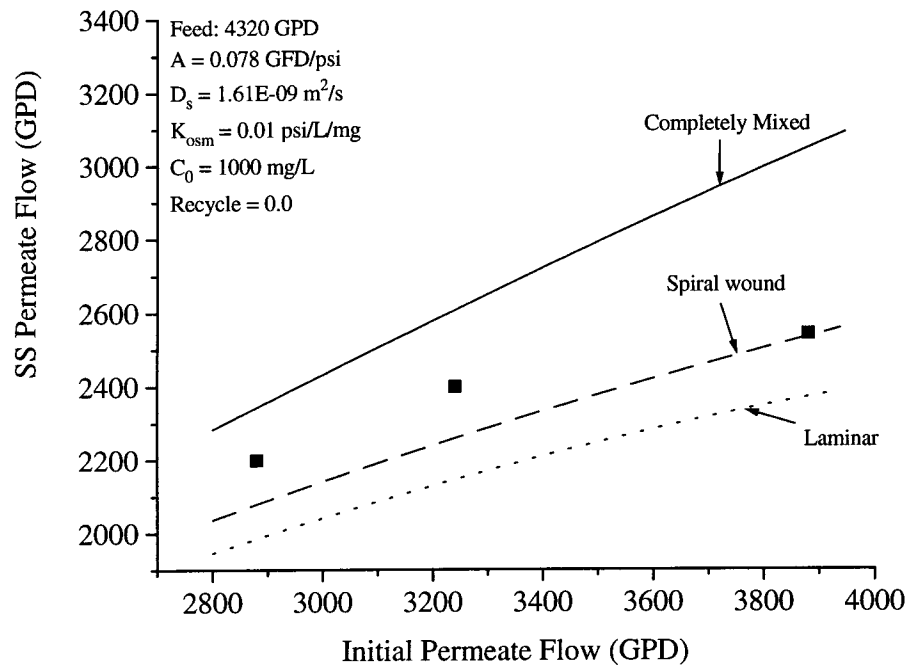


Figure 4.30: Permeate flux decline for a feed concentration of 1000 mg/L for various initial recoveries at zero recycle: Model results versus experimental data are depicted.

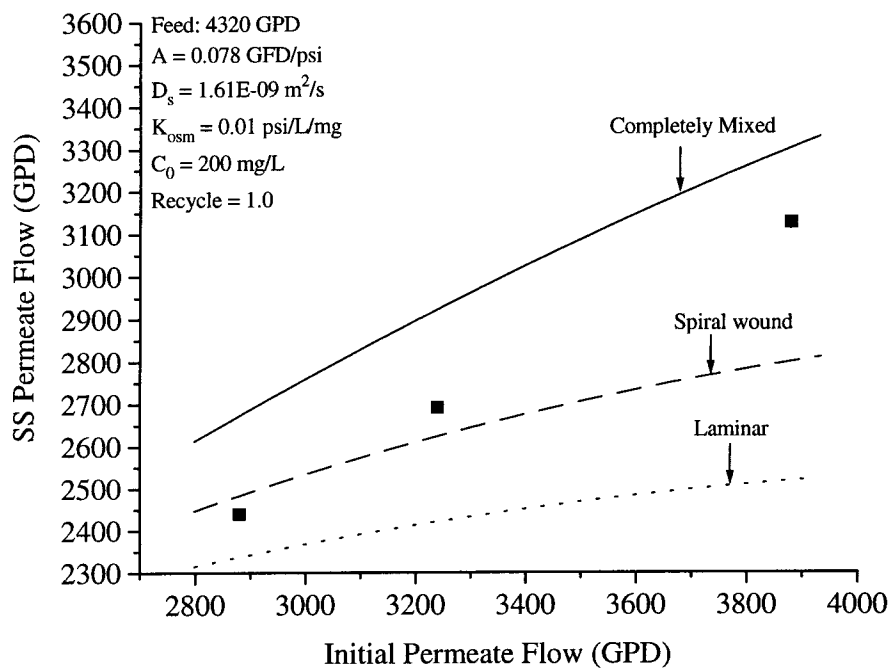


Figure 4.31: Model results versus experimental data for various initial recoveries at a recycle ratio of 1.

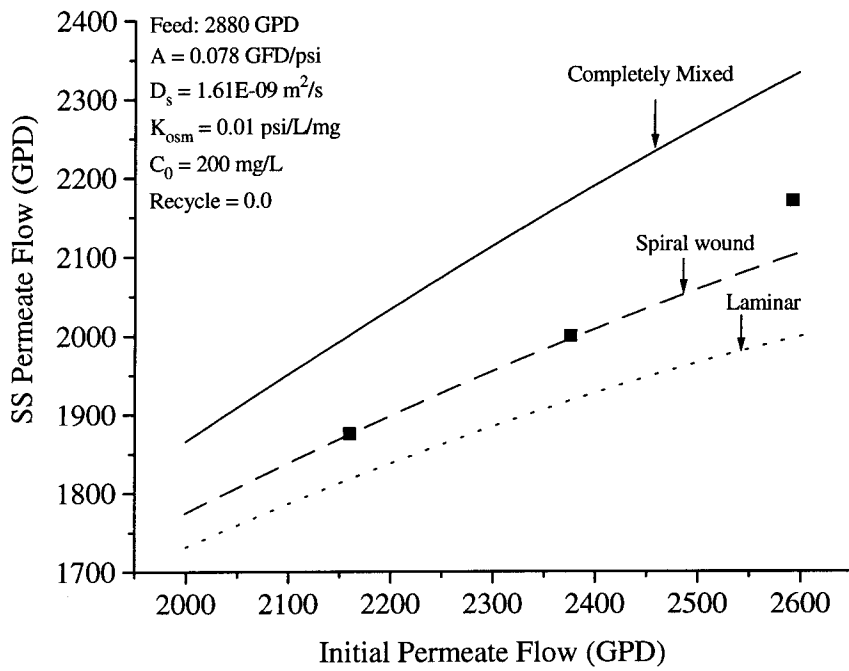


Figure 4.32: Model results versus experimental data for feed flow of 2880 GPD and zero recycle.

CHAPTER 5

SUMMARY AND CONCLUSIONS

Concentration polarization (CP) is a serious problem that has restricted the growth of the membrane industry. Few predictive models exist that predict CP and permeate flux decline in commercial membranes such as the spiral wound module; in addition, all the existing models only address steady state behavior. However, membrane flux decline is a dynamic phenomenon that begins with CP initially and continues over time because of other factors such as fouling, bacterial growth and membrane degradation. It is therefore necessary to develop a comprehensive membrane flux decline model that can include all the above factors.

In this study, a transient state finite difference (FD) model for predicting CP and initial permeate flux decline was developed and tested as a first step towards developing a more comprehensive model for flux decline in commercial membrane systems. A computer program was written to solve the solute mass balance equation along with the equations of fluid balance and continuity; the equations were written for flow in spiral wound membranes with feed spacers but other flow regimes such as laminar flow and completely turbulent flow in rectangular channels were also analyzed. The following are some of the conclusions relating to the model:

1. The model was based on a conditionally stable solution procedure and therefore required careful choice of time and spatial increments; however within the range of

stability, the model was found to be considerably accurate when compared with earlier steady state models based on alternate solution techniques.

2. A wide range of membrane permeabilities, osmotic pressure constant, membrane rejection characteristics and solute diffusivities were studied to ascertain the consistency and behavior of the model. The effect of other important membrane characteristics such as channel thickness, spacer characteristics and temperature were also studied. The effect of cross flow was also studied by varying feed and recycle flow rates.
3. Three different fluid flow regimes were tested including laminar, completely mixed flow and spacer-induced mixing. As expected, the model predicted largest CP and flux decline for laminar flow which is attributed to the absence of effective solute mass transfer near the membrane surface. Completely mixed flow regimes produced the lowest CP and flux decline while the presence of feed spacers produced intermediate CP and flux decline values. For spacers that are used in the commercial RO membranes, the model only predicted marginal decrease in CP and flux decline over laminar flow regimes. This indicated that the spacers needed to be optimized for effective mixing through changes in geometry and alignment.
4. Experiments conducted on a pilot-scale spiral wound RO unit for separation of NaCl solutions at various feed concentrations, feed flow rates, recycle rates compared well with the model; the model consistently over-predicted permeate flux decline by approximately 10%. This was attributed to the limitations of the model including numerical error as well as limitations relating to the description of the membrane, module and the spacers; for instance, several assumptions were made during the formulation of the model such as constant solute rejection, constant axial pressure drop of 10% on all model runs and the absence of spiraling effects.

Nevertheless, the model was successful in accurately predicting the effects of CP and is expected to be useful in the design of commercial membrane systems. The overall formulation of the model is also relatively easy to interpret, and is therefore expected to be useful for separation problems involving colloidal and organic matter removal that are described by other membrane flux models such as the gel polarization model or the resistances model. Another advantage of the model is its relevance to long term flux decline; as each model run reaches steady state with respect to CP, progressively larger time increments could be taken in order to incorporate these effects. Thus, a substantial amount of flux decline information could be generated within reasonable computation times. Some of the important long term flux decline models are reviewed in the second chapter. However, these models need to be tested in conjunction with the above CP model and verified experimentally on a pilot-scale or full-scale spiral wound membrane system.

APPENDIX I

PILOT-SCALE WASTEWATER RECLAMATION AT LAKE ARROWHEAD, CALIFORNIA: AN OVERVIEW

K. Madireddi, R. W. Babcock Jr., B. Levine, T. L. Huo, E. Khan, Q. F. Ye,
J. B. Neethling, I. H. Suffet, and M. K. Stenstrom

ABSTRACT

A demonstration pilot study was conducted in Lake Arrowhead, CA to determine the feasibility of reclaiming municipal secondary effluent for indirect potable reuse and stabilizing the Lake level during periods of extended drought. The Lake, which is the sole drinking water source to the community, was severely impacted during the long drought from 1985 to 1991. A 12,000 liters per day pilot plant was constructed and tested for nearly three years. The pilot plant included denitrification followed by alum coagulation/ flocculation/sedimentation, sand filtration, primary ozonation, granular activated carbon (GAC) filtration, ultrafiltration (UF)/nanofiltration (NF), reverse osmosis (RO) and final ozone disinfection . A comprehensive analytical testing program was devised to monitor product water quality as well as to compare it with the Lake water. Phosphorus and turbidity in the product water were consistently below detection limits (0.02 mg/L and 0.1 NTU respectively). Product water total organic carbon (TOC) and conductivity levels were 1-2 mg/L and 20-40 mmhos/cm respectively, which was approximately 25-50% and 30-50% of the Lake concentration. Challenge testing revealed nearly complete removal of pathogenic material (an approximate 21-22 log removal of bacteriophage and 8-10 log removal of Giardia and Cryptosporidium). Trace organic chemical analysis of volatile and base neutral organic compounds indicated that it is possible to produce reclaimed water that is superior to the Lake water. Only nitrogen (N) removal did not meet expectations for the entire period. It is anticipated that better process control will insure meeting the nitrogen product water goals for full scale treatment.

KEYWORDS: indirect potable reuse, nutrient removal, ozone disinfection, nanofiltration, reverse osmosis.

INTRODUCTION

The drought experienced in Southern California from 1985 to 1991 was one of the longest and most severe, and it is forecast that such extended droughts will continue to sporadically occur. There is an acute need to augment existing drinking water supplies with drought tolerant resources. Importing water from distant sources was previously a popular method, but today it is usually expensive or infeasible. Indirect potable reuse from industrial and municipal wastewater discharges after extensive treatment and subsequent natural treatment and storage, such as groundwater recharge, is an attractive alternative. Technical advances in ozonation, carbon adsorption, and membrane separation processes such as nanofiltration and reverse osmosis, and monitoring technology make this possible.

The concept of potable water reclamation is not technically new. It requires treating a source wastewater to remove all hazardous contaminants such as dissolved organic compounds, bacteria, viruses, nutrients and dissolved salts, that impact reuse. Several full-scale water reuse plants exist such as the Water Factory 21 [Argo, 1979; and McCarty, 1980] in Orange County, California, the Whittier Narrows Groundwater Recharge Project in Los Angeles County, California [Nellor, 1985], the Upper Occoquan Sewage Authority Project in Virginia [Hamann, 1991; National Research Council, 1982; and Water Reuse, 1989], and the Groundwater Recharge Project in El Paso, Texas [Asano, 1985; and Knorr, 1988]; however, public and regulatory agencies remain reluctant to accept reclamation technology for indirect potable water reuse. For this reason pilot-scale projects are used to demonstrate technical and economic feasibility; examples include the Aqua III Total Resource Recovery project in San Diego, California

[Western Consortium, 1992], and the Denver potable reclamation demonstration project in Denver, Colorado [Rogers, 1987]. These projects are also useful in developing technical data bases for regulators, as well as improving water reclamation technologies.

The present project was undertaken to explore indirect potable reuse to provide for additional drinking water supplies in Lake Arrowhead. The community is located in the San Bernardino mountains, 140 km (90 miles) east of Los Angeles in Southern California. Located at an altitude of 1700 m (5500 ft) above sea level, the community was developed around Lake Arrowhead, a 3.0 sq. km (750 acres) man-made recreational reservoir containing upto 5.8×10^7 cu. m (47300 acre-feet) of water. The approximate average depth of the Lake is 19 m (62 ft), when it is full. The population of the community was estimated at 10,000 in 1991, but it has a significant seasonal variation reaching upto 17,000 during summer months. Population growth in recent years has averaged about 10% annually, mainly due to conversions from part-time to full-time occupancy and new residential construction. It is expected that the number of water service connections will increase from approximately 6700, counted in 1991, to 9000 by the year 2010 [Davidson, 1991]. Both sanitation and water services are provided by the Lake Arrowhead Community Services District (LACSD). The long drought from 1985 to 1991 coupled with increasing water demand caused a significant drop in the Lake level, which reached a historic low in 1992. This diminished the recreational value of the Lake, but also seriously questioned the long term sustainability of the Lake as the sole drinking water source. The Community is not a member of the California Water Project, and has no convenience system to the Project's terminus. Even if additional surface water were available, such as the Colorado River water, the cost of a new supply line and pumping would be prohibitively expensive. The Community has no industry or

agriculture, which prevents industrial reuse. Since no other alternative was available, wastewater reclamation was proposed to produce additional water needed to stabilize the Lake level and insure water supply during drought years. It was calculated that reclaiming 50% of the current wastewater flow would add an equivalent of approximately 0.3 m (12 inches) per year, more than enough to offset the recent depletions.

LACSD has two municipal wastewater treatment facilities: the older 3800 m³/day (1.0 million gallons per day - MGD) Willow Creek activated sludge plant, and a new 7600 m³/day (2.0 MGD) Grass Valley trickling-filter treatment plant constructed in 1990. A major portion of the community's wastewater is treated at the Grass Valley plant. The plant has primary treatment, biological trickling filtration which achieves biological oxygen demand (BOD) removal and nitrification, secondary clarification and final disinfection with chlorine. The treated effluent is transported through a single pipe line down the mountains to a local town (Hisperia), where it is used for irrigation. The proposed full-scale reclamation facility would most likely be constructed at the Grass Valley plant. The plant is relatively new and was designed to be expanded to meet anticipated increase in the wastewater flow due to population expansion. The proposed reclamation facility would produce water which would be discharged into Lake Papoose, a small reservoir adjoining Lake Arrowhead, with a volume of 2.5 X 10⁶ cu. m (2000 acre-feet). The water from Lake Papoose can then be allowed to overflow into Lake Arrowhead. The community water supply taken from Lake Arrowhead would close the recycle loop. The existing effluent discharge pipeline could still be used to transport unreclaimed wastewater and brine from the reclamation plant, and act as a bypass to the reclamation facility if any major treatment problems occurred. A schematic of this proposed plan is shown in Figure 1.

Presently, there are no regulatory standards in California for surface water discharge when the receiving body of water is a potable source. The Department of Health Services (DOHS) has historically opposed the discharge of treated wastewaters into such sources. Recognizing this, it was decided to demonstrate that a pilot-scale reclamation plant could produce water equal to or better than the quality of water in the Lake. It was estimated that Lake Papoose with one year of detention time, and Lake Arrowhead with eight years of detention time (assuming 50% reclamation of the present Grass Valley plant flow of 3800 m³/day), would give adequate time for natural treatment of the reclaimed water equivalent or better than present groundwater recharge projects. A recently constructed water treatment plant at Lake Arrowhead (the Bernina drinking water treatment plant) would be the last barrier between the reclamation facility and the distribution system. The plant employs alum coagulation, adsorption clarification, dual media filtration and chlorine disinfection. Even though this proposed project clearly represents indirect reuse with nine years of detention time available between the point of discharge and the intake to the water treatment plant, it is still expected to be highly controversial within the community. The Lake water is of very high quality, and is recharged only from snowmelt and rain. Reclaimed water will be required to meet not only the Federal and State drinking water standards and the special requirements of the DOHS, but also must not degrade the quality of the Lake. After a preliminary review of water quality regulations and from previous reclamation work [Culp, 1980; Hultquist, 1991; SWRB, 1993; and Water Reuse, 1989], the most stringent water quality objectives were devised under four scenarios (Table 1):

1. Match the present water quality in Lake Arrowhead to meet anti-degradation criteria [SWRB, 1968]. These objectives covered a broad range of contaminants, but were especially important for phosphorus and nitrogen.
2. Meet the U.S. Safe Drinking Water Criteria [SDWA, 1986]. These addressed bacteriological and chemical parameters.
3. Meet the Inland Surface Water Plan Criteria [SWRB, 1993]. These were primarily aimed at eliminating toxicity in surface waters, resulting in strict limitations on various compounds, especially heavy metals.
4. Meet the State Reuse Criteria [Hulguist, 1991]. Because no reuse criteria were available for indirect potable reuse, the proposed groundwater recharge criteria were used.

This paper is an overview of the results obtained during the pilot study. It includes general performance data such as the ability of the individual unit processes in the pilot plant to remove specific contaminants, general water quality data on the product water, and a comparison of the product water with the Lake water, treatment objectives and the community's drinking water (Bernina effluent) quality. The comparisons were made for base neutral organics, metals, pathogens and disinfection by-products (DBPs) such as aldehydes and trihalomethanes (THMs). Results of special studies such as microbiological challenge testing, metals removal analysis and ozone disinfection by-products formation analysis are also presented. It is expected that the findings of this pilot study will be used in the eventual design of the full scale reclamation facility or facilities for communities having similar needs. This study differs from the other previously cited demonstration projects in that the product water quality goals were higher because of the Lake's water quality.

EXPERIMENTAL

Pilot plant description

Secondary effluent from the Grass Valley plant was used as the influent to the pilot plant. The main contaminants of interest included nitrogen (mainly present as nitrate) and phosphorus, organics, suspended solids (TSS), metals, pathogens and dissolved solids (TDS). Processes in the pilot plant included denitrification to remove nitrogen, alum coagulation/flocculation/sedimentation to remove phosphorus, suspended solids and turbidity, sand filtration to remove residual phosphorus and turbidity, primary oxidation with ozone to disinfect pathogenic material and simultaneously break down refractory organic matter into more biodegradable organic matter, biological carbon filtration for removal or oxidation of the biodegradable organic matter after ozonation, ultrafiltration (UF)/nanofiltration (NF) as pretreatment for reverse osmosis (RO) to remove dissolved solids (TDS) and total organic carbon (TOC), and final disinfection with ozone (Figure 2).

Two main features of the pilot plant design were the absence of chlorine disinfection altogether and the presence of two membrane filtration steps. Ozone was used instead of chlorine as the primary disinfectant mainly to avoid the formation of chlorine DBPs such as THMs. Ozone was used for its superior oxidation and disinfection capability and its ability to destroy taste and odor (T&O) causing compounds. Accordingly, the existing chlorine contact tanks in the Grass Valley plant were completely bypassed and the secondary clarifier was used as the intake point for the pilot plant. UF or NF was chosen as pretreatment membrane steps for RO to increase the

overall plant removal efficiency, but also to protect RO from fouling due to organic material. Another aspect of design was to provide at least two treatment barriers to all contaminants. For example, phosphorus is removed through alum precipitation and RO, while nitrogen is removed through denitrification and RO.

A tall up-flow fluidized bed denitrification reactor was constructed from a PVC column (5.75 m in height and 0.5 m in diameter) and filled with 2.1 m fine sand (0.6 mm) media for supporting biological growth. The retention time in the reactor ranged from 6 to 8 minutes. Methanol was used to provide additional organic carbon for denitrification; the organic carbon in the trickling filter effluent was too refractory for denitrification. A small aeration tank was placed after the denitrification reactor to strip the nitrogen gas bubbles from the denitrified effluent and simultaneously increase the dissolved oxygen concentration. Provision was also made for a portion of the denitrified effluent to be recycled back into the column. Flow was maintained at 55 liters per minute (LPM) while recycle was varied between 0 and 55 LPM. The expanded media bed depth varied between 2.5 m and 4.2 m depending on the total hydraulic flow.

Alum and a high molecular weight cationic polymer were used as coagulant and flocculant respectively for the clarifier. They were directly injected into the feed and mixing was achieved with stainless steel in-line static mixers. After comprehensive jar testing, alum and the polymer doses were fixed at 60 mg/L and 1.0 mg/L respectively. Alum was chosen as the coagulant because of its ease of handling; it is also used at the Bernina treatment plant. The retention time in the sedimentation tank was approximately 6 hours for a feed flow of 45 LPM. The clarified effluent was further filtered in a pressurized sand filter which utilized fine sand (0.6 mm) as the media. The

media depth was 1.2 m and there was an additional headspace of 1.2 m; this allowed for 100% expansion during filter backwashes. Flow to the filter was maintained at 35 LPM and the filter was automatically backwashed every six hours.

Primary ozone oxidation was achieved in five PVC columns (0.3 m in diameter and 6.0 m high). Oxidation with ozone was intended for two purposes: to achieve the disinfection of pathogenic material, and to break down high molecular weight refractory organic compounds into smaller more biodegradable compounds, which could be metabolized during biological carbon filtration. The ozone columns were operated in a counter current mode. The liquid was pumped into the columns near the top and the ozone gas was fed through the base of the columns. Fine pore ceramic dome diffusers were used to enhance ozone gas transfer. An anti-siphon loop was constructed after the fifth column to ensure a standing column of water in all the columns. An electric spark generator was used to produce ozone from pure oxygen. Inlet gas phase concentrations ranged from 0.5 to 1% of ozone by weight. The retention time in the columns ranged from 20 to 40 minutes depending on feed flow. The ozone dose varied from 10 to 20 mg/L depending on ozone concentration in the feed gas. The ozonated effluent was filtered through a granular activated carbon (GAC) filter. The GAC filter was similar in design to the sand filter, and was filled with approximately 1.2 m of Filtrasorb F-400 GAC (Calgon Corp., Pittsburg, PA); in addition, there was 1.2 m of headspace for 100% bed expansion during backwashes. Flow to the filter was maintained at 20 LPM and the filter was automatically backwashed every 8 hours. The filter was operated in a biological mode to avoid the costs of regenerating or replacing spent media. The filter feed was saturated with dissolved oxygen after oxygen absorption in the ozone columns,

and this provided adequate dissolved oxygen for biological growth with an oxygen residual after GAC filtration.

The effluent from the GAC filter was collected and pumped through the first membrane filtration unit (Figure 3). Table 2 is a description of the main features of the three membranes used in this study. Spiral-wound membranes were used instead of hollow-fiber membranes because of the presence of solids and organics in the feed water and their potential to foul the membrane surface. Fouling affects the performance of the membranes by decreasing the product water throughput and quality. Thin film membranes were used instead of the conventional cellulose acetate membranes; they were expected to run at high permeate recoveries (60-80%) and low operating pressures (100-200 psi). Provision was made for both acid and anti-scalant to be injected into the feed. The entire unit was designed for a total product water flow of 6 to 12 LPM depending on ambient conditions and the quality of the feed water. The product water from the RO unit was pumped through two PVC columns (0.15 m in diameter and 6.1 m high) for final disinfection with ozone. The feed ozone gas was drawn from the same generator which fed gas to the primary ozone columns.

It should be noted that there is a substantial decrease in the design flow between the first and the last unit processes. This was done deliberately to avoid flow control problems in the individual units. All valves were either manually operated ball valves or needle valves, and it was easier operate the plant continuously when the feed tanks were either full or had constant over-flow. This mode of operation would not be used in a full-scale facility. The plant was operated at steady state which would also be used in a full-

scale facility, since only a constant fraction of the total wastewater flow would be recovered.

Analytical Protocol

The key sampling points for individual unit processes are numbered Q1 through Q9 in Figure 2. Field parameters such as pH, turbidity, temperature, alkalinity, dissolved oxygen (DO) and hardness were measured three times a week on grab samples taken directly from sampling ports located on process effluent lines. Sampling was performed on all unit processes, and measurements were performed on-site immediately after sampling. Alkalinity and hardness were measured using the standard titrimetric method while pH, temperature and DO were measured using probes. Turbidity was measured using a Hach Model 2100A turbidimeter. The same grab samples were later analyzed using a Dionex Ion chromatograph (IC) at the University of California, Los Angeles (UCLA) to identify and quantify monovalent and divalent anions such as sulfate, phosphate, nitrate, nitrite, fluoride and chloride [U. S. EPA, 1984]. After December 1994, additional nitrate measurements were made using a nitrate probe. Ammonia and organic nitrogen (TKN) were measured weekly using the probe-method and the standard Kjeldahl method. The TKN measurements were discontinued after September 94. Both field and IC analysis were performed three times a week during regular data collection phase from June 1994 to December 1994, but towards the end of the test program from April 1995 to June 1995, grab samples were collected three times a week and composited before analysis. Metals were analyzed for four consecutive weeks in June 1995 using inductively coupled plasma emission spectroscopy and mass spectrometry (ICP-MS).

TOC measurements were made on a Dohrman DC-80 carbon analyzer. UV absorption at 254 nm measurements were made on a 5652 Hewlett Packard diode array spectrophotometer. Measurements during regular data collection were made on grab samples collected from all the sampling points, but towards the end of the program the samples were composited every week before analysis. Biodegradable dissolved organic carbon (BDOC) analysis was conducted once a week. This procedure quantified the portion of the dissolved organic carbon (DOC) which was biodegradable [Servais, 1989]. The samples were inoculated with seed microorganisms and the change in DOC after a 28 day incubation period was reported as BDOC. The time period of 28 days was chosen based upon laboratory evaluation. Since the carbon filter was operated in a biological mode, this analysis was useful in assessing the filter removal efficiency. The analytical protocol for BDOC is described in detail by Khan (1996).

Base neutral organic analysis were performed using a Finnigan 4000 automated Gas Chromatograph and Mass Spectrometer (GC-MS). The analysis was performed on the extracts from different unit operations, the product water, the Lake water and the drinking water treatment plant effluent, in order to identify and quantify semi-volatile, non-polar organic compounds using an automated form of extraction based upon EPA Method 625 [Longbottom, 1982]. The extractions were performed at the pilot plant and the analysis were performed at UCLA. In general, 10-80 liters of the water sample were extracted with methylene chloride, in a 2 liter per hour continuous liquid-liquid extractor (CLLE) [Baker, 1987], and concentrated to 1 mL for subsequent analysis. With the CLLE, it was possible to identify and quantify the concentrations of contaminants at parts per trillion level instead of parts per billion level. In addition, volatile organic

compounds (VOCs) were analyzed according to the EPA 502.2 procedure employing Purge and Trap, and subsequent GC measurement with a Hall detector. VOC measurements were limited to product water, Lake water and Bernina effluent samples. Aldehyde samples were derivatized with o-(2, 3, 4, 5, 6 - pentafluorobenzyl)-hydroxylamine (PFBHA), and analyzed using a GC with electron capture detection (ECD) [Sclimenti, 1990]. This procedure quantified formaldehyde, acetaldehyde, propanal, butanal, decanal and glyoxal.

Coliform testing was routinely performed (weekly or bi-monthly) on-site using the multiple test tube technique for calculating the most probable number (MPN). Testing was mostly limited to product water samples. Presence/absence indicator tests were also performed on the same samples. Challenge studies were undertaken once during the course of the test program to assess the removal capability of key treatment processes; this included bacteriophage testing on primary and final ozone columns and UF/NF/RO processes, and Giardia and Cryptosporidium testing on UF/NF/RO units.

Chronology of pilot plant operation

The construction of the plant began in July 1992; during this phase, data were collected on the primary phosphorus and nitrogen removal units. Initially, an up-flow direct filter (adsorption clarifier) was tested for a period of about six months to achieve simultaneous phosphorus and turbidity removal. Alum and various high molecular weight polymers were tested to affect removal; however, due to the relatively high volume of sludge production from alum precipitation, filter headlosses accumulated rapidly. This required backwashing the filter at intervals of approximately 15 to 30

minutes. In addition, the precipitating flocs were continually breaking through the filter bed, increasing effluent turbidity and phosphorus concentrations. To improve performance, a conventional clarifier consisting of separate flocculation and sedimentation tanks was assembled and placed on-line in August 1993.

The denitrification reactor was also evaluated during this initial start-up period. During the initial months, the biological growth on the sand media was slow and in order to accelerate growth, biosolids from the Willow Creek activated sludge plant were periodically mixed with the contents of the recycle tank. Initially, the nitrogen bubbles that formed during denitrification affected the performance of the sedimentation tank. The nitrogen bubbles were being trapped within the precipitating flocs and this decreased the floc settlability. To counter the problem, an aeration tank, with a holding time of four minutes, was placed after the denitrification reactor and the denitrified effluent was continuously stripped of nitrogen bubbles. Aerating the denitrified effluent also increased its DO concentration, and prevented anaerobic or anoxic conditions in the sedimentation tank.

Tests were also conducted during this period on the primary ozone columns and the biological carbon filter. This included establishing the BDOC analysis procedure, conducting preliminary UV absorption experiments in order to optimize the primary ozone columns. Experiments were also conducted to assess ozone mass transfer efficiencies and ozone transfer rates; this included setting up a gas and liquid phase measurement apparatus. During the initial phases of the project, there were numerous mechanical problems with the NF/RO processes. The manufacturer's design did not include sufficient vibration control for the positive displacement pumps. Check valves

within the pumps broke and piping connections continuously loosened and leaked. The pump mounting assembly was re-engineered to minimize vibration and the pumps were rebuilt. In addition, all low pressure PVC piping connections were replaced with stainless steel fittings and PVC pipes were replaced with flexible stainless steel hoses, capable of withstanding high pressures and intense vibrations from the pumps. The unit was tested for stable operation for a month prior to intense water quality data collection.

The entire plant was placed on-line in June 1994, and intense data collection proceeded through October 1994. In November 1994, the original NF membranes were replaced with new NF membranes, and the RO membranes were replaced with tighter membranes to enhance nitrogen removal. In addition, a new UF unit was constructed and installed in parallel to the NF unit. The plant was operated till the end of 1994 and shut down briefly during the winter months. Data collection resumed in March 1995 and proceeded until June 1995 during which period, special studies including challenge testing, metals removal analysis, and ozone DBP formation analysis were undertaken.

RESULTS AND DISCUSSION

Basic Water Quality

The important contaminants of interest in the secondary effluent were nutrients phosphorus and nitrogen. It was necessary to remove phosphorus and nitrogen in order to prevent potential eutrophication in the Lake.

Phosphorus. Phosphorus was mainly present as orthophosphate (PO_4^{3-}) in the secondary effluent and averaged 3.2 mg/L. The alum clarifier and the sand filter were operated to remove 60-75 % of the influent phosphorus. Though it was possible to remove more than 90% of incoming phosphorus through precipitation, the clarifier and filter were deliberately operated at lower removal efficiencies to minimize sludge production. Subsequent NF and RO units were used to remove the remaining phosphorus. Figure 3 shows the removal efficiency of the pilot plant for a period of one year. The data are illustrated in two different ways: (1) the monthly average values of secondary effluent and pilot plant product water are plotted in Figure 3a and (2) the log-linear probability distributions of the effluent concentrations from each of the key unit processes is given in Figure 3b. Curves Q1, Q4, Q7 and Q9 represent the exponential fits used to represent concentration data of secondary effluent, sand filter effluent, NF effluent and product water respectively. It was observed that exponential fits were better than linear fits in representing the data; however, curve Q9 which represents product water concentration data, is horizontal because the concentration was consistently below the method detection limit of 0.02 mg/L. In addition, total phosphorus was also measured using ICP emission spectroscopy, when metals testing was performed. Total phosphorus concentration in the product water was always below that of the set objective of 0.1 mg P/L (Table 3).

Nitrogen. The trickling filters present in the Grass Valley plant completely nitrified the ammonia present in the raw wastewater entering the plant; thus nitrogen in the secondary clarifier effluent was mainly present as nitrate. The concentrations of nitrate-nitrogen in the secondary effluent averaged 10.6 mg/L. Because considerable nitrate removal occurred only in the denitrification and RO processes, the monthly average values of

secondary effluent (Q1), denitrification reactor effluent (Q3b) and product water (Q9) are plotted along with average ambient water temperature (Figure 4a). In addition, the log-linear distributions of data for key sampling points are also plotted, as in the case of phosphorus (Figure 4b).

In order to meet the target effluent nitrate-nitrogen concentration of 0.1 mg/L, an overall removal efficiency of 99% was required. It was calculated that this goal could be achieved by 90% removal through the denitrification and the membrane separation processes. A target nitrate -nitrogen concentration of 1.0 mg/L was therefore set as the objective for the denitrification process. It was concluded after the initial testing phase that the denitrification reactor would be successful in removing up to 90% of the incoming nitrate provided that methanol were injected in excess of the stoichiometric dose of 35 mg/L (approximately 45 mg/L). The denitrification column was operated successfully in this mode during 1992-93 [Madireddi, 1994]. However, the excess methanol resulted in higher TOC concentrations in the denitrified effluent. After the intense data collection began on the entire pilot plant, it was noted that the unused methanol present in the denitrified effluent was not efficiently removed by the membrane processes, and resulted in unacceptable TOC concentrations in the final product water. The problem was even more serious during periods of low nitrogen loading to the Grass Valley plant.

In order to counter this problem, the methanol dose to the denitrification reactor was decreased to 30 mg/L which was slightly below the stoichiometric need, during the first month of intense data collection. This consequently decreased the denitrification reactor efficiency, and the overall nitrate removal. In addition, as nitrate-nitrogen

concentration in the pilot plant influent varied significantly (10.6 ± 3.8 mg/L), it was difficult to maintain consistent denitrification with constant methanol dose. For this reason, the effluent nitrate concentrations met the process objective only 30% of the time. Two different RO membranes were tested to increase nitrate removal: the older DESAL SG 4040 membranes which were rated for 80% nitrate removal, and the newer DESAL AG 4040 membranes which were rated for 90% nitrate removal. However, this removal efficiency by itself was not sufficient to meet the product water goal during the study.

Nitrate removal can be improved in a full scale plant by increasing the retention time in the denitrification reactor. The hydraulic retention time in the reactor used in this study was 6 to 8 minutes. A larger denitrification reactor could be used to allow for endogenous denitrification to take place which requires little or no organic carbon addition. It is estimated that doubling the retention time would achieve the nitrate-nitrogen goal of 1.0 mg/L with stoichiometric methanol doses. In addition, process controllers could be used to control the flow of methanol depending on the nitrate concentrations in the secondary effluent. These procedures were not undertaken during the pilot study, but should be included and tested in full-scale design without significantly adding to capital costs. The other forms of nitrogen present in the secondary effluent were ammonia, nitrite and biological nitrogen (TKN). These were present only in trace concentrations and as such were removed during membrane filtration (Table 3).

Conventional. Turbidity, suspended solids (TSS) and dissolved solids (TDS) were also closely monitored. Because of the presence of the clarifier, the sand filter, the biological carbon filter, and the two membrane processes (NF/RO or UF/RO), the removal of these constituents was always well in excess of the set objectives. Turbidity measurements

were performed on all process effluents. The turbidity of the product water and membrane effluent samples (UF, NF and RO) were consistently below the product water goal of 0.2 NTU. TSS measurements were also routinely performed on samples from Q1 to Q6; measurements on membrane effluent and product water samples were discontinued because TSS could not be detected in these samples. Conventional TDS analysis (according to Standard Methods) was not performed, but conductivity measurements were taken for all samples, and these values were used to represent TDS. It was found that the product water conductivity was consistently below the Lake concentration. The removal efficiency with respect to turbidity and conductivity is illustrated in Figures 5a and 5b, and Figures 6a and 6b, respectively.

Total Organic Carbon. In general, it was observed that TOC removal efficiency was high and consistent when NF was operated in series with RO. The product water concentrations were below the goal of 2.0 mg/L for the first six months of the testing phase from July 1994 to December 1994 (Figure 7a). The tighter RO membranes which replaced the older membranes in November 1994 were only marginally superior in removing TOC. The overall TOC removal efficiency was lower from March 1995 to May 1995, when UF was operated in series with RO. This was because a major portion of TOC in the membrane feed water consisted of low molecular weight compounds formed during primary ozone oxidation, and since UF membranes have a relatively high molecular weight cutoff (2500 daltons in this case), these compounds leaked across the membrane processes. Because of this difference in the quality of performance of NF and UF units, the TOC data distribution has been plotted separately for each of these membranes in Figure 7b; the UF permeate and the associated product water concentrations are shown as dotted lines.

The performance of the primary ozonation and biological carbon filtration as a single treatment step depended on the ability of ozone to oxidize refractory organics present in the influent into BDOC, and the ability of the carbon filter to remove the BDOC that is formed as a result of ozonation. UV absorption at 254 nm was used as an approximate indicator of the extent of cleaving of moderate and high molecular double bond organic compounds. It was expected that a portion of the products formed from such cleaving would contribute to BDOC. The data collected during the entire test period indicate that there was an approximate decrease of 35% in UV absorption across the primary ozone columns (0.145 ± 0.034 absorbance units (au) to 0.098 ± 0.032 au). The value further decreased to 0.075 ± 0.024 au after carbon filtration indicating some concurrent removal of refractory organics as well. No UV absorption (at 254 nm) was detected in the RO permeate and the product water indicating a minimal presence of refractory organic matter that can absorb UV light.

BDOC data indicate that there was considerable formation of BDOC during primary ozonation. The concentration values increased from 1.67 ± 0.67 mg/L present in the influent to the primary ozone columns (Q4) to 2.56 ± 0.86 mg/L present in the effluent (Q5e), which is an increase of approximately 55%. The carbon filter was successful in removing a portion of this BDOC; the BDOC in the carbon effluent was 1.18 ± 0.46 mg/L indicating 55% removal. The samples from Q7 which were NF or UF treated, were also measured for BDOC for comparison. No BDOC was detected in the NF permeate, while BDOC concentration in UF permeate was 0.89 ± 0.49 mg/L. This can be attributed to the higher pore size cut-off of the UF membrane (2500 molecular weight). The UF and NF permeate data are further discussed in the section on special studies.

Bacteriological. Bacteriological testing performed on-site revealed the removal of E. Coli and Streptococcus bacteria to below detection limits. Both UF and NF were effective in removing coliforms. Only occasionally (four times during the entire study), it was observed that coliforms were detected in the membrane effluent samples (< 5/100 mL). This was attributed to bacterial growth in the membrane effluent pipes. However, these residual coliforms were completely removed during final ozonation.

A summary of the overall water quality analysis is given in Table 3. It includes average values of the secondary effluent, the product water, and the established product water goal, along with an approximate number of the samples that were collected during the test program. The method detection limits of the instruments that were used, are also given where they are relevant. The values given in this table only reflect the overall removal efficiency of the pilot plant; individual differences of each phase of operation such as the operation of UF or NF, or the effect of replacing the loose RO membranes with tighter RO membranes, have been ignored to conserve presentation.

Special Studies

A series of special studies were performed to quantify various aspects of plant performance. These studies were conducted at specific times during pilot-scale testing for limited periods of upto four weeks.

Base neutral organic analysis. The results of the GC-MS analysis revealed the presence of EPA-625 target compounds such as low molecular weight phthalates, in the extracts of

the Lake water, the drinking water and the pilot plant product water samples (Table 4); however, these compounds were removed by the pilot plant to concentrations less than normally found in the drinking water and Lake water. Phthalates are generally used in the production of plastics and resins and are detected in all waters that have been contacted by things such as plastic caps, pipes, food packaging materials, etc. The compounds detected in the product water at levels indicated in Table 4, are less than drinking water standards. The values reported are presented for comparison, without correction for analytical recovery. A detailed analysis of the GC-MS analysis data along with other aspects of organic carbon removal especially in the biological carbon filter, will be presented in a future paper.

VOCs. VOC analysis performed according to the EPA procedure 502.2, on the Lake water, the drinking water and the pilot plant product water samples are also tabulated (Table 4). As expected, no compounds were detected in the Lake which is a water source that is not contaminated by chlorine treated waters. However, trihalomethanes (THMs) were detected in the drinking water and the pilot plant product water samples. The drinking water sample had a considerably higher total THM level (12 mg/L) than the pilot plant product water (2 mg/L). This was expected because the drinking water treatment plant employed chlorine treatment for disinfection. THMs detected in the product water originate in the raw wastewater coming into the Grass Valley plant. However, the total THM concentration was well below the federal drinking water standard of 100 mg/L, and also lower than the potential of the Lake water to form these compounds (as observed in the drinking water treatment plant).

Ozone disinfection by-products analysis. The analytical method for ozone by-products detected formaldehyde, acetaldehyde, propanal, butanal, decanal and glyoxal. Analysis were performed periodically from August 1994 to June 1995. Product water concentrations are plotted as a function of time (Figure 8a), and the general formation and removal through each of the pilot plant processes is shown in Figure 8b. The main compounds that were detected were formaldehyde, acetaldehyde and glyoxal; formaldehyde formation was primarily attributed to the presence of residual methanol in the water via denitrification, while acetaldehyde and glyoxal were considered to be the by-products formed from the break down of natural organic matter (NOM). The total aldehyde concentration in the product water was less than 10 mg/L. Aldehydes were also detected in the Lake and the drinking water treatment plant samples at approximately similar concentrations (Table 6). However, the concentrations found in both these samples do not reflect their true aldehyde formation potential. Both the Lake water and the drinking water samples were not ozonated and the presence of NOM in these waters considerably increases their aldehyde formation potential. Thus the total aldehyde formation potential of the Lake and the drinking water should be considerably higher than the formation potential of the pilot plant product water.

Challenge testing. In this study, bacteriophage removal was determined on the primary and final ozone columns and the membrane processes. Results are summarized in Table 6 along with the results of *Giardia* and *Cryptosporidium*. Because of the superior oxidation capability of ozone, a greater than 4.0 and 5.1 log removal was observed across the primary and final ozone columns, respectively. In addition, UF and NF were each able to achieve 5.3 and 6.4 log removal, while RO achieved 6.7 log removal. Counting only one pretreatment membrane unit (either UF or NF), a cumulative removal in excess

of 21 log removal was achieved. This does not take into account, the ability of the clarifier, the sand and GAC filters as well as the existing secondary treatment processes in the Grass Valley plant to remove pathogens. The effect of natural purification from detention in Lake Arrowhead and Lake Papoose, as well as removal during drinking water treatment in the Bernina plant was ignored. While no specific regulation is presently available for virus log removal in case of surface water discharge, the required removal for ground water recharge is 7 log removal during treatment [Hultquist, 1991]; the goal was exceeded during this study.

Giardia Lamblia and Cryptosporidium challenge testing were performed only on the membrane processes because of the nature of detection of these two species. The feed to the unit process being challenged was spiked with the inactive seed and the effluent from the process was filtered through a cartridge filter. The number of inactive seed microorganisms present in the filter were counted by a fluorescence assay. Because ozone disinfection is an inactivation process, unlike membrane filtration which is a physical separation process, it was not possible to challenge the ozone columns with Giardia Lamblia and Cryptosporidium using this method. Counting only one membrane pretreatment unit at a time, it was observed that atleast 9.0 and 8.5 log removal with respect to Giardia Lamblia and Cryptosporidium was achieved. This satisfied the treatment goal which was 3 log removal for each of these microorganisms. Cryptosporidium testing was performed using Hydrofluor as the fluorescence reagent; however, the agent also detected all species of Giardia simultaneously not differentiating between Giardia Lamblia and Giardia Muris. Therefore Table 5 shows the removal of both the Giardia species.

Metals removal. Towards the end of the test program, samples were collected from all the sampling points (Q1 to Q9) and analyzed for the presence of metals using AA and ICP spectroscopy. In addition, the Lake water and the Bernina plant effluent samples were also analyzed. Results of the analysis of the product water, the Lake water and the Bernina plant effluent samples are summarized in Table 6. The product water metal concentrations were equal to or below the Lake and Bernina effluent levels; the removal was attributed to the presence of alum clarification, and the two membrane separation units (UF/NF and RO).

Comparison of UF and NF membranes. The main difference in UF and NF membranes is the pore size distribution. NF membranes have a lower pore size cut off (approximately 200 daltons) and are capable of removing a larger range of contaminants. Consequently they offer better pretreatment for RO membranes. However, UF membranes generally having a higher pore size cut off (1000 or more) are expected to operate at lower pressures, and also not be as susceptible to fouling as NF membranes. Both these membranes were tested during this pilot program to compare performance and costs of pretreatment. It was observed that the NF was superior to UF in removing organic and inorganic constituents (di- and tri-valent anions such as sulfate, phosphate, hardness etc.). This was especially important with respect to TOC, which consisted predominantly of low molecular weight compounds after oxidation in primary ozone columns. Product water TOC was higher when UF was operated in series with RO (Figures 8a and 8b); it matched the water quality goal only 75 percent of the time, whereas with NF/RO the product water TOC concentrations were less than the required quality goal 100% of the time. In addition, it was observed that NF was superior in removing bacteriophage and cysts (*Giardia* and *Cryptosporidium*). With respect to

operating data (pressures and flux declines), both NF and UF effluent fluxes (through put per unit area of the membrane) experienced comparable declines (around 40% decline over a period of one week). The RO permeate flux decline for a 4 week period was less than 10% when the feed water was UF treated, and less than 5% when the feed water was NF treated. There is substantial data on operation and maintenance (O&M) of the membrane units, and it will be published in the future; however, it is clear that NF provides 100% protection RO membranes.

Conclusions

A pilot plant was successfully operated in Lake Arrowhead, to demonstrate that indirect potable reuse was possible. The treatment processes included were fluidized bed denitrification, alum coagulation and clarification, sand and carbon filtration, two ozone disinfection units, and two membrane filtration units (UF/NF and RO). Intense data collection was performed for a period of one year; the contaminants of interest were nutrients (phosphorus and nitrogen), dissolved organics, pathogens, and inorganics. Plant performance with respect to these contaminants was consistent and reliable. This was attributed to the concept of multiple barrier treatment achieved during plant operation, by incorporating at least two treatment steps for each contaminant of interest. Special studies including challenge testing, aldehyde analysis and metals testing were also undertaken, and the results indicate the technical feasibility of reuse. Minor problems were encountered with respect to nitrogen removal, but it is anticipated that the problems can be solved by incorporating better control control procedures during full-scale expansion. Detailed cost estimates for a full-scale plant have not been developed; however, the costs for reclamation is less than other alternatives for the Lake Arrowhead

community. This results in part because of the community's geographical location (elevation of 1800 m), the lack of membership in the California State Project, and the cost of transporting secondary treated water out of the basin to Hisperia.

Acknowledgements

Credits. This research was supported in part by the Ahmanson Foundation and additional on-site services were provided by the Lake Arrowhead Community Services District (LACSD). The authors are especially thankful to Mr. Ken Nelsen and his staff at the Grass Valley Wastewater Treatment Plant and Mr. Tim Dohman at the Lake Arrowhead Environmental Monitoring Laboratory for their support. Mr. S. Burke and Mr. J. Langhoff of the UCLA Department of Civil Engineering were instrumental in the construction of the pilot plant. Ms. H. T. Chen, Ms A. Kreibel, and Ms. S. L. Lau of the UCLA Department of Civil Engineering performed some of the water quality control experiments and assisted in the analysis of data. Mr. Ralph Wagner provided valuable guidance and insight through out the project.

Authors. K. Madireddi, T. L. Huo, and E. Khan are Ph. D students in the Department of Civil and Environmental Engineering at the University of California, Los Angeles, CA.

B. Levine and Q. F. Ye are graduate student and research fellow respectively in the Environmental Science and Engineering Program in the School of Public Health at UCLA. R. W. Babcock Jr. was a post doctoral researcher in the Department of Civil and Environmental Engineering at UCLA at the time this work was performed. He is presently an assistant professor in the Department of Civil Engineering at the University

of Hawaii in Honolulu, HI. J. B. Neethling is a principal engineer with HDR Engineering Inc. in El Dorado Hills, CA. I. H. Suffet is a professor in the Environmental Science and Engineering Program in the School of Public Health at UCLA. M. K. Stenstrom is a professor and chair of the Department of Civil and Environmental Engineering at UCLA. Correspondence should be addressed to him at 4173 ENGR I, University of California, Los Angeles, CA 90095.

References

1. Argo, D., and Montes, J. G. (1979) Wastewater Reclamation by Reverse Osmosis. *Journal Water Pollution Control Federation.*, **51**, 590.
2. Asano, T. (1985) Artificial Recharge of Groundwater (Ed), Butterworth Publishers, Boston, MA.
3. Baker, R. J., Gibs, J., Meng, A. K., and Suffet, I. H. (1987) Evaluation of a Teflon Helix Liquid-Liquid Extractor for Concentration of Trace Organics From Water using Methylene Chloride. *Water Research.*, **21**, 179.
4. Culp, G., Wesner, G., Williams, R., and Hughes, M. V. (1980) Wastewater Reuse and Recycling Technology, Noyes Data Corporation, New Jersey.
5. Davidson J. F. Associates. (1991b) Water Master Plan for Lake Arrowhead Community Services District, Lake Arrowhead, CA.
6. Hamann, C., and McEwen, B. (1991) Potable Water Reuse. *Municipal Wastewater Reuse Selected Readings on Water Reuse* EPA 430/09-91-022, Washington D. C.
7. Hultquist, R. H., Sakaji, R. H., and Asano, T. (1991) Proposed California Regulations of Ground Water Recharge with Reclaimed Municipal Wastewater. *Proc. 1991 Specialty Conference in Environmental Engineering*. ASCE, Reno, Nevada.

8. Khan, E., M. K. Stenstrom., R. W. Babcock., and I. H. (Mel) Suffet. (1996) Biodegradable organic carbon for characterizing reclaimed and treated wastewaters, *In Proc. 69th Annual WEF Conf. & Exp.*, Oct 5-9, 1996, Dallas, Texas. Water Environment Federation., Alexandria, VA.
8. Knorr, D. B., Hernandez, J., and Copa, W. M. (1988) Wastewater Treatment and Groundwater Recharge: A Learning Experience at El Paso, Texas, *Proceedings of Water Reuse Symposium IV, Implementing Water Reuse, 211*, AWWA Research Foundation, Denver, CO.
9. Longbottom, J. E., and Lichtenberg, J. J. (1982) Methods for Organic Chemical Analysis of Municipal and Industrial Wastewater, EPA 600/4-82-057, *U. S. Environmental Protection Agency*, U. S. Environmental Monitoring and Support Laboratory, Cincinnati, OH.
10. Madireddi, K., Levine, B; Neethling, J. B., and Stenstrom, M. K. (1994) Nutrient Removal Session: Denitrification in a Fluidized Sand Column: A Lake Arrowhead Pilot Study, *In Proc. 67th Annual WEF Conf. & Exp.*, Oct 15-19, 1994, Chicago, IL. Water Environment Federation., Alexandria, VA.
11. McCarty, P. L., Reinhard, M., Graydon, J., Schreiner, J., Sutherland, K., Evarhart, T., and Argo, D. G. (1980) Advanced Treatment for Wastewater Reclamation at Water Factory 21, Technical Report No. 236 Department of Civil Engineering, Stanford University.
12. Nellor, M. H., Baired, R. B., and Smyth, J. R. (1985) " Health Effects of Indirect Potable Reuse, *Journal American Water Works.*, 77, No.7, 88.
13. Rogers S. E., Peterson, D. L., and Lauer, W. C. (1987) Organic Contaminants Removal for Potable Reuse, *Journal Water Pollution Control Federation.*, 59, 722.

14. Safe Drinking Water Act. (1986) *Amended by the Safe Drinking Water Act Amendment of 1986.*, P.L. 99-339, Approved June 19, 1986.
15. Scilimenti, M. J., Krasner, S. W., Glaze, W. H., & Weinberg, H. S. (1990) Ozone Disinfection By-products: Optimization of the PFBHA Derivatization Method for the Analysis of Aldehydes , In advances in Water Analysis and Treatment, *Proc. 18th Annual AWWA Water Quality Technology Conf.* Nov. 11-15, 1990, San Diego, CA., American Water Works Association., Denver, CO.
16. Servais, P., Anzil, A., Ventresque, C., (1989) Simple Method for Determination of Biodegradable Dissolved Organic Carbon in Water, *Applied and Environmental Microbiology*, **55**, 2732.
17. State Water Resources Control Board (1968) Resolution No. 68-16, *Statement of Policy with respect to Monitoring High Quality of Waters in California..*
18. State Water Resources Control Board (1993) *California Surface Water Plan..*
19. U.S. EPA (1984) Test Method: The Determination of Inorganic Anions in Water by IC- Methods 300.0, EPA- 600/4-84-017. *U.S. Environmental Protection Agency*, Office of Environmental Monitoring, Cincinnati, OH.
20. Total Coliforms. Final Rule (1989) *Federal Register*. 54:124:27544 June 29, 1989.
21. *Water Reuse* (1989) Second edition, Manual of practice SM-3, Water Pollution Control Federation, Alexandria, VA.
22. Western Consortium for Public Health (1992) The City of San Diego Total Resource Recovery Project Health Effects Study, San Diego, CA.

Table 1: Summary of key pilot plant objectives.

Compounds	Goal	Unit	Water Quality Criteria
Inorganic			
TDS	50	mg/L	Lake background level ¹
Nutrients			
Nitrate-N	0.08	mg N/L	Lake background level
Ammonia-N	0.2	mg N/L	Method detection level
TKN	0.2	mg N/L	Method detection level
Ortho-P	0.02	mg P/L	Method detection level
Total-P	0.10	mg P/L	Lake background level
Metals			
Manganese	30	mg/L	Lake background level
Aluminum	40	mg/L	Lake background level
Zinc	270	mg/L	Lake background level
Cadmium	0.5	mg/L	Inland Surface Water ²
Copper	5	mg/L	Inland Surface Water
Lead	0.9	mg/L	Inland Surface Water
Mercury	0.012	mg/L	Inland Surface Water
Bacteriological			
Total Coliform	0	#/100 ml	Total Coliform. Final Rule ³
Fecal Coliform	0	#/100 ml	Total Coliform. Final Rule
Viruses	7	log removal	Groundwater Recharge ⁴
Organics			
TOC	2000	mg/L	Groundwater Recharge
THM	10	mg/L	Lake background level
Other			
Turbidity	0.2	NTU	U. S. Safe Drinking Water
pH	6.5 - 8.5	-	U. S. Drinking Water

¹ Lake Arrowhead Environmental Monitoring Laboratory, Lake Arrowhead, CA.² SWRB (1993); ³ Total Coliform. Final Rule (1989); ⁴ Hultquist (1991)

Table 2: Membranes installed in the ultrafilter, nanofilter and reverse osmosis units.

Item	Ultrafilter	Nanofilter¹	Reverse Osmosis²
Membrane element³			
Model	G 10	DK 4040	SG/AG 4040
Diameter	4"	4"	4"
Length	40"	40"	40"
Number of elements	3	6	3
Configuration	Spiral-wound	Spiral-wound	Spiral-wound
Material	Thin-film	Thin-film	Thin-film
Mol. weight cutoff	2500	200	-
Performance/rejection (% removal)			
Organics Fructose	-	98	-
Humics	-	-	-
TDS	-	-	98.7/99.0
Mg ²⁺	-	-	99.5
SO ₄ ²⁻	-	98	99.5
Na ⁺	-	-	98/99.0
Cl ⁻	-	50	98.8/99.0
Operating pressure	75 - 200	150 - 250	100 - 400

¹NF tested under 100 psi, 1000 mg/L salt and 2% fructose.

²RO tested under 200 psi, 528 mg/L TDS.

³Membrane elements purchased from DESAL Inc, San Diego, CA

Table 3: Contaminant concentrations in the Grass Valley plant secondary effluent and pilot plant product water for the period 1994 - 95.

Parameter	# of samples	Sec. Effl.	Product Water	MDL ¹	Est. Goal	Units
Nutrients						
Nitrate (NO ₃ -N)	85	10.6 ± 3.8	1.0 ± 1.2	0.01	0.1	mg/L
Nitrite (NO ₂ -N)	55	0.2 ± 0.3	< MDL	0.01	0.1	mg/L
Ammonia (as N)	30	1.1 ± 1.6	< MDL	0.2	MDL	mg/L
Organic-N (TKN)	10	2.6 ± 0.7	< MDL	0.2	MDL	mg/L
Ortho-P	55	3.2 ± 0.8	< MDL	0.02	0.02	mg/L
Total-P (ICP)	5	2.9 ± 0.4	0.05 ± 0.02	0.05	0.1	mg/L
Conventional						
pH	105	7.5 ± 0.4	6.3 ± 0.3	-	6.5 - 8.5	-
Alkalinity	75	78 ± 16	7.0 ± 3.0	-	-	mg/L
Hardness	75	90 ± 13	5.0 ± 2.0	-	-	mg/L
Dissolved Oxygen	55	7.0 ± 2.0	> 15	-	-	mg/L
Temperature	105	17 ± 9	17 ± 9	-	-	C
Turbidity	105	6.3 ± 2.8	< MDL	0.1	0.2	NTU
TSS	75	12 ± 6.8	< MDL	0.2	0	mg/L
Bacteriological						
Total Coliform	30	1.1 X 10 ⁶	< 2.2	-	< 2.2	#/100 mL
E. Coli (Fecal)	30	-	< 2.2	-	< 2.2	#/100 mL
Streptococcus	15	-	< 2.2	-	< 2.2	#/100 mL

Table 2: (Cont.d)

Inorganic								
Conductivity	105	350 ± 90	30 ± 20	10	80	mmhos/cm		
Sulfate	70	32 ± 19	0.8 ± 0.7	0.03	1.0-3.0	mg/L		
Chloride	70	46 ± 13	9.6 ± 3.8	0.02	10-15	mg/L		
Flouride	55	0.30 ± 0.05	0.05 ± 0.01	0.015	0.1	mg/L		
Calcium	5	24.2 ± 1.7	0.04 ± 0.02	0.005	15	mg/L		
Magnesium	5	4.4 ± 0.35	0.01 ± 0.008	0.001	2.0	mg/L		
Sodium	5	44 ± 2.1	2.2 ± 0.56	0.030	10	mg/L		
Potassium	5	2.9 ± 0.38	< MDL	0.130	2.0	mg/L		
Organic								
TOC	85	13.0 ± 2.80	0.85 ± 0.62	0.05	2.0	mg/L		
UV abs. at 254 nm	90	.197 ± .052	< MDL	0.002	-	au		

Note: Values are calculated for the entire test period (combined NF and UF readings).

¹ Method detection limit.

Table 4: Base neutral and VOC analysis.

Compound	MDL¹	Product water	Lake water	Drinking water
Base neutral compounds	mg/L	ng/L ²	ng/L	ng/L
Benzoic acid	0.5	< MDL	5.29	36.5
2,4,5-trichlorophenol	2.10	< MDL	< MDL	10.7
1,4-dichlorobenzene	0.084	< MDL	4.53	< MDL
Hexachloroethane	0.167	< MDL	< MDL	5.07
Nitrobenzene	0.66	< MDL	1.42	< MDL
Naphthalene	0.068	< MDL	< MDL	0.96
2-methyl naphthalene	0.125	< MDL	< MDL	0.37
Hexachlorocyclopentadiene	2.43	< MDL	< MDL	6.50
Dimethyl phthalate	0.064	< MDL	< MDL	8.61
Diethyl phthalate	0.060	< MDL	2.46	16.9
Azobenzene	0.063	< MDL	< MDL	0.64
Phenanthrene	0.064	< MDL	< MDL	0.61
Anthracene	0.070	< MDL	< MDL	0.57
Di-n-butyl phthalate	0.060	25.6	366	696
Butylbenzyl phthalate	0.30	< MDL	51.6	6.03
Bis (2-ethylhexyl) phthalate	0.048	0.65	33.7	130
Di-n-octyl phthalate	0.064	< MDL	0.96	0.76
Volatile - EPA Method 502.2	mg/L	mg/L	mg/L	mg/L
Chloroform	0.2	0.79	< MDL	9.05
Bromodichloromethane	0.2	0.7	< MDL	2.93
Dibromochloromethane	0.2	0.5	< MDL	0.33

Note: All samples for base neutral analysis were concentrated by a factor of approximately 76,000.

¹ Method detection limits based on 1.0L samples; ² Nanograms/liter.

Table 5: Summary of challenge testing with Bacteriophage, Giardia, and Cryptosporidium.

Parameter	Primary O ₃	UF	NF	RO	Final O ₃	Total Removal UF/NF
Challenge testing¹						
Bacteriophage	4.0	5.3	6.4	6.7	5.1	log removal 21 / 22
Giardia Lamblia	-	4.1	5.2	4.6	-	8.7 / 9.8
Giardia species ²	-	4.8	5.3	4.4	-	9.2 / 9.7
Cryptosporidium	-	4.3	4.6	4.2	-	8.5 / 8.8

¹Samples were analyzed in BioVir Laboratories Inc., Benica, CA.

²The reagent Hydrofluor which detected Cryptosporidium also detected all species of Giardia, not differentiating Giardia Lamblia and Giardia Muris.

Table 6: Summary of results of aldehydes and metals testing.

Parameter	approximate # of samples	MDL ¹	Product water	Lake water	Bernina effl.
Aldehydes					
Formaldehyde	10	mg/L 1.0	mg/L 3.6 ± 0.9	mg/L 3.0 ± 4.0	mg/L 3.4 ± 1.1
Acetaldehyde	10	-	3.0 ± 2.0	2.3 ± 1.0	12 ± 11
Propanal	10	-	< MDL	< MDL	< MDL
Butanal	10	-	< MDL	< MDL	< MDL
Decanal	10	1.0	< MDL	< MDL	< MDL
Glyoxal	10	1.0	1.6 ± 1.5	< MDL	< MDL
Metals					
Aluminum (Al)	4	mg/L 19	mg/L < MDL	mg/L 33 ± 12	mg/L 49 ± 9
Arsenic (As)	4	6.0	< MDL	< MDL	< MDL
Cadmium (Cd)	4	1.0	1.0	1.0	1.0
Chromium (Cr)	4	1.0	1.0	2.0 ± 1.0	2.0 ± 1.0
Copper (Cu)	4	2.0	< MDL	2.0 ± 1.0	< MDL
Iron (Fe)	4	1.0	1.0	43 ± 40	1.0
Lead (Pb)	4	5.0	< MDL	< MDL	< MDL
Manganese (Mn)	4	1.0	1.0	20 ± 10	1.0
Selenium (Se)	4	5.0	< MDL	< MDL	< MDL
Silver (Ag)	4	1.0	2 ± 1	2.0 ± 1.0	2.0 ± 1.0
Zinc	4	1.0	1.0	430 ± 400	340 ± 60

¹ Method detection limit.

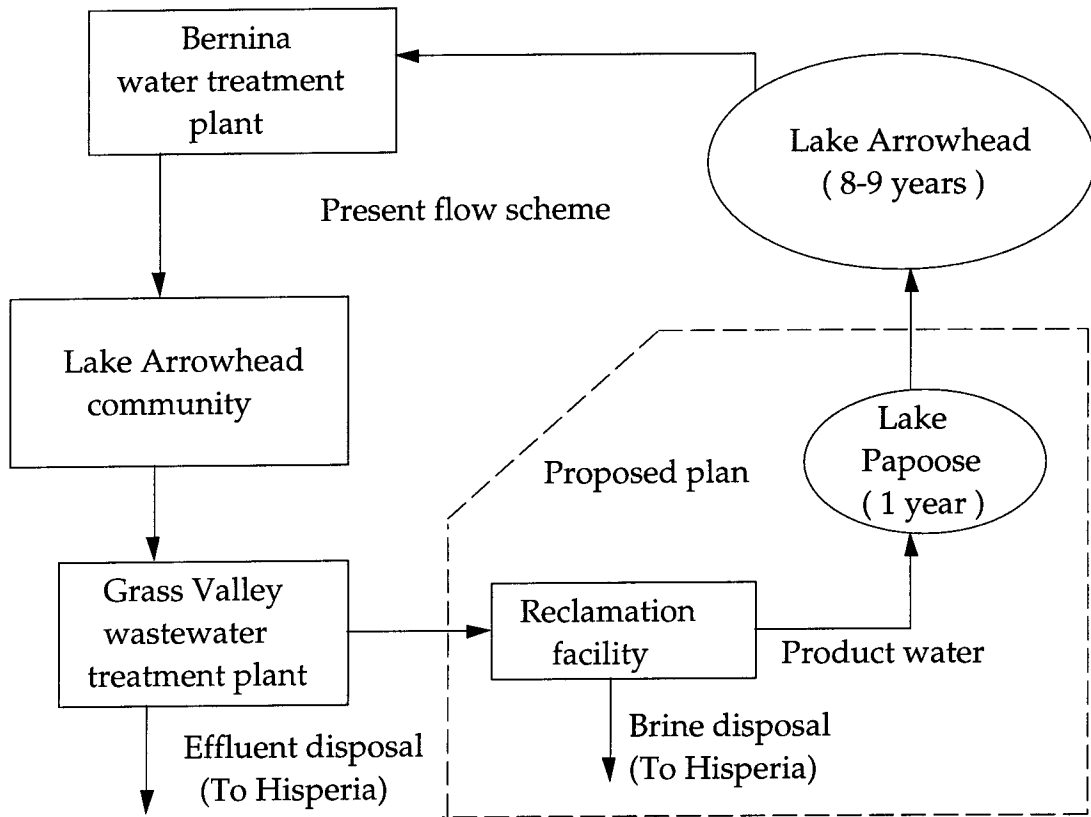


Figure 1. Proposed plan for the Lake Arrowhead reclamation project.

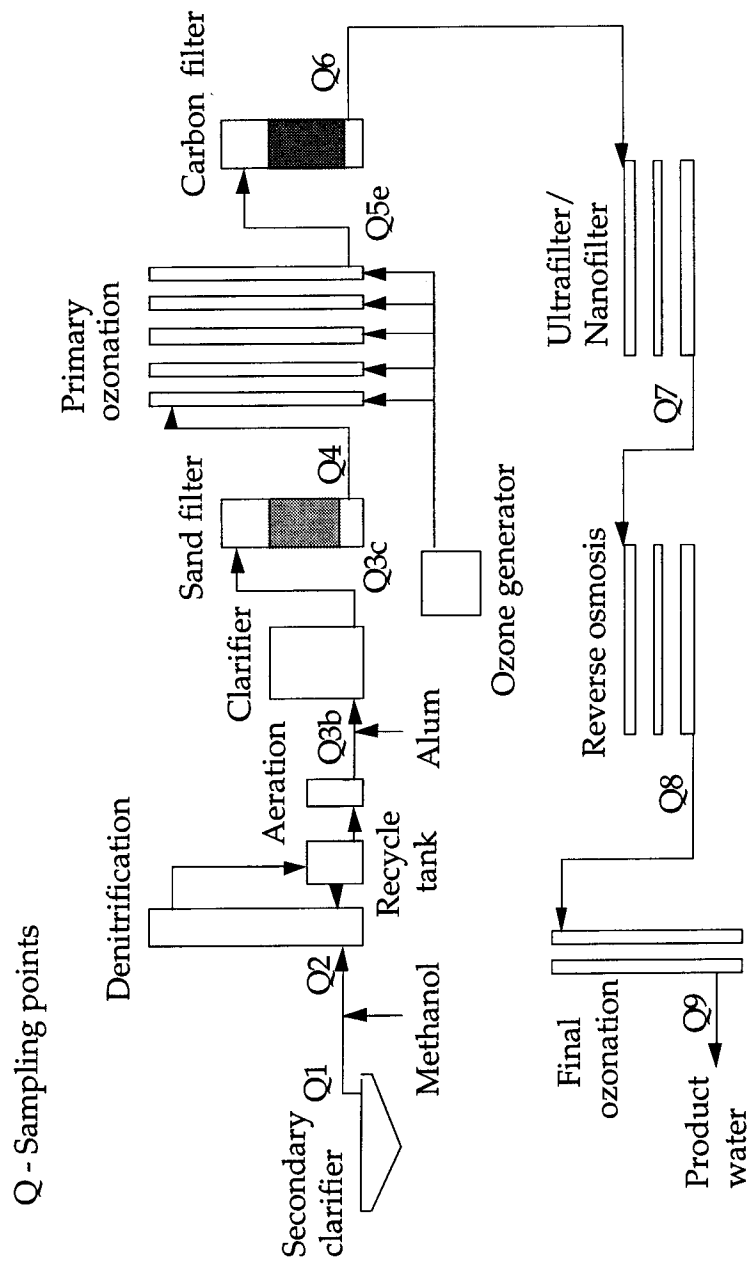


Figure 2. Lake Arrowhead pilot plant flow schematic.

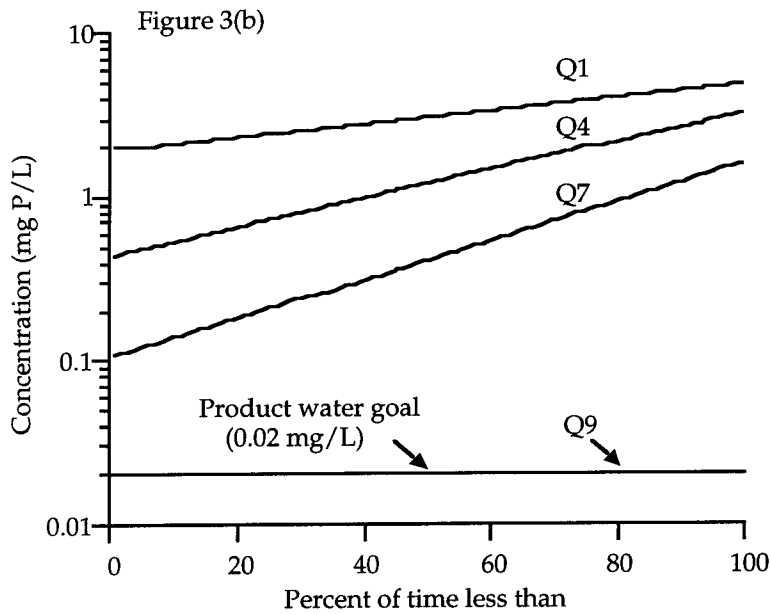
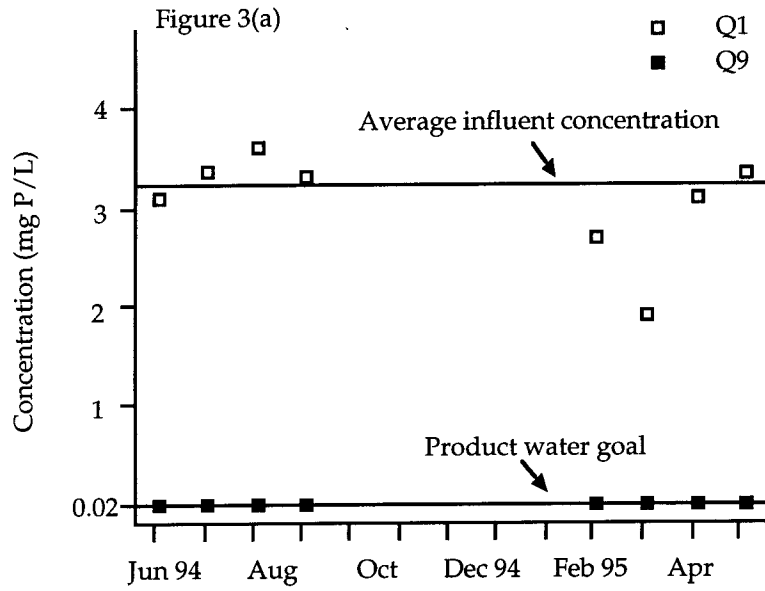


Figure 3. Phosphorus removal for the period 1994-95: (a) monthly average influent and product water P concentrations (b) log-linear data distribution fits for key sampling points.

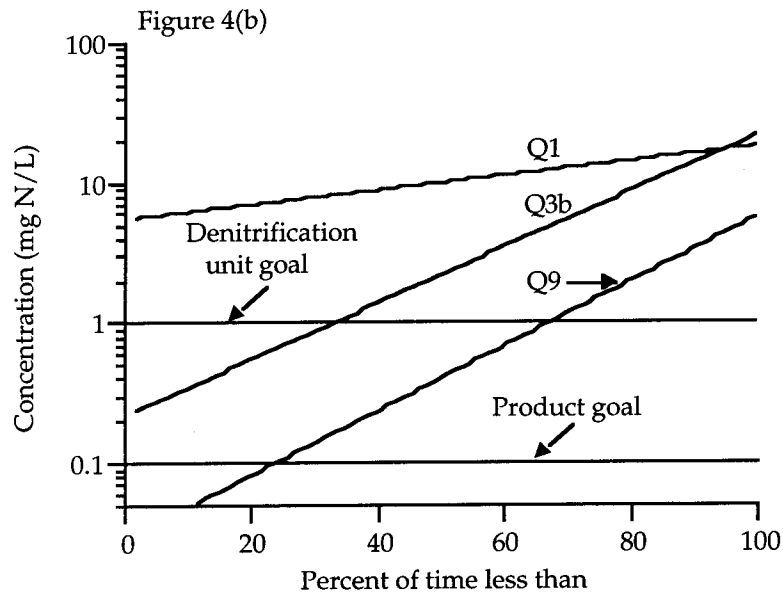
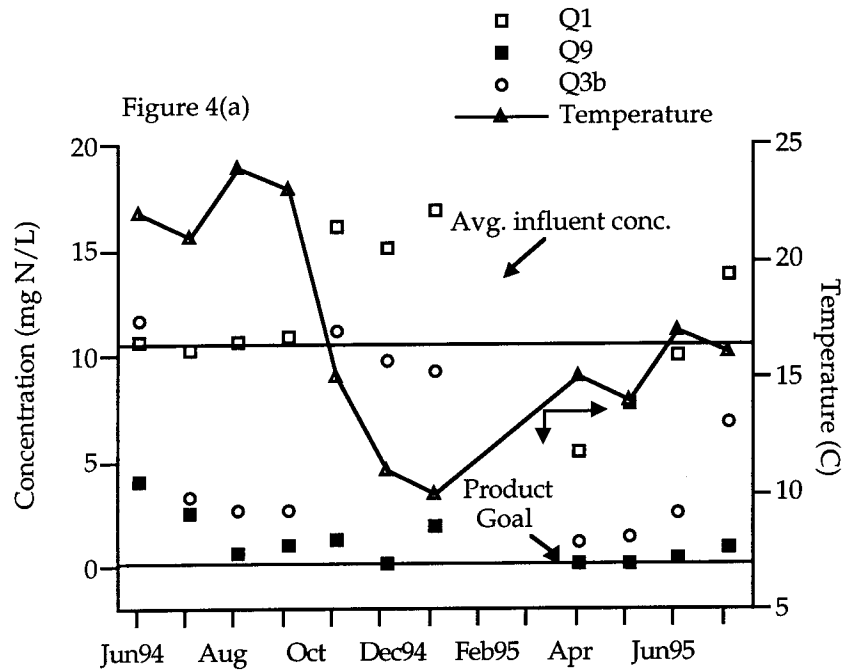


Figure 4. Nitrate removal for the period 1994-95: (a) monthly average influent, denitrified effluent, and product water nitrate concentrations along with ambient water temperature (b) log-linear data distribution fits for key sampling points.

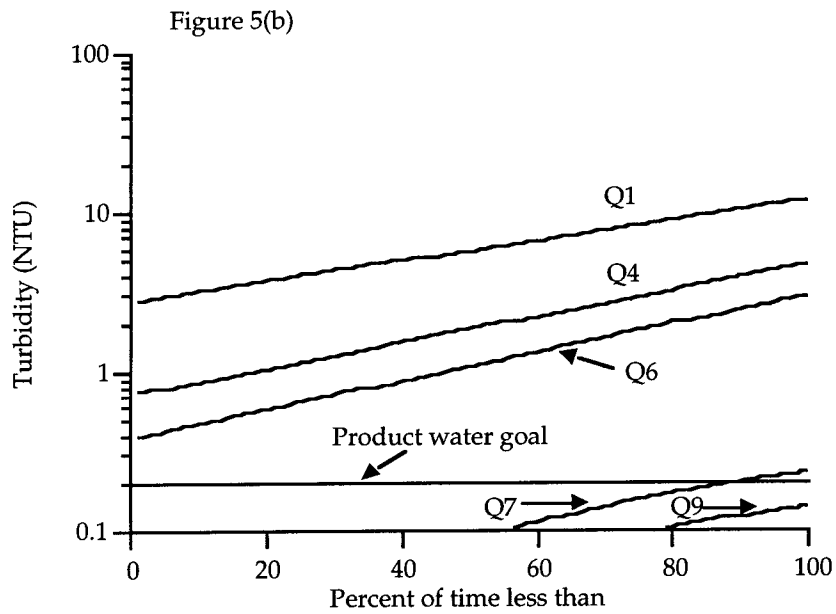
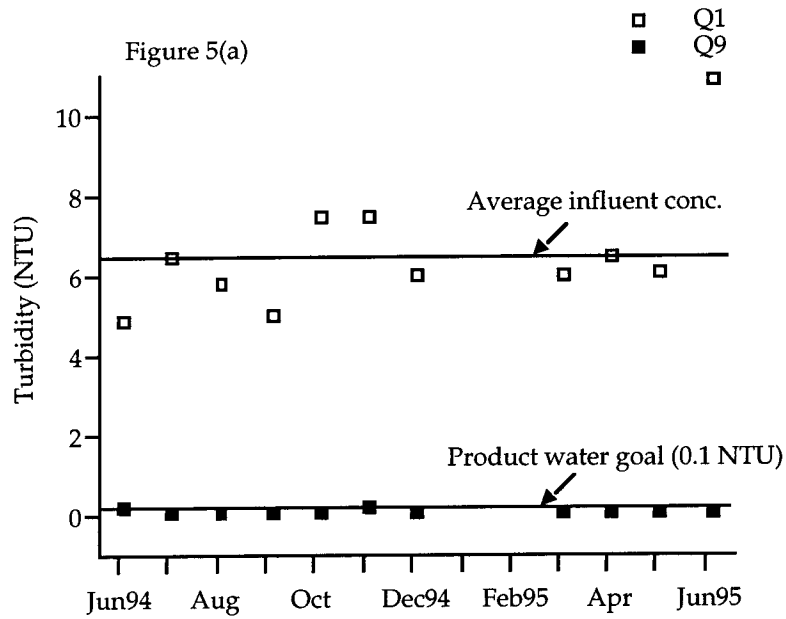


Figure 5. Turbidity removal for the period 1994-95: (a) monthly average influent and product water turbidities (b) log-linear data distribution fits for key sampling points.

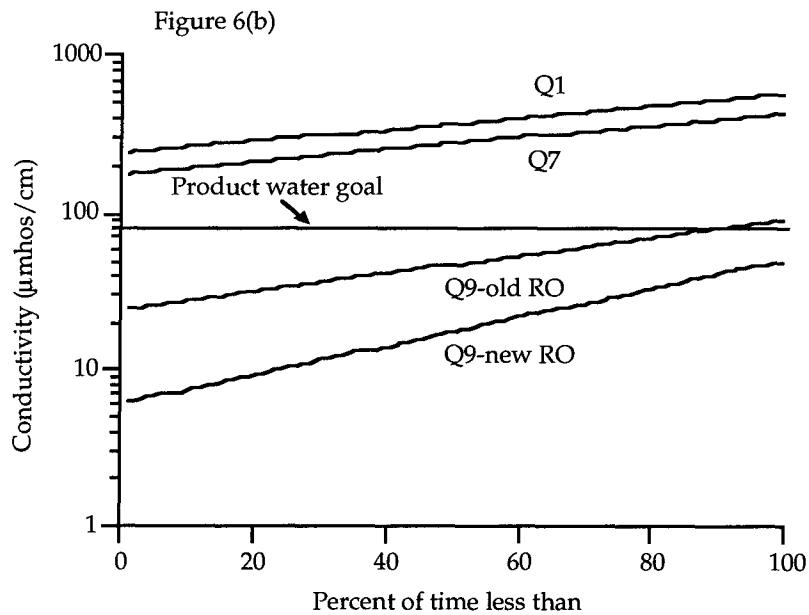
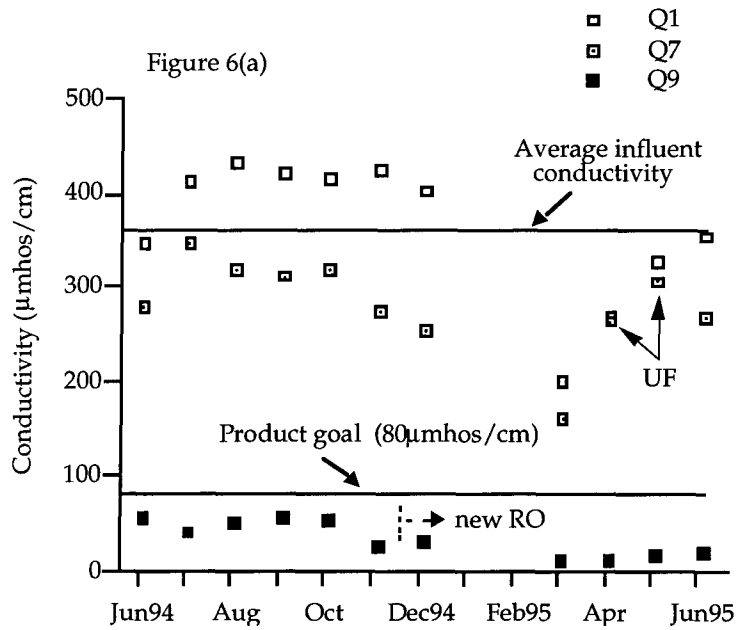


Figure 6. Conductivity removal for the period 1994-95: (a) monthly average influent, UF/NF permeate and product water concentrations - data marked UF represents UF/RO runs (b) log-linear data distribution fits for key sampling points - data collected from old and new RO membranes are plotted separately.

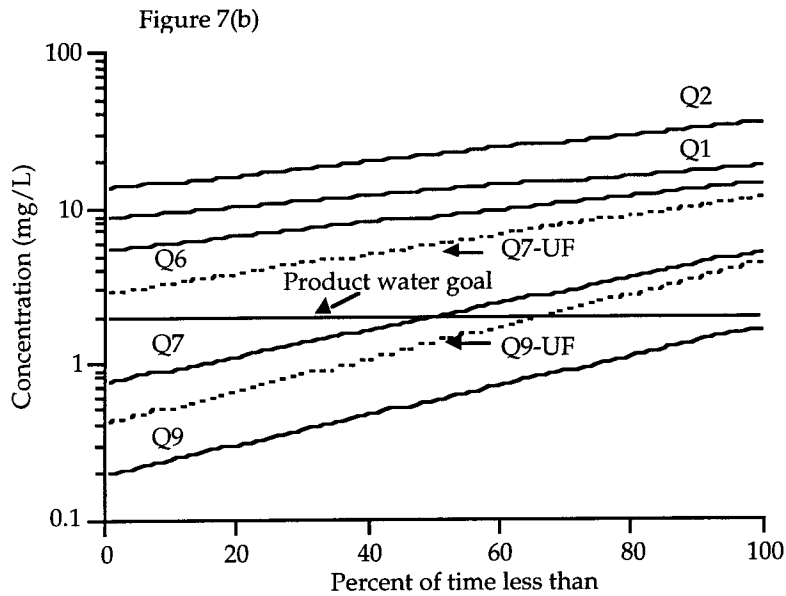
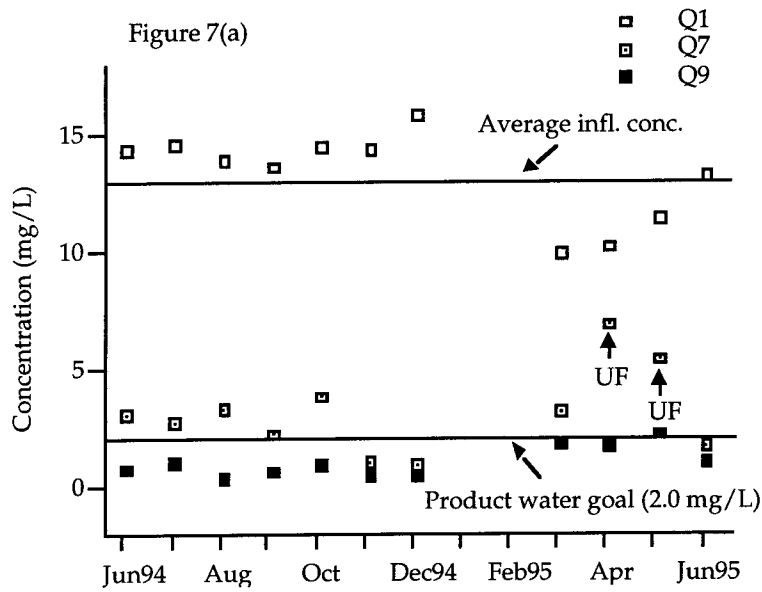


Figure 7. TOC removal for the period 1994-95: (a) monthly average influent, UF/NF permeate, and product water concentrations - data marked UF represents UF/RO runs (b) log-linear data distribution fits for key sampling points - dotted lines represent data collected when UF was operated.

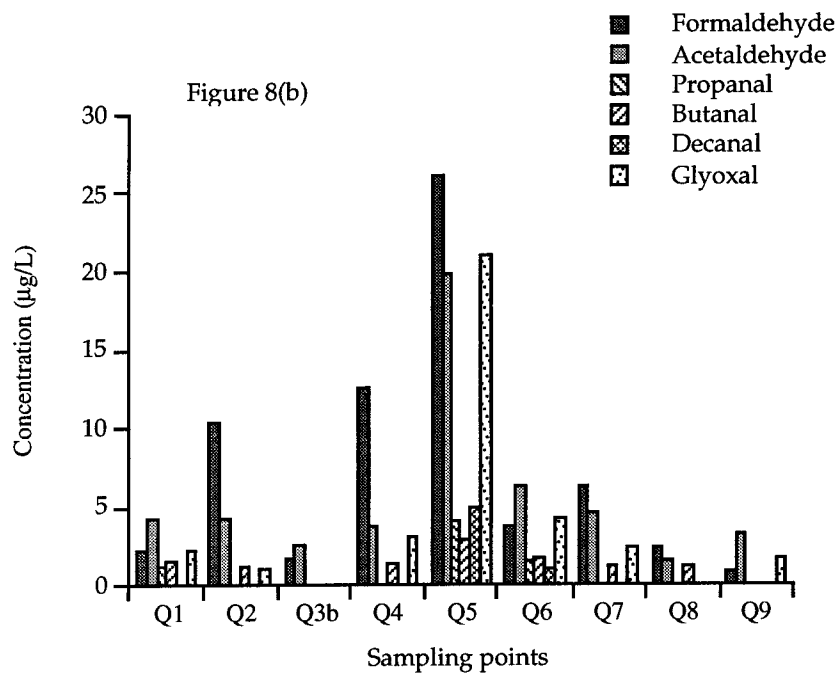
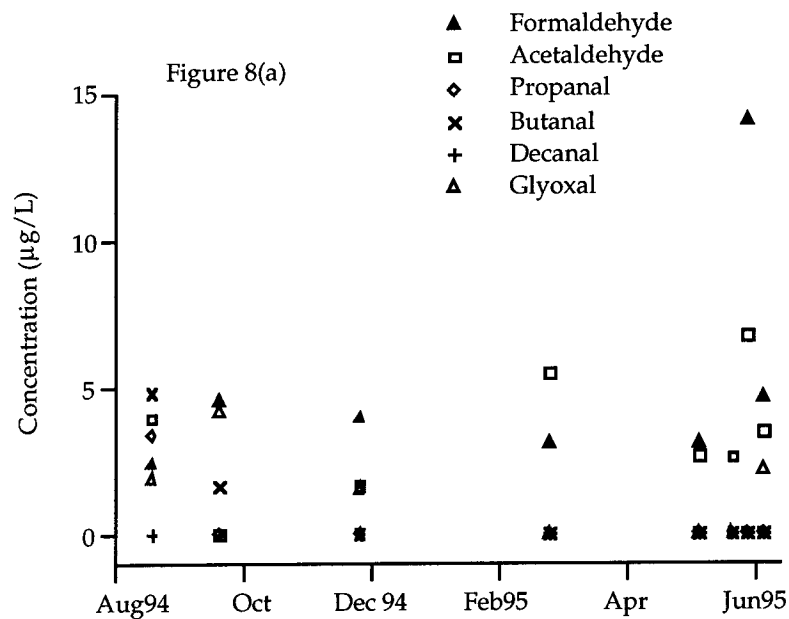


Figure 8. Aldehyde removal for the period 1994-95: (a) monthly average product water concentration of aldehydes as a function of time; (b) overall formation and removal of individual aldehydes through each of the pilot plant processes for 1994-95.

APPENDIX II

```
program recycle
c u = f(x,y); valid for large recoveries
c general comments
c membrane is divided into axial sections and each section
c is scaled separately, and solved numerically.
c scaling means to non-dimensionalize
c format numbers start from 100
c go to labels start with 1000
c do loop labels start from 200
c *****
c all real variables
double precision P(2001,10),pi(2001,10),sum(10),realdt
double precision cinit,unit(10),H,Ar,L,LP,Df(10),Kosm
double precision Q0,Qp(10),voinit(10),Ap,P0,delP,Diff,vw0
c all non-dimensional variables
double precision co(2001,0:52,10),cn(2001,0:52,10)
double precision vn(2001,51,10),vo(2001,51,10),vavg(51,10)
double precision x(2001,10),y(51,10),sol(51),uavg(51,10)
double precision a(51),b(51),c(51),d(51)
double precision d1(51),d2(51),d3(51),Qptot
double precision delx,dely,delt(10),vninit(10),uin
double precision unavg(2001,10),uoavg(2001,10)
double precision realtime,uo(2001,51,10),un(2001,51,10)
integer i,j,n1,n2,n,ir,jr,kr,nmax
c input/output follows
open(2,file='cspi1')
open(3,file='fsp1')
open(4,file='inputdatrpr1')
call inputpr3(Q0,Ar,Ap,Diff,Kosm,L,H,cinit,uin)
c *****
c Rejection Coefficient
Rej = 0.98
c entire recycle ratio
print*,'enter recycle ratio R'
c input data
read(4,105)R
105 format(f5.3)
c divide entire membrane system into sections
write(6,*)'Enter number of sections the unit is to be divided.'
write(6,*)'This is only for calculation purposes.'
```

```

    read(4,100)kr
c   divide membrane length-wise and area-wise
    LP = L/real(kr)
    ArP = Ar/real(kr)
c   *****
c   initialize time and concentrate concentration
    realtime = 0.0
    n = 1
    concentrate = 0.0
    concent = 0.0
c   *****
c   the program will allow for numerical grids to be developed
c   uniformly.
    print*,'number of iterations (enter an integer)'
c   input data
    read(4,100)nmax
100 format(i8)
c   *****
c   input grid information
    print*,'enter number of y-grid points for each section'
    read(4,100)jr
    print*,'enter number of x-grid points for each section'
    read(4,100)ir
c   enter pressure information
c   enter time increments information
    print*,'enter a value for time increment'
c   increment delT will be scaled based on section I
c   the real time increment realdt will be calculated from delT
c   input data
    read(4,110)delt(1)
110 format(f5.4)
c   *****
c   start pressure loop
c   pressure in psi
    P0 = 100.0
c   convert psi to KPa
999 counter = 1
    P0 = P0*6.8947
    delP = 0.1*P0
    vw0 = Ap*(P0-delP/2.)
c   *****
c   evaluate initial cross flow velocities at section inlets
    uinit(1) = uin*(1+R)

```

```

    if(kr.gt.1) then
    do 200 k = 2,kr
200  uinit(k) = uinit(k-1)-vw0*LP/H
    endif
c  *****
c  calculate real time increment
    realdt = delt(1)*LP/uinit(1)
c  calculate delt for all other section keeping realdt constant
c  this is to ensure that permeate flows are calculated
c  across the entire membrane unit uniformly in real time.
    if (kr.gt.1) then
    do 205 k = 2,kr
205  delt(k) = realdt*uinit(k)/LP
    endif
c  *****
c  evaluate and scale vw0(1) and Df(1)
    voinit(1) = vw0*LP/(uinit(1)*H)
    Df(1) = Diff*LP/(uinit(1)*H**2)
c  develop grids for section I
    delx = 1.0/real(ir-1)
    dely = 1.0/real(jr-1)
    x(1,1) = 0.0
    do 210 i = 2,ir
210  x(i,1) = x(i-1,1)+delx
    y(1,1) = 0.0
    do 215 j = 2,jr
215  y(j,1) = y(j-1,1)+dely
c  enter pressure information
    P(1,1) = P0
    do 220 i = 2,ir
220  P(i,1) = P(i-1,1)-delP*delx/kr
c  initial flow and concentration conditions for section I
    uoavg(1,1) = 1.0
    do 225 j = 1,jr
    uo(1,j,1) = uoavg(1,1)*0.095*(9.7*log(9.7-8.7*y(j,1))
    &+8.7*y(j,1)-8.7)
    vo(1,j,1) = voinit(1)*y(j,1)*(3.0-y(j,1)**2)/2.0
    co(1,j,1) = 0.0
225  continue
    do 230 i = 2,ir
    uoavg(i,1) = uoavg(i-1,1)-voinit(1)*delx
    do 235 j = 1,jr
    uo(i,j,1) = uoavg(i,1)*0.095*(9.7*log(9.7-8.7*y(j,1))

```

```

&+8.7*y(j,1)-8.7)
  vo(i,j,1) = voinit(1)*y(j,1)*(3.0-y(j,1)**2)/2.0
  co(i,j,1) = 0.0
235 continue
230 continue
c  y-boundary conditions
  do 240 i = 1,ir
    co(1,0,1) = co(1,2,1)
    co(1,jr+1,1) = co(i,jr-1,1)
240 continue
  if(kr.eq.1) then
    write(2,140)n,realtime,(co(i,jr,1),i=1,ir,20)
    Qptot = 2.0*Arp*vw0*22.825E06
    write(3,150)n,realtime,Qptot,concentrate
  endif
c  *****
c  section loop begins
  if(kr.gt.1) then
    do 245 k = 2,kr
c  evaluate and scale vw0(k) and Df(k)
      voinit(k) = vw0*LP/(uinit(k)*H)
      Df(k) = Diff*LP/(uinit(k)*H**2)
c  *****
c  develop grids
      delx = 1.0/real(ir-1)
      dely = 1.0/real(jr-1)
      x(1,k) = 0.0
      do 250 i = 2,ir
250 x(i,k) = x(i-1,k) + delx
        y(1,k) = 0.0
        do 255 j = 2,jr
255 y(j,k) = y(j-1,k)+dely
c  *****
c  enter pressure information
      P(1,k) = P0-delP*(k-1)/kr
      do 260 i = 2,ir
260 P(i,k) = P(1,k)-(delP/kr)*x(i,k)
c  *****
c  section-wise initial flow and concentration conditions
      uoavg(1,k) = 1.0
      do 265 j = 1,jr
        uo(1,j,k) = uoavg(1,k)*0.095*(9.7*log(9.7-8.7*y(j,k))
&+8.7*y(j,k)-8.7)

```

```

vo(1,j,k) = voinit(k)*y(j,k)*(3.0-y(j,k)**2)/2.0
co(1,j,k) = 0.0
265 continue
do 270 i = 2,ir
uoavg(i,k) = uoavg(i-1,k)-voinit(k)*delx
do 270 j = 1,jr
uo(i,j,k) = uoavg(i,k)*0.095*(9.7*log(9.7-8.7*y(j,k))
&+8.7*y(j,k)-8.7)
vo(i,j,k) = voinit(k)*y(j,k)*(3.0-y(j,k)**2)/2.0
co(i,j,k) = 0.0
270 continue
c first y-boundary conditions at x = 0.0
co(1,0,k) = co(1,2,k)
co(1,jr+1,k) = co(1,jr-1,k)+2.0*dely*vo(1,jr,k)*co(1,jr,k)
&*Rej/Df(k)
c y-boundary conditions for x > 0.0
c no CP because no concentration gradient exists
do 275 i = 2,ir
co(i,0,k) = co(i,2,k)
co(i,jr+1,k) = co(i,jr-1,k)
275 continue
245 continue
write(2,140)n,realtime,(co(i,jr,1),i=1,ir,100),
&((co(i,jr,k),i=101,ir,100),k=2,kr)
Qptot = 0.0
do 280 k = 1,kr
280 Qptot = Qptot+(2.0*ArP)*vw0*22.825E06
write(3,150)n,realtime,Qptot,concentrate
endif
c section-wise declarations, initial and boundary conditions end.
c *****
c section I boundary values at new time level
1000 vw1 = Ap*P0
c non-dimensionalize vw1
vninit(1) = vw1*LP/(uinit(1)*H)
unavg(1,1) = 1.0
do 290 j = 1,jr
un(1,j,1) = unavg(1,1)*0.095*(9.7*log(9.7-8.7*y(j,1))
&+8.7*y(j,1)-8.7)
vn(1,j,1) = vninit(1)*y(j,1)*(3.0-y(j,1)**2)/2.0
c concent represents concentrate concentration
c adjust concentration due to recycle mixing
cn(1,j,1) = (1.0+R*concent)/(1+R)

```



```

290 continue
c y - boundary conditions at x = 0.0
cn(1,0,1) = cn(1,2,1)
cn(1,jr+1,1) = cn(1,jr-1,1)+2.0*dely*vn(1,jr,1)*cn(1,jr,1)
&*Rej/Df(1)
go to 1200
c *****
c zero feed concentration at new time level; only to be used in
c the event of pure water flushing.
1100 vw1 = Ap*P0
c scale vw1
vninit(1) = vw1*LP/(uinit(1)*H)
unavg(1,1) = 1.0
do 295 j = 1,jr
un(1,j,1) = unavg(1,1)*0.095*(9.7*log(9.7-8.7*y(j,1))
&+8.7*y(j,1)-8.7)
vn(1,j,1) = vninit(1)*y(j,1)*(3.0-y(j,1)**2)/2.0
cn(1,j,1) = R*concent/(1+R)
295 continue
c y-boundary conditions at x = 0.0
cn(1,0,1) = cn(1,2,1)
cn(1,jr+1,1) = cn(1,jr-1,1)
c *****
c main body of the program follows for section I
1200 do 300 i = 2,ir
c guess a value for vn(i,jr)
vn(i,jr,1) = vo(i,jr,1)
unavg(i,1) = unavg(i-1,1)-delx*0.5*(vn(i,jr,1)+vn(i-1,jr,1))
do 310 j = 1,jr
310 un(i,j,1) = unavg(i,1)*0.095*(9.7*log(9.7-8.7*y(j,1))
&+8.7*y(j,1)-8.7)
do 320 j = 1,jr
320 vn(i,j,1) = vn(i,jr,1)*y(j,1)*(3.-y(j,1)**2)/2.0
c calculate a,b,c and d arrays
do 330 j = 1,jr
uavg(j,1) = 0.25*(un(i,j,1)+un(i-1,j,1)+uo(i,j,1)+uo(i-1,j,1))
vavg(j,1) = 0.25*(vo(i,j,1)+vo(i-1,j,1)+vn(i,j,1)+vn(i-1,j,1))
330 continue
do 340 j = 1,jr
a(j) = -(vavg(j,1)/(8*dely)+Df(1)/(4*dely**2))
b(j) = 1./(2.0*delt(1))+uavg(j,1)/(2*delx)+Df(1)/(2*dely**2)
c(j) = vavg(j,1)/(8*dely)-Df(1)/(4*dely**2)
d1(j) = (vavg(j,1)/(8.0*dely)+Df(1)/(4.0*dely**2))*cn(i-1,j-1,1)

```

```

&-(1./(2.*delt(1))-uavg(j,1)/(2.0*delx)+Df(1)/(2.0*dely**2))*
&cn(i-1,j,1)
&+(-vavg(j,1)/(8.0*dely)+Df(1)/(4.0*dely**2))*cn(i-1,j+1,1)
d2(j) = (vavg(j,1)/(8.0*dely)+Df(1)/(4.0*dely**2))*co(i,j-1,1)+
&(1.0/(2.0*delt(1))-uavg(j,1)/(2.0*delx)-Df(1)/(2.0*dely**2))*
&co(i,j,1)
&+(-vavg(j,1)/(8.0*dely)+Df(1)/(4.0*dely**2))*co(i,j+1,1)
d3(j) = (vavg(j,1)/(8.0*dely)+Df(1)/(4.0*dely**2))*co(i-1,j-1,1)
&+(1./(2.*delt(1))+uavg(j,1)/(2.0*delx)-Df(1)/(2.0*dely**2))*
&co(i-1,j,1)
&+(-vavg(j,1)/(8.0*dely)+Df(1)/(4.0*dely**2))*co(i-1,j+1,1)
d(j) = d1(j)+d2(j)+d3(j)
340 continue
c adjust terms for boundary conditions for section I
c(1) = c(1) + a(1)
a(jr) = a(jr) + c(jr)
b(jr) = b(jr) + c(jr)*2.0*dely*vn(i,jr,1)*Rej/Df(1)
99 format(i8,7(f10.4,2x))
c start the thomas algorithm
call thomas(sol,jr,j,a,b,c,d)
do 350 j = 1,jr
350 cn(i,j,1) = sol(j)
c calculate and compare velocity at y = 1.0
pi(i,1) = Kosm*cn(i,jr,1)*cinit
vn(i,jr,1) = Ap*(P(i,1)-pi(i,1))*LP/(uinit(1)*H)
do 360 j = 1,jr-1
360 vn(i,j,1) = vn(i,jr,1)*y(j,1)*(3.-y(j,1)**2)/2.
cn(i,0,1) = cn(i,2,1)
cn(i,jr+1,1) = cn(i,jr-1,1) + 2.0*dely*vn(i,jr,1)*cn(i,jr,1)
&*Rej/Df(1)
300 continue
c calculations on concentration end for section I
c flow calculations on section I
sum(1) = 0.0
do 370 i = 1,ir
370 sum(1) = sum(1) + vn(i,jr,1)
sum(1) = sum(1)/ir
Qp(1) = (2.0*ArP)*sum(1)*uinit(1)*H*22.825E06/LP
if(kr.eq.1) then
c calculate concentrate concentration
sumcon = 0.0
do 375 j = 1,jr
375 sumcon = sumcon + cn(ir,j,1)*un(ir,j,1)

```

```

    concent = sumcon/jr
  endif
c   flow calculations on section I end.
c   *****
c   start calculations for successive sections if they are present
  if(kr.gt.1) then
c   start section loop
  do 400 k = 2,kr
c   boundary conditions at new time level
c   cross flow velocity values
c   dimensionalize cross flow velocity at exit of previous section
  unavg(ir,k-1) = unavg(ir,k-1)*uinit(k-1)
c   equate values from previous section to new section
  unavg(1,k) = unavg(ir,k-1)
c   scale velocity at exit of previous section
  unavg(ir,k-1) = unavg(ir,k-1)/uinit(k-1)
c   scale velocity for the present section
  unavg(1,k) = unavg(1,k)/uinit(k)
  do 410 j = 1,jr
410  un(1,j,k) = unavg(1,k)*0.095*(9.7*log(9.7-8.7*y(j,k))
    &+8.7*y(j,k)-8.7)
c   repeat calculations for transverse velocity in identical steps
  vn(ir,jr,k-1) = vn(ir,jr,k-1)*uinit(k-1)*H/LP
  vn(1,jr,k) = vn(ir,jr,k-1)
  vn(1,jr,k) = vn(1,jr,k)*LP/(uinit(k)*H)
  vn(ir,jr,k-1) = vn(ir,jr,k-1)*LP/(uinit(k-1)*H)
  do 420 j = 1,jr
420  vn(1,j,k) = vn(1,jr,k)*y(j,k)*(3.0-y(j,k)**2)/2.0
c   repeat calculations for concentration
c   note that cinit is constant
  do 430 j = 1,jr
430  cn(1,j,k) = cn(ir,j,k-1)
c   y-boundary conditions at x = 0
  cn(1,0,k) = cn(1,2,k)
  cn(1,jr+1,k) = cn(1,jr-1,k)+2.0*dely*vn(1,jr,k)*cn(1,jr,k)
    &*Rej/Df(k)
c   *****
c   main body of the program for section k follows
  do 440 i = 2,ir
c   guess a value for vn(i,jr)
  vn(i,jr,k) = vo(i,jr,k)
  unavg(i,k) = unavg(i-1,k)-(vn(i,jr,k)+vn(i-1,jr,k))*delx*0.5
  do 450 j = 1,jr

```

```

450 un(i,j,k) = unavg(i,k)*0.095*(9.7*log(9.7-8.7*y(j,k))
    &+8.7*y(j,k)-8.7)
    do 460 j = 1,jr
460 vn(i,j,k) = vn(i,jr,k)*y(j,k)*(3.0-y(j,k)**2)/2.0
c   calculate a, b, c and d arrays
    do 470 j = 1,jr
        uavg(j,k) = 0.25*(un(i,j,k)+un(i-1,j,k)+uo(i,j,k)+uo(i-1,j,k))
        vavg(j,k) = 0.25*(vn(i,j,k)+vn(i-1,j,k)+vo(i,j,k)+vo(i-1,j,k))
470 continue
    do 480 j = 1,jr
c   calculate lhs arrays
        a(j) = -(vavg(j,k)/(8.*dely)+Df(k)/(4.*dely**2))
        b(j) = 1./(2.*delt(k))+uavg(j,k)/(2.*delx)+Df(k)/(2.*dely**2)
        c(j) = vavg(j,k)/(8.*dely)-Df(k)/(4.*dely**2)
c   calculate rhs arrays
        d1(j) = (vavg(j,k)/(8.*dely)+Df(k)/(4.*dely**2))*cn(i-1,j-1,k)
        &-(1./(2.*delt(k))-uavg(j,k)/(2.*delx)+Df(k)/(2.*dely**2))*
        &cn(i-1,j,k)
        &+(-vavg(j,k)/(8.*dely)+Df(k)/(4.*dely**2))*cn(i-1,j+1,k)
        d2(j) = (vavg(j,k)/(8.*dely)+Df(k)/(4.*dely**2))*co(i,j-1,k)+
        &(1./(2.*delt(k))-uavg(j,k)/(2.*delx)-Df(k)/(2.*dely**2))*
        &co(i,j,k)+
        &(-vavg(j,k)/(8.*dely)+Df(k)/(4.*dely**2))*co(i,j+1,k)
        d3(j) = (vavg(j,k)/(8.*dely)+Df(k)/(4.0*dely**2))*
        &co(i-1,j-1,k)+
        &(1./(2.*delt(k))+uavg(j,k)/(2.0*delx)-Df(k)/(2.*dely**2))*
        &co(i-1,j,k)+
        &(-vavg(j,k)/(8.*dely)+Df(k)/(4.*dely**2))*co(i-1,j+1,k)
        d(j) = d1(j)+d2(j)+d3(j)
480 continue
c   adjust terms for boundary conditions
        c(1) = c(1) + a(1)
        a(jr) = a(jr) + c(jr)
        b(jr) = b(jr) + c(jr)*dely*vn(i,jr,k)*Rej/Df(k)
c   start the thomas algorithm
        call thomas(sol,jr,j,a,b,c,d)
        do 490 j = 1,jr
490 cn(i,j,k) = sol(j)
c   calculate and compare velocity at y = 1.0
        pi(i,k) = Kosm*cn(i,jr,k)*cinit
        vn(i,jr,k) = Ap*(P(i,k)-pi(i,k))*LP/(uinit(k)*H)
        do 500 j = 1,jr-1
500 vn(i,j,k) = vn(i,jr,k)*y(j,k)*(3.-y(j,k)**2)/2.

```

```

c   incorporate boundary conditions at y = 0.0 and y = 1.0
    cn(i,0,k) = cn(i,2,k)
    cn(i,jr+1,k) = cn(i,jr-1,k) + 2.0*dely*vn(i,jr,k)*cn(i,jr,k)
    &*Rej/Df(k)
440  continue
101  format(11(f8.6,1x))
c   calculations on concentration end for section K
c   flow calculations on section K
    sum(k) = 0.0
    do 510 i = 1,ir
510  sum(k) = sum(k) + vn(i,jr,k)
    sum(k) = sum(k)/ir
    Qp(k) = (2.0*ArP)*sum(k)*uinit(k)*H*22.825E06/LP
c   flow calculations end for section K
c   calculations continue for all sections
400  continue
    endif
c   calculations end
    n = n+1
    realtime = realtime +realdt
c   *****
c   calculate total flow
    if(kr.eq.1) then
    Qptot = Qp(1)
c   print concentrations and flows
    n1 = mod(n,100)
    if(n1.eq.1) then
    write(2,140)n,realtime,(cn(i,jr,1),i=1,ir,20)
140  format(i8,',',f10.4,',',11(f8.5,','))
    concentrate = concent*cinit*1000.
    write(3,150)n,realtime,Qptot,concentrate
    endif
    elseif(kr.gt.1) then
    Qptot = 0.0
    do 520 k = 1,kr
520  Qptot = Qptot + Qp(k)
c   calculate concentrate concentration
    if(kr.gt.1) then
    sumcon = 0.0
    do 525 j = 1,jr
525  sumcon = sumcon + cn(ir,j,kr)*un(ir,j,kr)
    sumcon = sumcon/unavg(ir,kr)
    concent = sumcon/jr

```

```

endif
c *****
c print concentrations and flows
  if(n.le.1001) then
    n1 = mod(n,100)
  else
    n1 = mod(n,1000)
  endif
  if(n1.eq.1) then
    write(2,145)n,realtime,(cn(i,jr,1),i=1,ir,100)
    &,,(cn(i,jr,k),i=101,ir,100),k=2,kr)
145 format(i8,',',f10.4,',',11(f8.5,','))
    concentrate = concent*cinit*1000.
    write(3,150)n,realtime,Qptot,concentrate
  endif
150 format(i8,',',f10.4,',',f10.4,',',f10.4)
  endif
c *****
c exchange all values
  if(n.le.nmax) then
c exchange values for section I
    do 530 i = 1,ir
      uoavg(i,1) = unavg(i,1)
      do 540 j = 1,jr
540 uo(i,j,1) = un(i,j,1)
          do 550 j = 0,jr+1
550 co(i,j,1) = cn(i,j,1)
              do 560 j = 1,jr
560 vo(i,j,1) = vn(i,j,1)
530 continue
          if(kr.eq.1) then
            if(counter.ge.1) then
              go to 1000
            else
              go to 1100
            endif
          endif
c exchange if other sections are present
          if(kr.gt.1) then
            do 600 k = 2,kr
              do 610 i = 1,ir
                uoavg(i,k) = unavg(i,k)
              do 620 j = 1,jr

```

```

620 uo(i,j,k) = un(i,j,k)
    do 630 j = 0,jr+1
630 co(i,j,k) = cn(i,j,k)
    do 640 j = 1,jr
640 vo(i,j,k) = vn(i,j,k)
610 continue
600 continue
    if(counter.ge.1) then
        go to 1000
    else
        go to 1100
    endif
endif
endif
endif
c  start another run
write(6,*)'Do you want pure solvent flush ?'
write(6,*)'Enter 1 for yes, 0 to no'
read(4,*)int
if(int.eq.1) then
c  this is for pure water flush
counter = 0
n = 1
realtime = 0.0
write(2,*)' '
write(3,*)' '
go to 1100
endif
c  start run at a new inlet pressure
P0 = P0/6.8947
P0 = P0+20.
n = 1
realtime = 0.0
write(2,*)' '
write(3,*)' '
if(P0.le.180) then
go to 999
else
stop
endif
end

```

```

subroutine inputpr3(Q0,Ar,Ap,Diff,Kosm,L,H,cinit,uin)
c  this program will accept all the required input
c  parameters for developing a predictive model for
c  spiral wound membranes
double precision cinit,uin,H,Ar,L,Diff,Kosm
double precision Q0,Ap
integer num
open(1,file='inpr')
c  C0 is the feed solute concentration (mg/L)
c  H is the feed spacer thickness (m)
c  Ar is the membrane area (sq.m)
c  L is the length of the membrane (m)
c  R is the rejection,delP is the initial
c  applied pressure
c  Q0 is the feed flow (m3/s)
c  vw0 is the initial permeation
c  velocity (m/s), Ap is the water permeability
c  input parameters
c  read spacer thickness in mils
read(1,5)H
5  format(f5.2)
c  convert mils to meters
H = H*0.3048*0.001/12.0
c  read element length in inches
read(1,10)L
10 format(f8.2)
c  read number of elements
read(1,*)num
c  calculate total membrane length
L = L*num
c  convert inches into meters
L = L*0.3048/12.0
c  read element area in sq. ft
read(1,15)Ar
c  calculate total membrane area and convert to sq. m
Ar = Ar*(0.3048*0.3048)*num
15 format(f8.3)
c  read permeability in GFD/PSI
read(1,20)Ap
20 format(f12.10)
c  convert GFD/PSI into m3/m2.sec.KPa
Ap = Ap*6.839E-08
c  convert PSI into KPa

```



```

c  read feed flow in gpm
  read(1,35)Q0
35  format(f10.2)
c  convert GPD into m3/sec
   Q0 = Q0/22.825E06
c  read feed concentration in mg/L
  read(1,40)cinit
40  format(f10.4)
c  convert mg/L into kg/m3
   cinit = cinit*0.001
c  read diffusivity in m2/s
  read(1,45)Diff
45  format(e10.4)
c  read osmotic pressure constant in psi.L/mg
  read(1,50)Kosm
50  format(f5.4)
c  convert psi.L/mg into KPa.m3/kg
   Kosm = Kosm*6.8947*1000.0
c  calculate initial cross flow velocity in m/sec
   uin = (2.0*Q0*L)/(H*Ar)
c  Normalize H and Ar for one half of the membrane
   H = H/2.0
   Ar = Ar/2.0
  return
end

```

```

subroutine thomas(sol,jr,j,a,b,c,d)
double precision a(51),b(51),c(51),d(51)
double precision beta(51),gamma(51),sol(51)
integer i,j,k,jr,jr1
beta(1) = b(1)
gamma(1) = d(1)/b(1)
do 1000 j = 2,jr
beta(j) = b(j)-a(j)*c(j-1)/beta(j-1)
gamma(j) = (d(j)-a(j)*gamma(j-1))/beta(j)
1000 continue
c    back calculation
sol(jr) = gamma(jr)
jr1 = jr-1
do 1010 j = 1,jr1
k = jr-j
sol(k) = gamma(k)-c(k)*sol(k+1)/beta(k)
1010 continue
return
end

```

Input file: inpr
30.
40.
3
90.
0.078
4320.0
1000.0
1.61E-09
0.01

Input file: inputdatrpr

0.0

3

10001

6

201

0.005

0

0

0

0

0

0

0

0

0

1

0

0

1

0

0